ISSN 2074-272X

науково-практичний
журнал 2020/3

Електротехніка і Електромеханіка

Electrical Engineering & Electromechanics

Електричні машини та апарати
Електротехнічні комплекси та системи
Силова електроніка
Електроізоляційна та кабельна техніка
Електричні станції, мережі і системи
Ювілеї

З 2015 р. журнал індексується у міжнародній наукометричній базі Web of Science Core Collection: Emerging Sources Citation Index

«ELECTRICAL ENGINEERING & ELECTROMECHANICS»
SCIENTIFIC & PRACTICAL JOURNAL
Journal was founded in 2002
Founders:
National Technical University «Kharkiv Polytechnic Institute» (Kharkiv, Ukraine)
State Institution «Institute of Technical Problems of Magnetism of the NAS of Ukraine» (Kharkiv, Ukraine)

INTERNATIONAL EDITORIAL BOARD

Sokol Ye.I.	**Editor-in-Chief**, Professor, Corresponding member of NAS of Ukraine, Rector of NTU "KhPI", Ukraine
Korytchenko K.V.	**Deputy Editor,** Professor, National Technical University "Kharkiv Polytechnic Institute" (NTU "KhPI"), Ukraine
Rozov V.Yu.	**Deputy Editor,** Professor, Corresponding member of NAS of Ukraine, Director of State Institution "Institute of Technical Problems of Magnetism of the NAS of Ukraine"(SI "ITPM NASU"), Kharkiv, Ukraine
Batygin Yu.V.	Professor, Kharkiv National Automobile and Highway University, Ukraine
Bíró O.	Professor, Institute for Fundamentals and Theory in Electrical Engineering, Graz, Austria
Bolyukh V.F.	Professor, NTU "KhPI", Ukraine
Colak I.	Professor, Nisantasi University, Istanbul, Turkey
Doležel I.	Professor, University of West Bohemia, Pilsen, Czech Republic
Féliachi M.	Professor, Technological Institute of Saint-Nazaire, University of Nantes, France
Gurevich V.I.	Ph.D., Honorable Professor, Central Electrical Laboratory of Israel Electric Corporation, Haifa, Israel
Ida N.	Professor, The University of Akron, Ohio, USA
Kildishev A.V.	Associate Research Professor, Purdue University, USA
Kuznetsov B.I.	Professor, SI "ITPM NASU", Ukraine
Kyrylenko O.V.	Professor, Member of NAS of Ukraine, Institute of Electrodynamics of NAS of Ukraine (IED of NASU), Kyiv, Ukraine
Nacke B.	Professor, Gottfried Wilhelm Leibniz Universitat, Institute of Electrotechnology, Hannover, Germany
Podoltsev A.D.	Professor, IED of NASU, Kyiv, Ukraine
Rainin V.E.	Professor, Moscow Power Engineering Institute, Russia
Rezynkina M.M.	Professor, NTU "KhPI", Ukraine
Shkolnik A.A.	Ph.D., Central Electrical Laboratory of Israel Electric Corporation, member of CIGRE (SC A2 - Transformers), Haifa, Israel
Trichet D.	Professor, Institut de Recherche en Energie Electrique de Nantes Atlantique, Nantes, France
Yatchev I.	Professor, Technical University of Sofia, Sofia, Bulgaria
Yuferov V.B.	Professor, National Science Center "Kharkiv Institute of Physics and Technology", Ukraine
Zagirnyak M.V.	Professor, Member of NAES of Ukraine, rector of Kremenchuk M.Ostrohradskyi National University, Ukraine
Zgraja J.	Professor, Institute of Applied Computer Science, Lodz University of Technology, Poland

ISSUE 3 / 2020

TABLE OF CONTENTS

Electrical Machines and Apparatus

Electrotechnical Complexes and Systems

Power Electronics

Electrical Insulation and Cable Engineering

Power Stations, Grids and Systems

Editorial office address: Dept. of Electrical Apparatus, NTU «KhPI», Kyrpychova Str., 2, Kharkiv, 61002, Ukraine
phones: +380 57 7076281, +380 67 3594696, **e-mail:** a.m.grechko@gmail.com (**Grechko O.M.)**

ISSN (print) 2074-272X
ISSN (online) 2309-3404

© National Technical University «Kharkiv Polytechnic Institute», 2020
© State Institution «Institute of Technical Problems of Magnetism of the NAS of Ukraine», 2020

Printed 23 June 2020. Format 60 x 90 ⅛. Paper – offset. Laser printing. Edition 200 copies.
Printed by Printing house «Madrid Ltd» (18, Gudanova Str., Kharkiv, 61024, Ukraine)

UDC 621.3.04: 621.316 **doi: 10.20998/2074-272X.2020.3.01**

E.I. Baida, B.V. Klymenko, S.V. Vyrovets, M.G. Pantelyat, M. Clemens

INVESTIGATIONS OF THE DYNAMICS OF A BISTABLE ELECTROMAGNET WITH IMPROVED CHARACTERISTICS FOR MEDIUM VOLTAGE VACUUM CIRCUIT BREAKERS

Introduction. Currently, for switching medium voltage circuits, vacuum circuit breakers are widely used, which have good arcing properties and high breaking capacity. One of the problems of creating the drive mechanism of such apparatus is the need to ensure the absence of contact welding when a through current of a short circuit of a given duration flows through them, which is achieved due to a certain amount of contact pressure. One of the problems arising in the design of circuit breakers is the need to fix the mechanism with a mechanical lock, which should hold the mechanism securely. This leads to significant specific mechanical loads, which in turn reduces the reliability of the circuit breaker. One way to solve these problems is to create a drive based on monostable or bistable electromagnetic actuators with highly coercive permanent magnets, which provide reliable fixation of the position of the contacts. Purpose. Investigation of the improved design of a bistable electromagnetic actuator based on permanent magnets of a medium voltage vacuum circuit breaker. Methods. Theoretical and experimental research and comparative analysis of existing and developed electromagnetic actuators. Conclusions. A new design of an electromagnetic bistable actuator with reduced overall dimensions is developed and tested. The electromechanical characteristics of the actuator correspond to the technical specifications, which is confirmed by both theoretical and experimental studies. The proposed actuator can be used as a drive mechanism for medium voltage vacuum circuit breakers. References 10, figures 17, tables 3.

Key words: **bistable electromagnet, actuator, vacuum circuit breaker, multiphysics model.**

В статье исследован новый бистабильный электромагнит с высококоэрцитивными постоянными магнитами, который предполагается использовать в качестве актуатора вакуумных выключателей средних напряжений. Приводится теоретическое и экспериментальное исследование усовершенствованной конструкции электромагнита с целью сравнительного анализа его параметров с параметрами имеющейся конструкции. Теоретическое исследование базируется на мультифизической модели, которая включает расчет статического и динамического электромагнитных полей в нелинейной проводящей неоднородной среде с учетом постоянных магнитов, нелинейных уравнений разрядной цепи накопительного конденсатора, нелинейных уравнений движения. Экспериментальные исследования, которые проводились на реальном вакуумном выключателе, показали соответствие параметров нового бистабильного электромагнита расчетным показателям. Направление дальнейших исследований представляются в виде оптимизации геометрии электромагнита и схемы управления. Библ. 10, рис. 17, табл. 3.

Ключевые слова: **бистабильный электромагнит, актуатор, вакуумный выключатель, мультифизическая модель.**

Introduction. In recent years, vacuum switching devices having unique arcing properties and high breaking capacity [1] are widely used in medium voltage circuits. One of the most important characteristics of such apparatus is the rated short-time withstand current – the current that the circuit breaker must withstand for given time in accordance with the test conditions [2] defined by the standard, which is achieved due to a certain value of contact pressure. Under the electromagnetic actuator we understand the device that creates the movement of contacts when excited by an electric signal of an electromagnetic field in an electromagnet. Here, the movement of the contacts in one direction is provided by the traction force of the electromagnet, and in the other one by contact and disconnecting springs. Thus, the electromagnet together with the contact springs forms an electromagnetic actuator. From experimental data it is known [1, 3] that to ensure the breaking capacity of the circuit breaker of 20 kA, contact pressure should be of the order 2 kN per pole or about 6 kN per three poles, respectively. Such contact pressures are provided by Belleville springs, therefore, the mechanical opposing characteristic has its own peculiarity (Fig. 1), which consists in a jump in the opposing force at the moment of contact touch. This leads to a slowdown in the velocity of movement of the armature of the electromagnet and a possible «freezing» of the drive mechanism [4] (if the kinetic energy of the moving parts is not enough to overcome the area where the electromagnetic force is less than the opposing one).

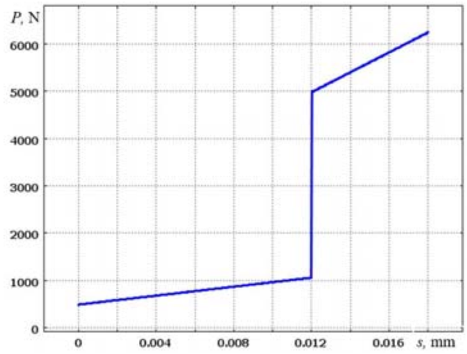

Fig. 1. The dependence of the opposing force (P) as a function of the stroke (s) of the armature

There are publications on the design and calculation of electromagnetic actuators [4-6]. One of the problems arising in the design of circuit breakers is the need to fix the mechanism of the circuit breaker in extreme positions. Actuators of vacuum circuit breakers, as a rule, use neutral electromagnets or electric motors, the main disadvantage of which is the presence of mechanical locks – mechanical latches that securely hold the mechanism in the on position. The main requirement for mechanical latches is the small force required to release the free trip mechanism when the circuit breaker is switched off, which is associated with its velocity. This leads to significant specific mechanical loads on the mechanical element, which in turn reduces the reliability of the circuit breaker. In addition, electromagnetic and spring-motor actuators are complex and require qualified service.

One way to solve these problems is to create an actuator based on monostable (Fig. 2,*a*) or bistable (Fig. 2,*b*) polarized electromagnets with highly coercive permanent magnets, which provide reliable fixation of contacts in extreme positions, consuming energy only in transient modes. The advantage of such electromagnets is the simplicity of design and reliability.

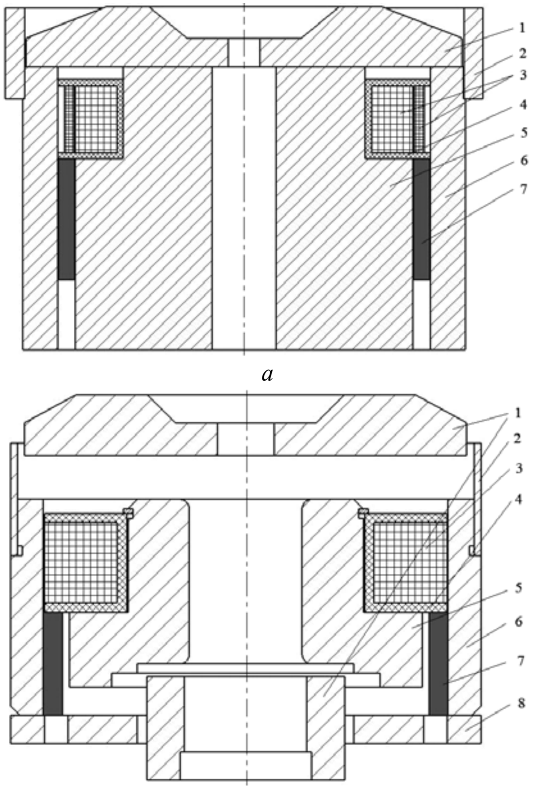

a

b

Fig. 2. Sketches of monostable (*a*) and bistable (*b*) electromagnets

The designs of shown in Fig. 2 electromagnets are similar. Each includes a movable armature (1), a ferromagnetic shunt (2), a winding (3), a winding frame (4), a core (5), a housing (6), permanent magnets (7) located along the inner perimeter of the housing, and a base (8). In the design of a bistable electromagnet, a non-magnetic rod, which is connected to the movable contacts through the shaft levers, also connects the upper and lower armatures, which ensures synchronization of the movement of the armatures when the electromagnet is triggered (not shown in Fig. 2). The main differences of these electromagnets are as follows:

- in a bistable electromagnet, armature fixation in two extreme positions is provided by permanent magnets, and in a monostable one – by permanent magnets (on) and a spring (off);
- a change in the position of the armature in a bistable electromagnet occurs due to a change in the direction of the current in the winding (polarized electromagnet), in a monostable one – by applying voltage to the additional winding.

The design and operation principle of a monostable electromagnet (Fig. 2,*a*) are considered in [6, 7]. The disadvantages of its design include:

- the charge voltage of the capacitor of the control winding circuit of a monostable electromagnet is 380-400 V, which is unsafe for maintenance personnel;
- significant (in relation to the dimensions of the circuit breaker) dimensions;
- the presence of two windings (on and off);
- a significant amount of permanent magnets, which increases the cost of the electromagnet.

These shortcomings are the reason for the development of a new design of a bistable polarized electromagnet (Fig. 2,*b*) [8].

Thus, **the goal of the paper** is to create a mathematical multiphysics model for calculating the dynamic parameters of a bistable electromagnet based on highly coercive permanent magnets with improved characteristics for medium voltage vacuum circuit breakers. In addition, in the course of experimental studies, it is necessary to verify the adequacy of the created model.

Problem definition. As mentioned above, a monostable electromagnet has several disadvantages. Therefore, when designing and studying a bistable polarized electromagnet, the following tasks are formulated:

- to reduce the size and mass of the magnetic system;
- to reduce the mass of highly coercive permanent magnets used, which will reduce the cost of the electromagnet;
- to reduce the charge voltage of the capacitor to a practically safe value of 100-110 V, while ensuring reliable operation of the circuit breaker (when the touch voltage decreases from 400 V to 100 V, the total resistance of the human body along the path «arm–arm» increases by about 2.7 times – from about 1300 Ω to about 3500 Ω, and the direct current through the human body decreases by about 11 times – from about 310 mA to about 28 mA (see Fig. 2.2 on p. 102 in [1]), which makes a contact scenario almost safe);
- to ensure high thermal stability of the circuit breaker due to the holding force of the bistable electromagnet armature with permanent magnets of at least 6.5 kN.

The design shown in Fig. 2,*b* [8] is obtained on the basis of numerous preliminary calculations and studies. For the final decision on the parameters of the prototype, comparative calculations of the dynamic characteristics of a bistable polarized electromagnet with a monostable one have been carried out. Also, experimental studies of the new actuator have been carried out when it was installed in a vacuum circuit breaker. All calculations are carried out with the same parameters of the opposing force, the mass of contacts, levers and traction insulators, the mechanical work of the forces opposing the movement (the same armature stroke and contact failure) and the specific characteristics of permanent magnets (coercive force and residual magnetic flux density).

The multiphysics model of the actuator given in [6, 9] is based on the Maxwell equations and written in terms of the magnetic vector potential for a nonlinear conducting moving medium taking into account the field of permanent highly coercive magnets with boundary conditions – the zero value of the magnetic vector potential at the remote boundary and the axial component of the field on the axis of symmetry. The problem is solved by the Finite Element Method in axisymmetrical formulation, and for discretization in time domain the implicit multistep Adams-Moulton method of the 4th order with adaptive selection of time step values is used. The PDE system solved to obtain electromagnetic field distribution is supplemented by a separate system of nonlinear equations of the discharge circuit of the storage capacitor and a system of nonlinear equations of motion [6, 9], the form of which is determined by the electrical circuit for connecting the winding to the energy source and the kinematics of the mechanical system under consideration. In the calculations, all moving masses and the opposing force are reduced to the armature of the electromagnet. Since the calculation is carried out in the COMSOL Multiphysics code, the assumptions made during the calculation are minimal: the frictional forces in the bearings (axes) and the change in the resistance of the winding as a result of heating due to their smallness are not taken into account. The calculation consists of two stages: static calculation and dynamic one. To calculate the dynamics, the initial data are the results of a static calculation.

The nature of the movement is significantly affected by a change in the reduced mass of the armature (Fig. 3), which is associated with the closure of contacts at the moment of impact. Assuming that the impact is inelastic and «stretched» it in time by 0.4 ms, we can write:

$$\frac{d(m\cdot v)}{dt}\cdot\vec{1}_s=\left(\frac{dm}{dt}\cdot v+m\cdot\frac{dv}{dt}\right)\cdot\vec{1}_s=\left(\frac{dm}{ds}\cdot v^2+m\cdot\frac{dv}{dt}\right)\cdot\vec{1}_s, \quad (1)$$

where m is the mass reduced to armature; v is the velocity of movement; s is the armature displacement; $\vec{1}_s$ is the directional unit vector.

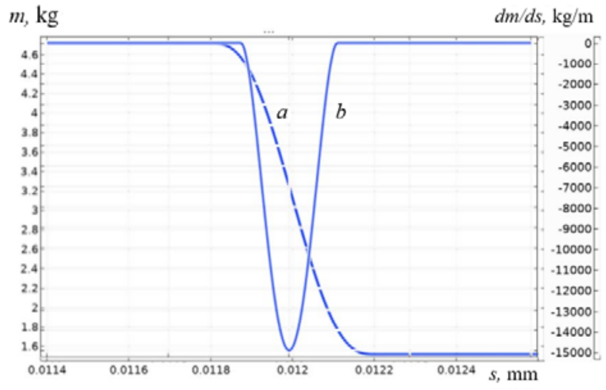

Fig. 3. Change in mass (a) and its derivative (b) as functions of the displacement at the moment of the contacts touch

Table 1 shows the parameters of the windings of the electromagnets and the supply circuit. The initial voltage at the capacitor U_{c0} is chosen as the minimum voltage for the operation of electromagnets.

Table 1

Parameters of electromagnet windings and supply circuit

Parameter	Monostable	Bistable
U_{c0}, V	400	105
number of turns w	700	270
R, Ω	19	1.53
C, μF	10000	60000

The results of a comparative calculation of the dynamic characteristics of actuators. The results of calculating the movement of the armature of the electromagnets as a function of time when switched on are shown in Fig. 4, and the results of calculating the driving force (it means the difference between the traction force developed by the electromagnets and the opposing force) as a function of time – in Fig. 5.

From the graphs it follows: the increase in the total force of a monostable electromagnet occurs more quickly, which, combined with a slightly lower mass of the armature and a smaller time constant determines its higher velocity. The graphs show a significant decrease in the driving force at the moment of the contacts touch.

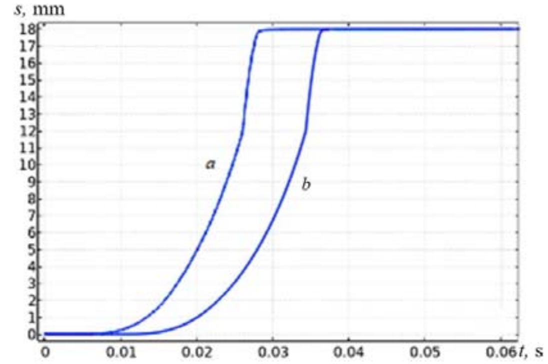

Fig. 4. Displacement of the armature of monostable (a) and bistable (b) electromagnets as a function of time

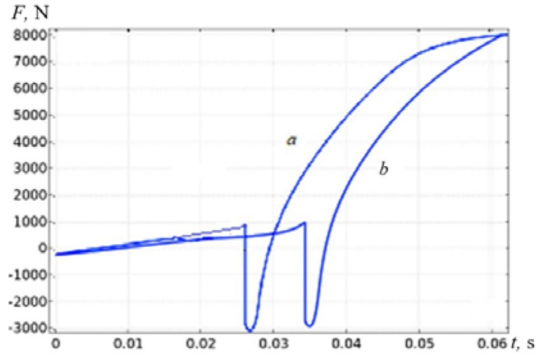

Fig. 5. Comparative characteristics of the driving force F created by monostable (a) and bistable (b) electromagnets

The influence of changes in the reduced mass during the movement of the system is illustrated by the velocity graphs (Fig. 6), which show its jump at the moment of contact closure. In this case, the kinetic energy of the remaining moving parts of the actuator (armature, levers, contact holder) increases which should be enough to overcome the area in which the driving force is negative. Otherwise, the system may «freeze».

It is advisable to carry out a further comparative analysis by the magnetizing force of the windings, which is shown in Fig. 7. The winding currents are presented in Fig. 8.

With almost the same magnetizing force of the windings (the opposing characteristic is the same), the currents of electromagnets vary significantly due to different winding data (windings sizes, wire diameter, number of turns, etc.).

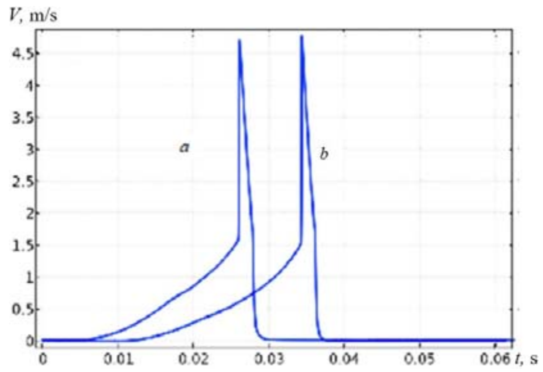

Fig. 6. Velocity of the armature movement of the monostable (a) and bistable (b) electromagnets

It should be noted that the graphs of currents allow to evaluate the actuator operating parameters [4].

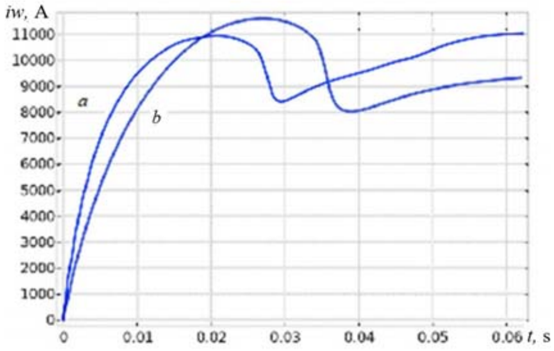

Fig. 7. Magnetizing force of the monostable (*a*) and bistable (*b*) electromagnets

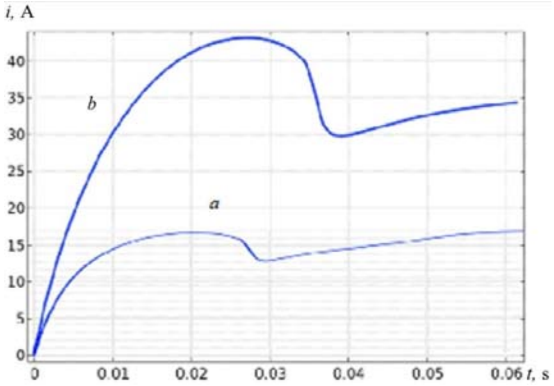

Fig. 8. Currents of windings of the monostable (*a*) and bistable (*b*) electromagnets

The minimum of the current curve approximately corresponds to the actuator operating time, and the current fluctuation in the winding circuit means a possible «freezing» of the drive mechanism, which is unacceptable, since it causes the circuit breaker contacts to not switch on completely, leading to an accident. Such a case is shown in Fig. 9 (solid line is the touch line of the contacts) when the capacitor charge voltage U_{c0} in calculation is insufficient for the actuator to operate.

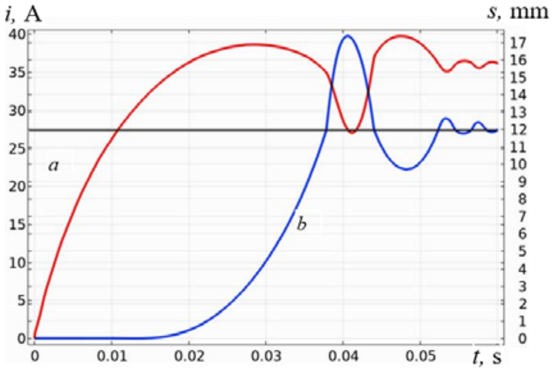

Fig. 9. Current and stroke of the armature during emergency switching on of the electromagnet:
a – winding current; *b* – electromagnet armature stroke

From Fig. 9 it follows that before reaching its final position, the electromagnet armature, levers, traction insulators and contacts started the reverse movement and passed the touch point of the contacts in the opposite direction. Then the contacts opened, the opposing force decreased (see Fig. 1), and the contacts again began to move in the direction of closure, «hanging» at the point of contact. This means that when short circuit current is switched on, the contacts and vacuum chambers can be damaged as a result of burning on the contacts of a powerful electric arc. Closing the contacts of the circuit breaker with small contact pressure is a serious accident, significantly reducing the thermal stability of the circuit breaker both during the flow of rated and emergency currents.

Since the function of switching an electric circuit by a circuit breaker assumes both connecting consumers to energy sources and disconnecting them from these sources, the next step is to study the process of disconnecting a load by a circuit breaker. Figure 10 shows the time dependence of the armature displacement of a new bistable electromagnet during switching off.

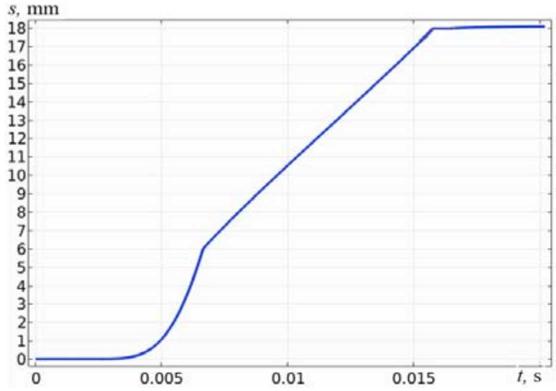

Fig. 10. Dependence of the displacement of the armature of the electromagnet during switching off

An analysis of this dependence shows that the breaker contacts open in about 7 ms, and the off process takes place within 16-17 ms which is approximately two times faster than switching on (Fig. 4,*b* and Fig. 10).

Of interest is also the form of the total force acting on the armature of the electromagnet which is shown in Fig. 11.

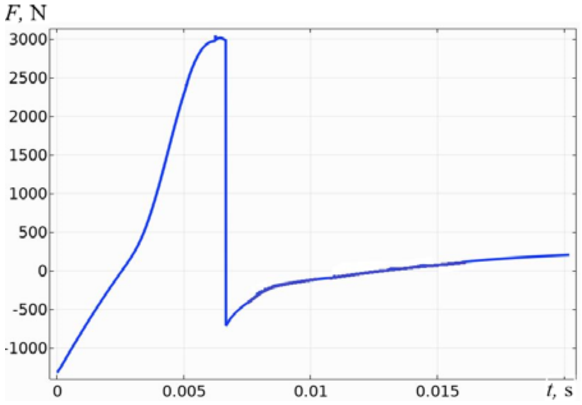

Fig. 11. The total force acting on the armature of an electromagnet when switched off as a function of time

The velocity graph is shown in Fig. 12. As follows from the graph, at the moment of opening the contacts, the velocity of the system decreases due to the attachment to the armature of the mass of contacts, levers and traction insulators.

Indicative is the graph of the current in the winding circuit, which, due to the counter-EMF of armature movement, takes negative values, i.e. recharges the capacitor (see Fig. 13).

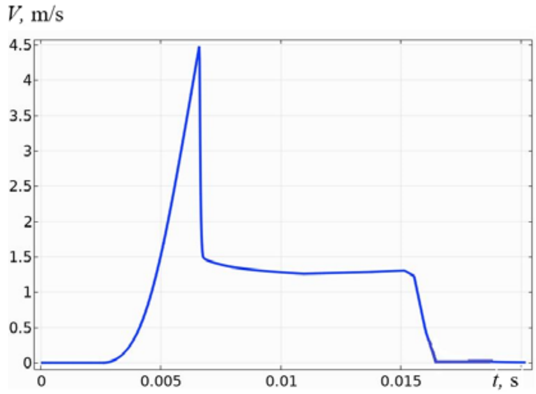

Fig. 12. The electromagnet armature velocity during switching off

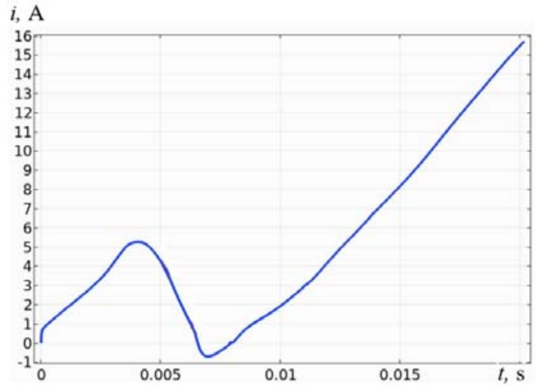

Fig. 13. Winding current change during switching off

This follows from the fact that, according to Ohm law

$$i = \frac{U_c + E}{r}, \tag{2}$$

where U_c is the voltage on the capacitor; E is the counter-EMF of movement; r is the resistance of the winding and connecting wires.

But at the same time

$$E = -w \cdot \frac{d\Phi}{dt} = -w \cdot \frac{d\Phi}{ds} \cdot v, \tag{3}$$

where w is the number of turns; Φ is the magnetic flux; s is the displacement of the armature; v is the velocity.

Therefore, if the velocity is high, then the counter-EMF can be larger in magnitude than the voltage on the capacitor. In this case, the current will be negative.

It should be noted that due to the opposing springs, the magnetizing force sufficient to switch off is approximately 1.5 kA, while to switch on is about 10 kA. Figure 14 shows the nature of the change in voltage on the capacitor during switching off.

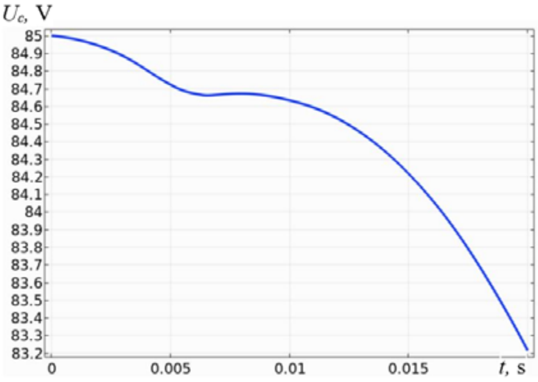

Fig. 14. Capacitor voltage change during switching off

As follows from Fig. 14, due to the large capacitance, the voltage during the switching off time of about16 ms varies slightly (by less than 1 V), and the decrease in voltage during the total switch on duration is about 20 V).

This gives grounds to assert that the standard operation OFF-ON-OFF will be successfully performed provided that the energy source (capacitor) is disconnected from the electromagnet winding in a timely manner using, for example, the position sensor when the circuit breaker changes its state.

An experimental study of the developed design of a bistable electromagnet. For experimental studies, a prototype bistable electromagnet has been manufactured, which is installed in the casing of a vacuum circuit breaker. A capacitor bank is used as the power source of the electromagnet, and the electric circuit is closed to the winding of the electromagnet and is not turned off until the capacitor bank is completely discharged.

Figure 15 shows the oscillogram of the switching on of the electromagnet at U_{c0} = 105 V.

Figure 16 shows the oscillogram of the switching off of the electromagnet at U_{c0} = 60 V.

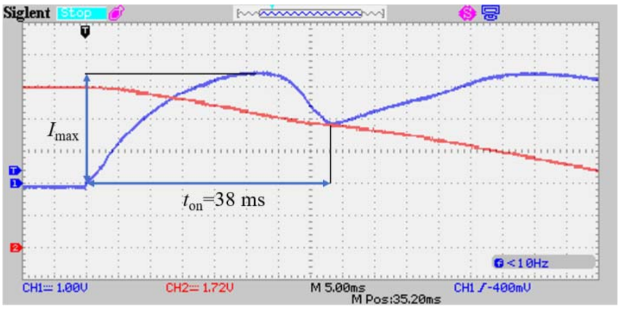

Fig. 15. The oscillogram of the switching on of a bistable actuator, where the horizontal time scale is 5 ms/div; the vertical current scale is 10 A/div

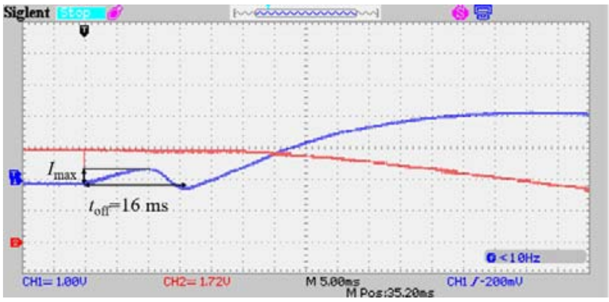

Fig. 16. The oscillogram of the switching off of a bistable actuator, where the horizontal time scale is 5 ms/div; the vertical current scale is 10 A/div

A comparative analysis of the calculated and experimental temporal characteristics of the bistable actuator is shown in Table 2, where I_{max} is the first maximum of the current of the electromagnet winding.

Table 2

Comparative analysis of calculated and experimental temporal characteristics of a bistable actuator

	Switching on		Switching off	
	Calculation	Experiment	Calculation	Experiment
I_{max}, A	39.0	43.0	3.6	4.0
t, ms	38.0	38.0	9.5	16.0

The discrepancy between the experimental and calculated data (especially in time during the switching off process) can be for various reasons, the most likely of which are the following:

- uncertainty of the electrical resistivity of the material of the magnetic circuit;
- parameters of permanent magnets;
- friction forces in hinges and bearings;
- change in contact failure due to repeated switching operations, etc.

The uncertainty of the electrical resistivity of the material of the magnetic circuit is the dominant factor, which is confirmed by the results of studies in [10].

During testing, with insufficient capacitor charge voltage, the electromagnet did not switch on completely, at which the armature became «stuck» at the value of the failure. The oscillogram of this process is shown in Fig. 17, which confirms the data obtained by calculation (see Fig. 9).

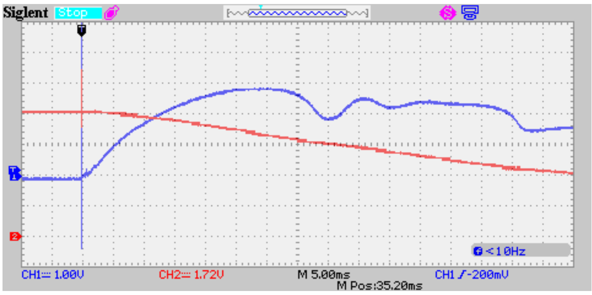

Fig. 17. The process of fuzzy switching on of an electromagnet

Comparative mass and dimensional characteristics of monostable and developed bistable electromagnets are presented in Table 3.

Table 3

Comparative mass and dimensional characteristics of electromagnets

	Monostable	Bistable
Diameter, mm	150	140
Height, mm	110	90
Electromagnet mass, kg	11.5	8.63
Copper mass, kg	0.44	0.73
Permanent magnets mass, kg	0.49	0.33

Conclusions.

1. The created mathematical multiphysics model allows to determine the basic dynamic parameters of a bistable electromagnet: switching on and switching off times, armature velocity, etc.

2. The developed design of a bistable electromagnet, compared with the known monostable design, has outer diameter smaller by 6.7 %, lower by 18.2 % height, which, in this case, is a decisive factor for a limited space inside the housing of the vacuum circuit breaker. The mass of the new electromagnet is also decreased by 25 %.

3. The analysis of static traction characteristics with de-energized windings in the drawn position of the armature gives the following values: the well-known monostable electromagnet – 8.5 kN; a new developed bistable electromagnet – 6.9 kN with the required 6.5 kN. The force of 8.5 kN is unreasonably high for this type of circuit breaker. Such a load requires strengthening of the circuit breaker housing, drive rods and shaft. From this point of view, the developed bistable electromagnet is more preferable.

4. The ratio of the holding force to the total mass of the electromagnet in the new design is 800 N/kg, while for a monostable electromagnet this indicator is 740 N/kg. At the same time, the mass of the permanent magnets decreased by 32.6 %.

5. Since the switching off time of the actuators is mainly determined by the force of the opposing springs, the difference in switching off time is insignificant. The switching off time is 16 ms, and the switching on time is 37 ms, which is comparable to the switching on time of the vacuum circuit breakers manufactured by ABB. Therefore, the result obtained for the developed bistable electromagnet is completely acceptable.

6. The results of investigations allow to talk about the prospects of using the developed design of the electromagnet as an actuator of medium voltage vacuum circuit breakers.

REFERENCES

1. Klymenko B.V. *Elektrychni aparaty. Zahalnyi kurs* [Electric apparatus. The general course]. Kharkiv, Tochka Publ., 2013. 400 p. (Ukr).

2. *VM1-T. Vacuum circuit-breaker.* Available at: https://library.e.abb.com/public/e9408d38c8324932ac60aa9e935e481a/MA_VM1-T(EN)-_1VCD601412%20-%20BA%20543-02.pdf (accessed 06 April 2019).

3. Klymenko B.V., Bugaychuk V.M., Grechko A.M. A pre-production model of two-position electromagnetic drive for an average-voltage vacuum switch. *Electrical engineering & electromechanics*, 2005, no. 2, pp. 23-27. (Rus).

4. Baida E.I. Fuzzy dynamic response of a bistable electromagnetic actuator based on high-coercitivity permanent magnets. *Electrical engineering & electromechanics*, 2012, no. 5, pp. 18-20. (Rus).

5. Ro J.-S., Hong S.-K., Jung H.-K. Characteristic analysis and design of a novel permanent magnetic actuator for a vacuum circuit breaker. *IET Electric Power Applications*, 2013, vol. 7, no. 2, pp. 87-96. **doi: 10.1049/iet-epa.2012.0176.**

6. Bayda Ye.I., Vyrovets S.V. Characteristic of monostable actuator starting. *Naukovyi Visnyk Natsionalnoho Hirnychoho Universytetu*, 2013, issue 6, pp. 72-77. (Rus).

7. Klymenko B.V., Vyrovets S.V., Forkun Ya.B. *Elektromagnitnyj pryvid* [Electromagnetic actuator]. Patent UA, no. 15210, 2006. (Ukr).

8. Bugaychuk V.M., Klymenko B.V., Varshamova I.S., Grechko O.M. *Elektromagnitnyj pryvid* [Electromagnetic actuator]. Patent UA, no. 130401, 2018. (Ukr).

9. Baida E.I. A mathematical model for calculating the dynamics of on-off electromagnetic actuators of medium voltage vacuum circuit breakers. *Journal of scientific publications of graduate students and doctoral students*, 2013, no. 1, pp. 136-141. (Rus).

10. Grechko A.M. Experimental research of eddy currents in the magnetic core on dynamic characteristics of the electromagnetic actuator, *Bulletin of NTU «KhPI». Series: Problems of Electrical Machines and Apparatus Perfection. The Theory and Practice*, 2012, no. 49 (955), pp. 9-17. (Rus).

Received 30.04.2020

E.I. Baida[1]*, Doctor of Technical Science, Associate Professor,*
B.V. Klymenko[1]*, Doctor of Technical Science, Professor,*
S.V. Vyrovets[1]*, Senior Lecturer,*
M.G. Pantelyat[1]*, Candidate of Physics and Mathematics, Associate Professor,*
M. Clemens[2]*, Professor, Dr. rer. nat.*
[1] National Technical University «Kharkiv Polytechnic Institute»,
2, Kyrpychova Str., Kharkiv, 61002, Ukraine,
e-mail: baida.kpi@gmail.com, vsv_2007@ukr.net, m150462@yahoo.com
[2] University of Wuppertal,
Rainer-Gruenter-Straße 21, 42119 Wuppertal, Germany,
e-mail: clemens@uni-wuppertal.de

How to cite this article:
Baida E.I., Klymenko B.V., Vyrovets S.V., Pantelyat M.G., Clemens M. Investigations of the dynamics of a bistable electromagnet with improved characteristics for medium voltage vacuum circuit breakers. *Electrical engineering & electromechanics*, 2020, no. 3, pp. 3-8. **doi: 10.20998/2074-272X.2020.3.01.**

UDC 621.313.33 **doi: 10.20998/2074-272X.2020.3.02**

V.S. Malyar, O.Ye. Hamola, V.S. Maday

MODELLING OF DYNAMIC MODES OF AN INDUCTION ELECTRIC DRIVE AT PERIODIC LOAD

Goal. Development of methods and mathematical models, based on them, for the calculation of transients and steady-state modes of induction electric drives operating in periodic load mode. Methodology. The developed algorithms are based on a mathematical model of an induction motor, which takes into account the saturation of the magnetic core and the displacement of current in the rotor bars. The processes are described by a system of nonlinear differential equations in the orthogonal axes x, y, which enables the results to be obtained with the smallest amount of calculations. The magnetization characteristics by the main magnetic flux and the leakage fluxes are used to calculate the electromagnetic parameters of the motor. To account for the current displacement in the rotor bars, the short-circuited winding is considered as a multilayer structure formed by dividing the bars in height by several elements. Results. Due to the variable load on the motor shaft, electromagnetic processes in both transient and steady state modes of the electric drive in any coordinate system are described by a system of nonlinear differential equations. The result of the calculation of the transients is obtained as a result of their integration time dependencies of coordinates (currents, electromagnetic torque, etc.) at a given law of change of the moment of loading. The proposed method of calculating steady-state mode is based on algebraization of differential equations on the mesh of nodes of the process cyclicity period and allows to obtain periodic dependencies in the time domain. Originality. The problem of calculating a steady-state periodic mode is solved as a boundary problem for a system of first-order differential equations with periodic boundary conditions, which allows to obtain instantaneous dependences during the period of currents, electromagnetic torque, capacities and other coordinates. Practical significance. Using the developed algorithm, it is possible to calculate the static characteristics of periodic processes as dependencies on different parameters of the cycle of periodic load or other coordinates, which is the basis for the choice of the motor for overload, power, heating, etc., as well as to detect the possibility of resonance. References 9, figures 4.

Key words: **induction motor, periodic load, mathematical model, steady-state dynamic mode, transient, static characteristics, saturation of the magnetic core, displacement of current.**

Розроблено математичні моделі і алгоритми, з використанням яких складені програми розрахунку перехідних процесів і усталених режимів асинхронних електроприводів, які працюють в режимі періодичної зміни навантаження. В їх основу покладено математичну модель асинхронного двигуна, розроблену на основі теорії кіл і зображувальних векторів електричних координат, в якій враховується насичення магнітопроводу і витіснення струму в стержнях короткозамкненого ротора. Внаслідок змінного навантаження на валу двигуна електромагнітні процеси як в перехідних, так і усталених режимах в будь-якій системі координат описуються системою нелінійних диференціальних рівнянь. В роботі використано систему ортогональних координатних осей x, y, яка обертається з довільною швидкістю. Для обчислення електромагнітних параметрів двигуна використовуються характеристики намагнічування основним магнітним потоком, а також потоками розсіювання статора і ротора. Для урахування витіснення струму в стержнях ротора короткозамкнена обмотка подається у вигляді багатошарової структури, утвореної розбиттям стержнів по висоті на кілька елементів. Усталений періодичний режим розраховується методом розв'язування крайової задачі, розробленим на основі апроксимації координат кубічними сплайнами, що дає змогу отримати їх періодичні залежності в позачасовій області і розраховувати статичні характеристики як залежності від параметрів циклу періодично-змінного навантаження або інших координат. Бібл. 9, рис. 4.

Ключові слова: **асинхронний двигун, періодичне навантаження, математична модель, усталений динамічний режим, перехідний процес, крайова задача, резонанс, статичні характеристики, насичення магнітопроводу, витіснення струму.**

Разработаны математические модели и алгоритмы, с использованием которых составлены программы расчета переходных процессов и установившихся режимов асинхронных электроприводов, которые работают в режиме периодического изменения нагрузки. В их основу положено математическую модель асинхронного двигателя, разработанную на основе теории цепей и изображающих векторов электрических координат, в которой учитывается насыщение магнитопровода и вытеснение тока в стержнях ротора. Вследствие переменной нагрузки на валу двигателя электромагнитные процессы как в переходных, так установившихся режимах в любой системе координат описываются системой нелинейных дифференциальных уравнений. В работе используется система ортогональных осей x, y, которая вращается с произвольной скоростью. Для вычисления электромагнитных параметров двигателя используются характеристики намагничивания основным магнитным потоком, а также потоками рассеивания статора и ротора. Для учета вытеснения тока в стержнях ротора короткозамкнутая обмотка представляется в виде многослойной структуры, образованной разделением стержней по высоте на несколько элементов. Установившийся периодический режим рассчитывается методом решения краевой задачи, разработанным на основе аппроксимации координат кубическими сплайнами, что дает возможность получить периодические зависимости во вневременной области и рассчитать статические характеристики как зависимости от параметров цикла периодически изменяющейся нагрузки или других координат. Библ. 9, рис. 4.

Ключевые слова: **асинхронный двигатель, периодическая нагрузка, математическая модель, установившийся динамический режим, переходный процесс, статические характеристики, резонанс, насыщение магнитопровода, вытеснение тока.**

Introduction. In modern conditions of development of science and technology, the problem of the development of induction electric drives requires new approaches to their practical implementation, which can be realized only on the basis of the development of adequate mathematical models of electric drive systems that are adapted to their operating conditions. Their use allows not only to correctly select the necessary induction motor (IM), but also to develop a control system under which the motor, operating under these conditions, would ensure the maximum possible efficiency of the electric drive system as a whole.

Modern factory methods make it possible to design an IM that is highly likely to meet the technical conditions of operation in a steady nominal mode with constant load. Such calculations are usually performed using classical substitution circuits [1, 2], but classical substitution circuits are not suitable for the calculation of dynamic modes, and their various adaptations need to be checked on a case-by-case basis.

In the practice of operation, IMs are used not only for actuating mechanisms that operate with unchanged mechanical torque of loading, but also for drives with periodic repeated short-term loading [3, 4]. The duration of the cycle of periodic re-alternating load *T* consists of two parts: the duration of the action of the load pulse and the pause. In particular, for repeated short-term operation (*S*3), the duration of the load pulse is expressed as a percentage to the duration of the full cycle. Switch-on time (ST) = 15; 25; 40; 60 % (e.g. *S*3 – 25 %; *S*3 – 40 %) is considered standard, with a cycle time of 10 minutes [5]. The industry produces IMs to operate in different standard-defined *S*3 modes. The selection of the motor power for the repeated short-term operation mode *S*3 can be made for equivalent power or torque for a given load schedule. Knowing the power of the catalog IM for motors designed to operate in a particular *S*3 mode, it is possible to select a motor to check for starting torque, overload capacity and heating [4].

Both standard long-run motors and motors specially designed for repeated short-term mode can operate in the repeated short-term mode. After all, often the values of the duration of switching on the IM are not standard. There is a need for a comprehensive study of the operation of the motor under the conditions specified by the working mechanism of the periodic load torque, which can be accomplished through mathematical modelling.

The goal of the work is to develop mathematical models for the analysis of the dynamic modes of induction motors operating under conditions of periodic-variable loading.

A mathematical model for the calculation of transients. For the analysis of the operation of electric drives operating in dynamic modes, mathematical models of IM, built on the basis of substituting circuits or linear differential equations (DEs) can be used only for approximate calculations. Because the electromagnetic torque is determined by the flux linkages and currents of the circuits of the motor, the inaccuracy of their determination leads to the inaccuracy of the calculation of the mechanical characteristic [1, 2]. In particular, the value of the inductive resistances of the windings is significantly influenced by the saturation of the magnetic core, the change in the active resistances of the rotor winding due to displacement of current. Taking them into account in dynamic modes with the help of corresponding coefficients [2] does not guarantee the accuracy of the calculation results, especially for deep-slot motors.

The object of study is an IM with short-circuited rotor winding, which is powered by a three-phase network with a symmetric voltage system. For the analysis of electromagnetic processes in IM, we use a mathematical model, created using orthogonal coordinate axes, which allows to consider processes by computer simulation taking into account both saturation and displacement of current in bars of the short-circuit rotor windings with minimal computation. The magnetization characteristics of the main magnetic flux and the scattering fluxes are used to take into account saturation, and to take into account displacement of current the bars are separated by a height into n layers ($2 \le n \le 5$) which results in the n windings being covered by different magnetic scattering fluxes. The calculation algorithms are based on a mathematical model of the IM in the x, y axes, developed on the basis of the theory of imaging vectors [7], which allows to consider processes in the IM based on the theory of circuits.

Dynamics of motion of the rotor of the IM, operating in the mode of periodically variable loading, is described by the system of the DEs of electromechanical equilibrium which in the system of orthogonal axes x, y taking into account the division of each bar in height into n elementary ones, as well as subjecting the image vector of the supply voltage along x axis that is commonly practiced looks like

$$
\begin{gathered}
\frac{d\psi_{sx}}{dt} = -\omega_0\psi_{sy} - R_s i_{sx} + U_m\,; \\
\frac{d\psi_{sy}}{dt} = -\omega_0\psi_{sx} - R_s i_{sy}\,; \\
\frac{d\psi_{1x}}{dt} = (\omega_0 - \omega)\psi_{1y} - R_1 i_{1x}\,; \\
\frac{d\psi_{1y}}{dt} = -(\omega_0 - \omega)\psi_{1x} - R_1 i_{1y}\,; \\
\vdots \\
\frac{d\psi_{nx}}{dt} = (\omega_0 - \omega)\psi_{ny} - R_n i_{nx}\,; \\
\frac{d\psi_{ny}}{dt} = -(\omega_0 - \omega)\psi_{nx} - R_n i_{ny}\,; \\
\frac{d\omega}{dt} = \frac{p_0}{J}\left(\frac{3}{2}p_0\left(\psi_{sx} i_{sy} - \psi_{sy} i_{sx}\right) - M_c(t)\right),
\end{gathered}
\tag{1}
$$

where the indices sx, sy denote that the flux linkages (ψ), currents (i), and active resistances (r) belong to the corresponding stator circuits; and $1x,...,nx$, $1y,...,ny$ to the rotor ones; U_m, ω_0 are the amplitude value and angular frequency of the stator winding phase voltage; ω is the angular velocity of rotation of the rotor; J is the moment of inertia of the moving parts of the electric drive reduced to the shaft of the IM; p_0 is the number of pole pairs.

The loading diagram of the mechanism must be known for modelling. Taking into account that the time dependence of the load torque is periodic, it is necessary to represent it in the form of a law of change, which corresponds to a complete cycle in the form $M_c(t) = M_c(t + T)$, where T is the period.

An algorithm of calculation of characteristics. If the IM operates in one of the standard modes (full cycle is 10 minutes), then the transient is almost complete, and for a complete analysis of the motor operation it is enough to calculate the transient during the period. This can be done by integrating the DE system (1) using the numerical method [6].

DE system (1) includes $2 + 2n$ electrical equilibrium equations and one rotor dynamics equation. Therefore, when calculating the transient, it is necessary to rotate a matrix of the same order at each step (sub-step). In order to reduce the amount of calculations, we reduce the DE system (1), based on the following considerations.

The flux linkages of each IM circuit according to accepted assumptions consists of the sum

$$\psi_j = \psi_{\delta j} + \psi_{\sigma j}$$

of working flux linkage $\psi_{\delta j}$ which is nonlinearly dependent on the currents of all circuits, and scattering flux linkage $\psi_{\sigma j}$ which has a linear dependence, respectively, only on the stator currents or only on the rotor one. In addition, the flux linkage caused by the main work flow and the flux linkage of the slit scattering for all rotor circuits along the x axis are equal. The same applies to similar circuits along the y axis. The above makes it possible to divide the equilibrium equations of the DE system (1) into two parts by distinguishing a linear part in it. For this purpose it is necessary to replace the 5th equation by the difference of the 5th and the 3rd ones, the 6th equation by the difference of the 6th and 4th ones, etc. The first one is of the fourth order

$$\frac{d\psi_{sx}}{dt} = \omega_0\psi_{sy} - R_s i_{sx} + U_m \,;$$

$$\frac{d\psi_{sy}}{dt} = -\omega_0\psi_{sx} - R_s i_{sy} \,;$$

$$\frac{d\psi_{1x}}{dt} = (\omega_0 - \omega)\psi_{1y} - R_1 i_{1x} \,;$$

$$\frac{d\psi_{1y}}{dt} = -(\omega_0 - \omega)\psi_{1x} - R_1 i_{1y}$$

and is nonlinear, and the second of the $2(n–1)$ order is linear

$$\frac{d(\psi_{1x} - \psi_{2x})}{dt} = (\omega_0 - \omega)(\psi_{1y} - \psi_{2y}) - r_1 i_{1x} + r_2 i_{2x} \,;$$

$$\frac{d(\psi_{1y} - \psi_{2y})}{dt} = -(\omega_0 - \omega)(\psi_{1x} - \psi_{2x}) - r_1 i_{1y} + r_2 i_{2y} \,;$$

$$\vdots$$

$$\frac{d(\psi_{1x} - \psi_{nx})}{dt} = (\omega_0 - \omega)(\psi_{1y} - \psi_{ny}) - r_1 i_{1x} + r_n i_{nx} \,;$$

$$\frac{d(\psi_{1y} - \psi_{ny})}{dt} = -(\omega_0 - \omega)(\psi_{1x} - \psi_{nx}) - r_1 i_{1y} + r_n i_{ny} \,.$$

Write these two systems in the form

$$\begin{bmatrix} A_{11} & A_{12} \\ A_{21} & A_{22} \end{bmatrix} \times \begin{bmatrix} d\vec{i}_I/dt \\ d\vec{i}_{II}/dt \end{bmatrix} = \begin{bmatrix} \vec{B}_1 \\ \vec{B}_2 \end{bmatrix}. \qquad (2)$$

Determine the derivative of equation (2)

$$\frac{d\vec{i}_I}{dt} = \left(A_{11} - A_{12}A_{22}^{-1}A_{21}\right)^{-1}\left(\vec{B}_1 - A_{12}A_{22}^{-1}\vec{B}_2\right),$$

in which only the elements of the matrices A_{11} and A_{12} depend on saturation. This allows to calculate the elements of the matrices A_{22}^{-1} and A_{21} once and use them to determine at each step the integration the derivative

$$\frac{d\vec{i}_{II}}{dt} = A_{22}^{-1}\left(\vec{B}_2 - A_{21}\frac{d\vec{i}_I}{dt}\right).$$

Therefore, it is enough to rotate once the matrix of the $2(n–1)$ order and rotate the 4th order matrix at each integration step. The obtained formulas make it possible by numerical methods to reduce to Cauchy form the system (2) of the DEs of the electric equilibrium of the circuits.

Flux linkages of circuits are determined based on the use of magnetization curves by the main magnetic flux ψ_μ and the scattering fluxes of the stator $\psi_{\sigma s}$ and rotor $\psi_{\sigma r}$ windings

$$\psi_\mu = \psi_\mu(i_\mu), \; \psi_{\sigma s} = \psi_{\sigma s}(i_s), \; \psi_{\sigma r} = \psi_{\sigma r}(i_r),$$

where

$$i_\mu = \sqrt{(i_{sx} + i_{rx})^2 + (i_{sy} + i_{ry})^2} \,;$$

$$i_s = \sqrt{i_{sx}^2 + i_{sy}^2} \,; \qquad i_r = \sqrt{i_{rx}^2 + i_{ry}^2} \,.$$

The currents of the rotor circuits are defined as the sum of the currents of n bar elements

$$i_{rx} = \sum_{j=1}^{n} i_{rjx} \,; \qquad i_{ry} = \sum_{j=1}^{n} i_{rjy} \,.$$

A mathematical model for calculating steady-state dynamic mode. In order to reduce the presentation of the computation of the steady-state dynamic calculation algorithm, we write the DE system (1) as a vector equation of the form

$$\frac{d\vec{x}}{dt} = \left(\frac{\partial\vec{y}}{\partial\vec{x}}\right)^{-1} \vec{z}\left(\vec{y}, \vec{x}, \vec{u}, \vec{f}\right), \qquad (3)$$

where $\frac{d\vec{y}}{dt} = \begin{bmatrix} L_{xy} & 0 \\ 0 & 1 \end{bmatrix}$ is the matrix in which $L_{xy} = \frac{d\vec{\psi}}{d\vec{i}}$ is the complete matrix of differential inductances of the IM in coordinate axes x, y [7];

$$\vec{y} = \begin{bmatrix} \psi_{sx} \\ \psi_{sy} \\ \psi_{1x} \\ \psi_{1y} \\ \vdots \\ \psi_{nx} \\ \psi_{ny} \\ \omega \end{bmatrix}; \quad \vec{u} = \begin{bmatrix} U_m \\ 0 \\ 0 \\ 0 \\ \vdots \\ 0 \\ 0 \\ 0 \end{bmatrix}; \quad \vec{f} = \begin{bmatrix} 0 \\ 0 \\ 0 \\ 0 \\ \vdots \\ 0 \\ 0 \\ M_c(t) \end{bmatrix}; \quad \vec{x} = \begin{bmatrix} i_{sx} \\ i_{sy} \\ i_{1x} \\ i_{1y} \\ \vdots \\ i_{nx} \\ i_{ny} \\ \omega \end{bmatrix}.$$

In steady state mode of the electric drive system with periodic change of the load torque $M(t) = M(t + T)$ flux linkages, currents, rotor speed, electromagnetic torque, etc. are varied by periodic laws. The task of calculating a periodic mode is to determine these dependencies. The solution of the system of equations (3) is the periodic dependencies of the components of the vector $\vec{x}(t)=\vec{x}(t+T)$. The calculation by the stable method is inefficient for many reasons. In particular, CPU time is wasted, and if the process is becomes stable too slowly, then the oscillations at time t are little different from those for time $t + T$, so there is a problem of determining the time when the transient ends. Finally, the stable method is practically unsuitable for optimization calculations.

The most effective approach to calculating a steady periodic mode is to consider the problem as a boundary one [7], which allows to obtain periodic dependencies of coordinates in the timeless domain, that is, without resorting to the calculation of the transient. To do this, the system of continuous DEs (1) must be reduced to discrete ones, which are a point mapping of the dependencies of the coordinates during the process repetition period. There are many methods of algebraization in the literature that have both positive and negative sides: difference, collocation, including trigonometric, differential transformations, etc. The method, based on spline approximations of coordinates, developed in [8], makes it possible to formalize the algebraization process and is also numerically stable. It allows to obtain continuous dependencies of coordinates on a period on the basis of the obtained by calculation their discrete values in nodes of a mesh on a period. Note that the mesh of nodes can be taken uniformly. In the system of algebraic equations obtained by the approximation of variables, the values of the coordinates in m nodes of the period are unknown. As a result, taking into account periodic boundary conditions $\vec{Y}(t)=\vec{Y}(t+T)$, $\vec{X}(t)=\vec{X}(t+T)$, we obtain the system of $m\times(2n+3)$ nonlinear algebraic equations, which can be represented as a vector equation

$$\vec{Y}(\vec{X})=H^{-1}\vec{Z}(\vec{Y},\vec{X}), \tag{4}$$

in which H is the square matrix of size $m(3+2n)$ of transition from continuous change of coordinates to their nodal values, whose elements are determined only by the mesh step [8]; $\vec{Y}=(\vec{y}_1,\ldots,\vec{y}_m)$, $\vec{Z}=(\vec{z}_1,\ldots,\vec{z}_m)$, $\vec{X}=(\vec{x}_1,\ldots,\vec{x}_m)$ are the vectors made up of values of vectors $\vec{y}$, $\vec{x}$, $\vec{z}$ in m nodes of the period.

By defining from vector (4) the vector $\vec{X}$, it is possible to construct periodic dependencies of all coordinates, including electromagnetic of torque, power, etc.

Direct application of the iterative method to the solution of system (4) is practically impossible due to the divergence of the iterative process. A reliable method of solving the problem is the method of continuation by parameter [9]. However, in the system of nonlinear algebraic equations there are two disturbing actions: applied voltage – vector $\vec{U}=(\vec{u}_1,\ldots,\vec{u}_m)$ and vector of nodal values of load torque – $\vec{F}=(\vec{f}_1,\ldots,\vec{f}_m)$. It is impossible to increase them at the same time, so the problem is solved in two stages, the essence of which is to increase them alternately in proportion to a certain parameter. First, we increase the applied voltage, and then, taking it unchanged, we increase the nodal values of the applied torque. This makes it possible to determine the time dependencies of the coordinates in the steady-state periodic mode of operation of the IM at a given law of change of the applied torque.

The steady-state mode calculation algorithm is the basis for the calculation of static characteristics, which can be obtained as a sequence of steady-state modes calculated with a set of coordinate values, which is taken as an independent variable, which can be any value: moment of inertia, pulse density of the load torque; ratio between pulse duration and pause, pulse rate, maximum and minimum torque, period duration, etc. In addition, under cyclic loading mechanical resonance is possible, which can be detected by mathematical modelling.

The problem of calculating static characteristics can be solved by a differential method, the essence of which is the differentiation of algebraic equation (4) on an independent variable, for example ε, as a parameter. As a result of differentiation, we obtain a nonlinear system of DE in the form

$$A\frac{d\vec{X}}{d\varepsilon}=\frac{\partial\vec{Z}}{\partial\varepsilon}. \tag{5}$$

The static multidimensional characteristic as a dependence of periodic curves on the independent variable ε is obtained by integrating system (5) with parameter ε. The initial conditions should be those obtained as a result of the first stage of the calculation at a given supply voltage. At each integration step, the result can be refined by the Newton method. During integration as well as iterative refinement, it is necessary to determine the differential inductance of circuits as nonlinear functions of currents.

Results of investigations. Below are examples of calculation results performed using the above algorithms on the example of the IM with short-circuited rotor 4AP160S4Y3 (P = 15 kW, U = 220 V, I = 29.9 A, p_0 = 2).

Figure 1 shows the time dependences of the relative values of the electromagnetic torque (Fig. 1,*a*) and the current value (Fig. 1,*b*) in the transient during start up of the IM with cyclic loading, at which the torque of load varies with the period T = 0.16 s in the range from idling to nominal value, the moment of inertia J = 0.5 kg·m^2, and the density is 60 %, and Fig. 2 presents the same dependencies, but with less moment of inertia J = 0.1 kg·m^2.

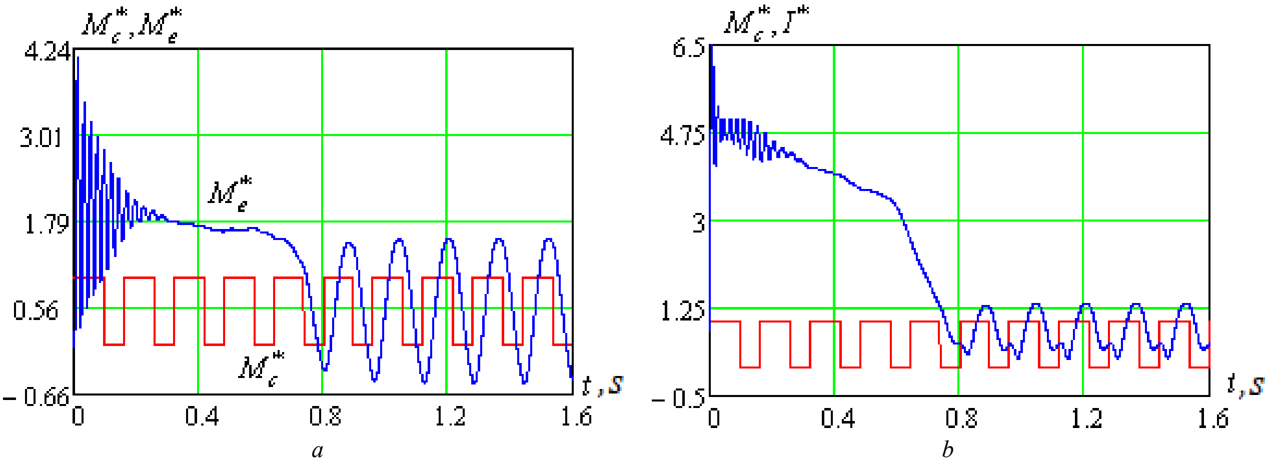

a *b*

Fig. 1

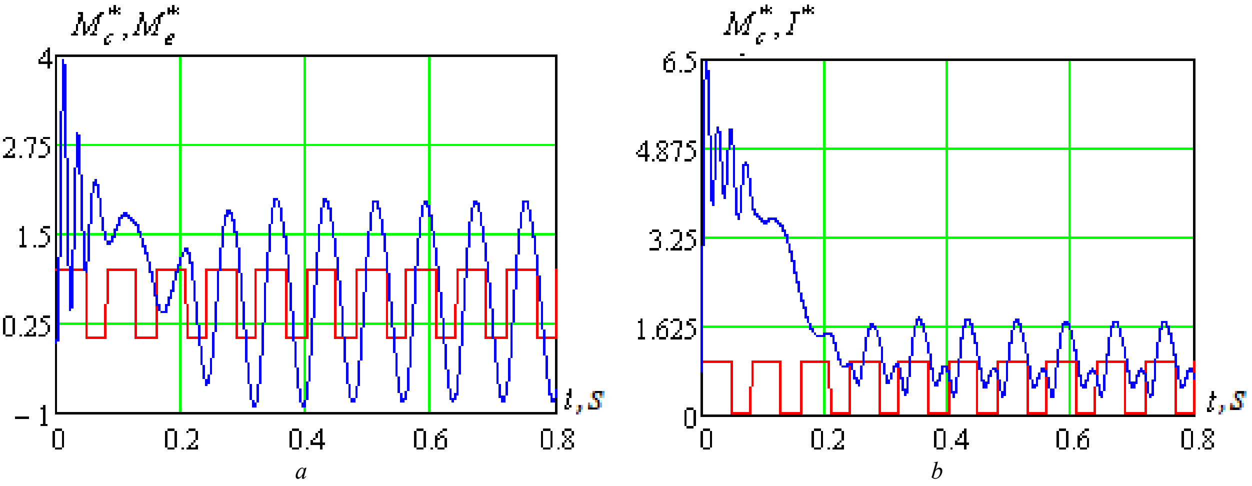

a *b*

Fig. 2

Figures 3, 4 present an example of calculated by the method of solving the boundary value problem of periodic curves of current, electromagnetic torque and load, presented in this work which correspond dependencies in steady state shown in Fig. 2.

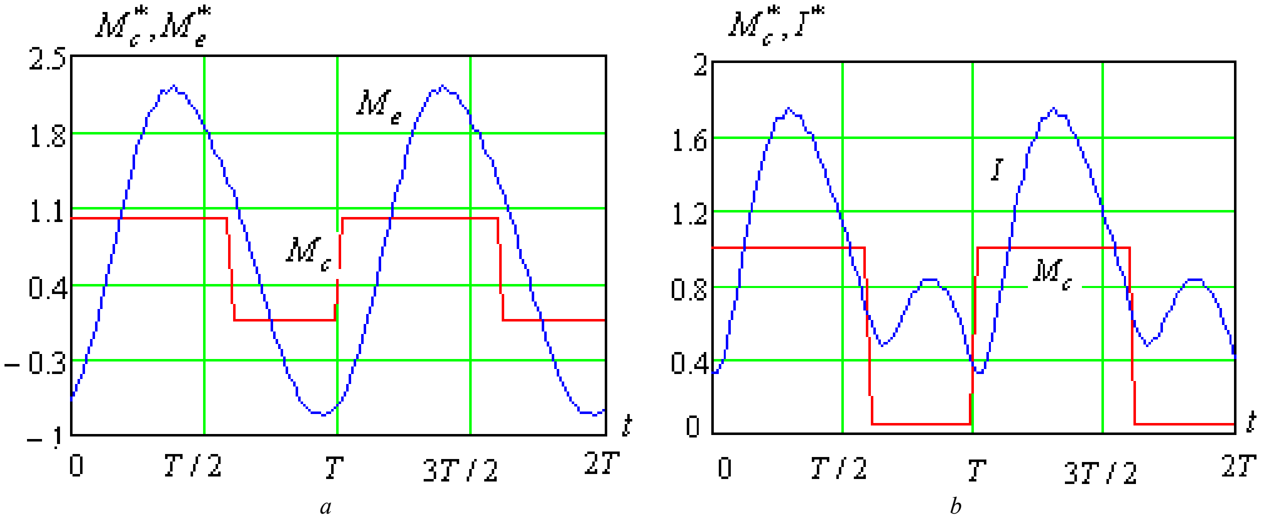

a *b*

Fig. 3. Periodic dependencies (two periods shown) of the relative values of the load torque (M_c^*), electromagnetic torque (M_e^*) and current (I^*) calculated at the moment of inertia $J = 0.1$ kg·m^2 by the method of solving the boundary value problem

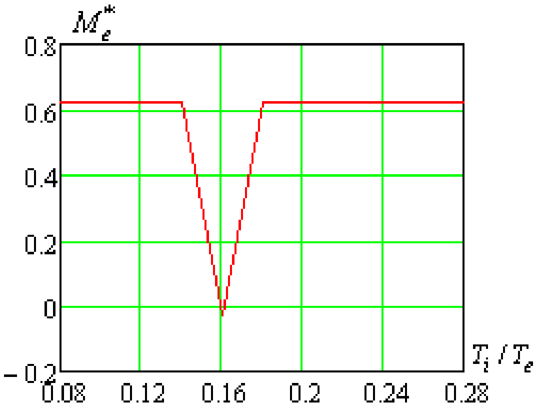

Fig. 4. Dependence of the electromagnetic torque of the motor on the relative value of the duration of the period of change of load (at the point T_i/T_e = 0.16 there is a mechanical resonance)

Conclusions.

1. The developed calculation methods and corresponding algorithms make it possible to use mathematical modelling to analyze the operation of induction motors with a short-circuited rotor taking into account the saturation and displacement of currents in the rotor bars under different laws of change of periodic load.
2. The algorithm of calculation of the steady-state periodic modes at cyclic loading allows to obtain the periodic dependencies of coordinates in the timeless domain, which ensures high speed.
3. The mathematical models developed can be used to design and analyze the operation of electric drives with periodic load.

REFERENCES

1. Voldek A.I., Popov V.V. *Elektricheskiye mashiny. Mashiny peremennogo toka* [Electric machines. AC machines]. Saint Petersburg, Piter Publ., 2010. 350 p. (Rus).

2. Safaryan V.S., Gevorgyan S.G. Ascertainment of the equivalent circuit parameters of the asynchronous machine. *Energetika. Proceedings of CIS higher education institutions and power engineering associations*, 2015, no. 6, pp. 20-34. (Rus).

3. Rogal V.V., Kapshtik V.S. Reactive power compensation in intermittent duties. *Electronics and Communication. Thematic issue «Electronics and Nanotechnology»*, 2011, no. 3, pp. 101-108. (Ukr).

4. Petrushin V.S., Plotkin J.R., Yenoktaiev R.N., Bendahmane Boukhalfa. Development of energy–efficient asynchronous electric drive for intermittent operation. *Bulletin of the National Technical University «KhPI». Series: Problems of automated electrodrive. Theory and practice*, 2019, no. 16 (1341), pp. 70-79. **doi: 10.20998/2079-8024.2019.16.13**.

5. Petuhov S.V., Krishyanis M.V. *Elektroprivod promyishlennyih ustanovok* [Electric driver industrial-scale plants]. Arkhangelsk, S(A)FU Publ., 2015. 303 p. (Rus).

6. Hrisanov V.I. Transient process analysis at various methods of starting asynchronous machines. *Technical electrodynamics. Thematic issue «Electric drive»*, 2000, pp. 24-27. (Rus).

7. Fil'ts R.V. *Matematicheskie osnovy teorii elektromekhanicheskikh preobrazovatelei* [Mathematical foundations of the theory of electromechanical transducers]. Kyiv, Naukova dumka Publ., 1979. 208 p. (Rus).

8. Malyar V.S., Malyar A.V. Mathematical modeling of periodic modes of operation of electrical devices. *Electronic Modeling*, 2005, vol.27, no.3, pp. 39-53. (Rus).

9. Zhulin S.S. The method of continuation by parameter and its application to the tasks of optimal control. *Numerical methods and programming*, 2007, vol. 8, no. 2, pp. 205-217. (Rus).

Received 11.02.2020

V.S. Malyar[1], *Doctor of Technical Science, Professor,*
O.Ye. Hamola[1], *Candidate of Technical Science, Associate Professor,*
V.S. Maday[1], *Candidate of Technical Science, Associate Professor,*
[1] Lviv Polytechnic National University,
12, S. Bandera Str., Lviv, 79013, Ukraine,
e-mail: vasyl.s.maliar@lpnu.ua,
orest.y.hamola@lpnu.ua,
volodymyr.s.madai@lpnu.ua

How to cite this article:
Malyar V.S., Hamola O.Ye., Maday V.S. Modelling of dynamic modes of an induction electric drive at periodic load. *Electrical engineering & electromechanics*, 2020, no. 3, pp. 9-14. **doi: 10.20998/2074-272X.2020.3.02.**

UDC 621.3.013 **doi: 10.20998/2074-272X.2020.3.03**

B.I. Kuznetsov, T.B. Nikitina, I.V. Bovdui

THE EFFECTIVENESS OF ACTIVE SHIELDING OF MAGNETIC FIELD WITH CIRCULAR SPACE-TIME CHARACTERISTIC AND WITH DIFFERENT SHIELDING COILS SPATIAL POSITIONS

Aim. The synthesis, computer modeling and field experimental research of two degree of freedom robust two circuit system of active shielding of magnetic field with circular space-time characteristic, generated by overhead power lines with «triangle» type of phase conductors arrangements and with different shielding coils spatial positions for reducing the magnetic flux density to the sanitary standards level and to reducing the sensitivity of the system to plant parameters uncertainty. Methodology. The synthesis is based on the multi-criteria game decision, in which the payoff vector is calculated on the basis of the Maxwell equations quasi-stationary approximation solutions. The game decision is based on the stochastic particles multiswarm optimization algorithms. The initial parameters for the synthesis by system of active shielding are the location of the overhead power lines with respect to the shielding space, geometry and number of shielding coils, operating currents, as well as the size of the shielding space and magnetic flux density normative value, which should be achieved as a result of shielding. The objective of the synthesis is to determine their number, configuration, spatial arrangement and shielding coils currents, the control systems parameters as well as the resulting of the magnetic flux density value at the shielding space. Results. Computer simulation and field experimental research results of two degree of freedom robust two circuit system of active shielding of magnetic field, generated by overhead power lines with «triangle» type of phase conductors arrangements and with different shielding coils spatial positions are given. The possibility of initial magnetic flux density level reducing and system sensitivity to the plant parameters uncertainty reducing is shown. Originality. For the first time the synthesis, theoretical and experimental research of two degree of freedom robust two -circuit t system of active shielding of magnetic field generated by single-circuit overhead power line with phase conductor's triangular arrangements and with different shielding coils spatial positions carried out. Practical value. Practical recommendations from the point of view of the practical implementation on reasonable choice of the spatial arrangement of two shielding coils of robust two -circuit system of active shielding of the magnetic field with circular space-time characteristic generated by single-circuit overhead power line with phase conductor's triangular arrangements are given. References 32, figures 20.

Key words: **overhead power lines with «triangle» type of phase conductors arrangements, magnetic field, system of active shielding, computer simulation, field experimental research.**

Цель. Синтез, компьютерное моделирование и полевые экспериментальные исследования комбинированной робастной двухконтурной системы активного экранирования магнитного поля с круговой пространственно-временной характеристикой, генерируемого одноконтурной воздушной линией электропередачи с треугольным подвесом проводов, и с различным пространственным расположением экранирующих обмоток для снижения индукции магнитного поля до уровня санитарных норм и для снижения чувствительности системы к неопределенности параметров объекта управления. Методология. Синтез основан на решении многокритериальной стохастической игры, в которой векторный выигрыш вычисляется на основании решений уравнений Максвелла в квазистационарном приближении. Решение игры находится на основе алгоритмов стохастической мультиагентной оптимизации мультироем частиц. Исходными параметрами для синтеза системы активного экранирования являются расположение высоковольтной линий электропередачи по отношению к экранируемому пространству, ее геометрические размеры, количество проводов и рабочие токи линии электропередачи, размеры экранируемого пространства и нормативное значение индукции магнитного поля, которое должно быть достигнуто в результате экранирования. Задачей синтеза является определение количества, конфигурации, пространственного расположения и значения токов в экранирующих обмотках, параметры системы управления, а также результирующего значения индукции магнитного поля в экранируемом пространстве. Результаты. Приводятся результаты компьютерного моделирования и полевых экспериментальных исследований комбинированной робастной двухконтурной системы активного экранирования магнитного поля, генерируемого воздушной линией электропередачи с треугольным подвесом проводов, и с различным пространственным расположением экранирующих обмоток. Показана возможность снижения уровня индукции исходного магнитного поля внутри экранируемого пространства и снижения чувствительности системы к неопределенностям параметров объекта управления. Оригинальность. Впервые проведены синтез, теоретические и экспериментальные исследования комбинированной робастной двухконтурной системы активного экранирования магнитного поля, генерируемого одноконтурной воздушной линией электропередачи с треугольным подвесом проводов. Практическая ценность. Приводятся практические рекомендации по обоснованному выбору с точки зрения практической реализации пространственного расположения двух экранирующих обмоток двухконтурной робастной системы активного экранирования магнитного поля с круговой пространственно-временной характеристикой, создаваемого одноконтурной воздушной линией электропередачи с треугольным подвесом проводов. Библ. 32, рис. 20.

Ключевые слова: **воздушная линия электропередач, подвес проводов типа «треугольник», магнитное поле, система активного экранирования, компьютерное моделирование, полевые экспериментальные исследования.**

Introduction. World Health Organization experts have identified the carcinogenic properties of the power frequency (PF) magnetic field (MF). Therefore, in the world over the past 15 years, sanitary standards are constantly tightening at the maximum permissible level of MF induction of 50–60 Hz and intensive research is being conducted on the development of methods for MF normalization. Overhead power lines (OPL) are one of the most dangerous for people sources of PF MF [1, 2].

Active contour shielding of PF MF generated by OPL [3, 4] is the most acceptable and economically feasible for ensuring the sanitary norms of Ukraine in the PF MF. The methods of synthesis of systems of active shielding (SAS) for MF, generate by OPL, developed in [5-8].

Single-circuit SAS with single SC is most widely used in world practice [3]. Such SAS can effectively shielded by MF with a small polarization. The space-time characteristics (STC) of such MF is a very elongated ellipse whose ellipse coefficient (ratio of the smaller axis to the larger axis) is seeks to zero. Single SC of single-circuit OPL generates MF, whose STC is a straight line. With such a single- circuit SAS with single SC, the major axis of the STS ellipse of the initial MF is compensated, so that the STS of the total MP with SAS is on is significantly smaller than the STS of the initial MF, which determines the high shielding factor of such single-circuit SAS. Single-circuit OPL with horizontal and vertical bus arrangement, double-circuit OPL such as «barrel», «tree» and «inverted tree», and groups of OPL generates a MF with a weak polarization.

However, the single-circuit OPL with phase conductor's triangular arrangements generated most polarized MF. The STC of such MF is practically a circle. Therefore, for effective shielding of such MF it is necessary to have two SC at least [5]. Note that the vast majority of single-circuit OPL in Ukraine has just such phase conductors triangular arrangements.

The goal of this work is the synthesis, computer modeling and field experimental research of two degree of freedom robust two circuit system with different both shielding coils spatial positions for active shielding of magnetic field with circular space-time characteristic, generated by overhead power lines with «triangle» type of phase conductors arrangements for reducing the magnetic flux density to the sanitary standards level and to reducing the sensitivity of the system to plant parameters uncertainty.

Problem statement. The initial data for the synthesis of the SAS are the parameters of the transmission lines (working currents, geometry and number of wires, location of the transmission lines relative to the protected space) and the dimensions of the shielding space and magnetic flux density sanitary standards level, which should be achieved as a result of shielding [12-22]. In the process of synthesis, it is necessary to determine the parameters of the shielding coils (SC) (their number, configuration, and spatial arrangement), currents and the resulting magnetic flux density level. To shielding factor improvement two degree of freedom SAS are used in which simultaneously used feed back regulator for closed loop control and feed forward regulator for open loop control [22-26].

Two degree of freedom robust SAS synthesizing problem reduced [27, 28] to the determination of such SC spatial arrangement and geometric sizes, as well as parameters of the regulator vector and uncertainty parameters vector, which the maximum value of the magnetic flux density in the shielding space points assumes a minimum value for the SC spatial arrangement and geometric sizes parameters vector but the maximum value for the uncertainty parameters vector [28]. The two degree of freedom robust SAS includes open loop and closed loop control. The synthesis of such two degree of freedom robust SAS is based on the multi-criteria game decision [29-31], in which the payoff vector calculated on the basis of the Maxwell equations quasi-stationary approximation solutions [1, 2]. The game decision based on the stochastic particles multiswarm optimization algorithms [32].

Computer simulation results. Consider the results of the two degree of freedom robust two circuit SAS synthesis of MF with circular space-time characteristic generated by 110 kV OPL with triangular conductors arrangement in a single-story building located at a distance of 10 m from OPL. In Fig. 1 are shown location of OPL and shielding space (SS) in which MF must mitigated to the sanitary norms level. In Figure 1 also are shown location of both SC. SC upper parts are coordinates (3.0416, 3.4965) and (7.1943, 3.6818). SC lower parts are coordinates (6.3707, 0.6637) and (2.8478, 2.4522).

At 250 A OPL current, its necessary 86.2448 and 86.2768 amperes of turns (AT) in SC. Phase current shifts are 0.8074 rad and 1.2043 rad.

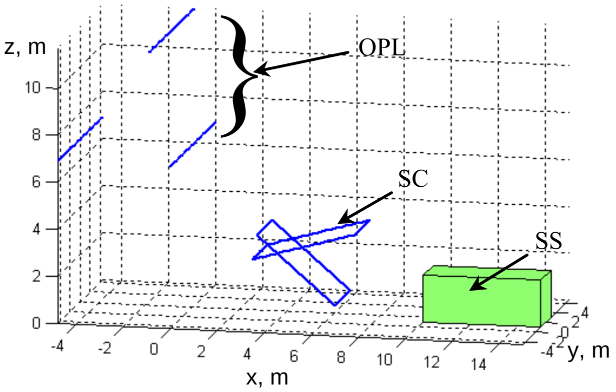

Fig. 1. The location of 110 kV overhead power line with phase conductors triangular arrangements, both shielding coils and shielding space

In Figure 2 are shown comparison of magnetic flux density between working SAS with and without SAS. The initial magnetic flux density level in shielding space is 0.75 μT. When the SAS is on, the magnetic flux density level in shielding space is reduced to 0.12 μT. Therefore, the shielding factor is 6.25.

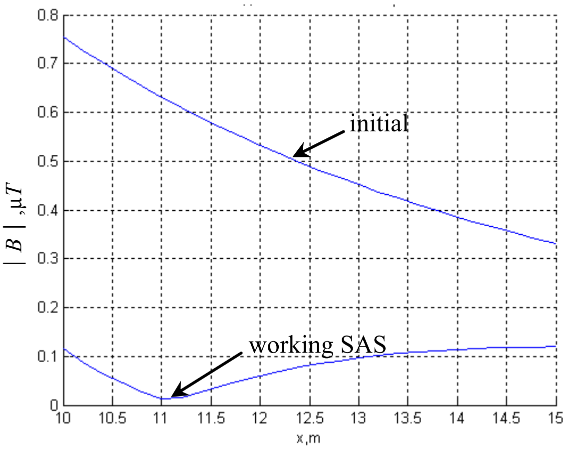

Fig. 2. Comparison of magnetic flux density between with and without system of active shielding

In Figure 3 are shown the MF STC, generated by OPL (1); both SC (2) and total MF with SAS is on (3). The STC of initial MF generated by OPL with phase conductors triangular arrangements close to the circle. STC of MF generated by both SC is also close to the circle of the STC of initial MF, which ensures high shielding factor.

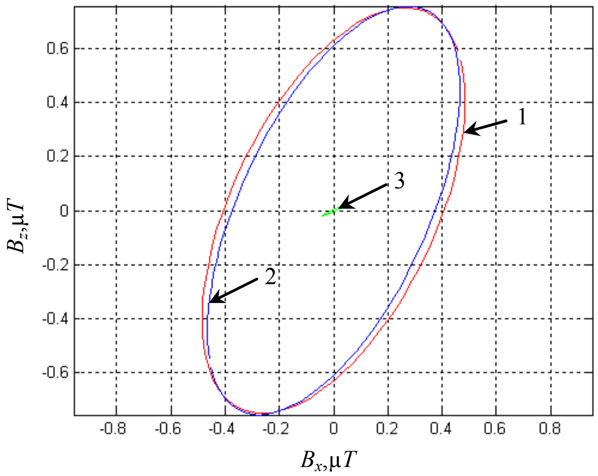

Fig. 3. Comparison of space-time characteristics of magnetic flux density between with and without system of active shielding and both shielding coils

However, STC of MF generated separately by only single first SC or only single second SC are straight lines. Naturally, the STC of the resulting MF generated by OPL and only single SC is an ellipse, which will be shielded by another SC. In Figure 4 are shown the STC of the initial MF generated by OPL, shielding MF generated by only single first SC and the resulting MF when only single first SC is used.

As can seen from Fig. 4, the STC of the resulting MF is a strongly elongated ellipse, the semi-major axis of which is almost two times larger than the STC of the initial MF, and therefore, due to only single first SC work, initial MF is almost twice re compensated.

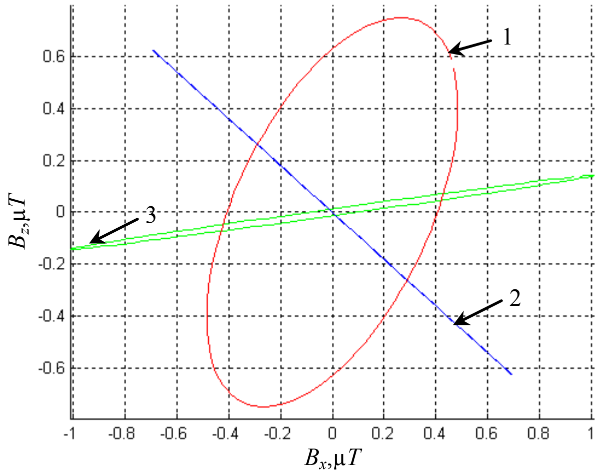

Fig. 4. Comparison between space-time characteristics of magnetic flux density without and with system of active shielding with only single first shielding coil and only single first shielding coil

However, then after second SC switching resulting MF STC becomes significantly less than the STC of initial MF, which ensures high shielding factor. Note that the STC of the resulting MF, left after the operation of only single first SC, practically parallel with the STC generated by the MF using only single second SC.

In Figure 5 are shown the STC of the initial MF generated by OPL, shielding MF generated by only single second SC and the resulting MF when only single second SC is used.

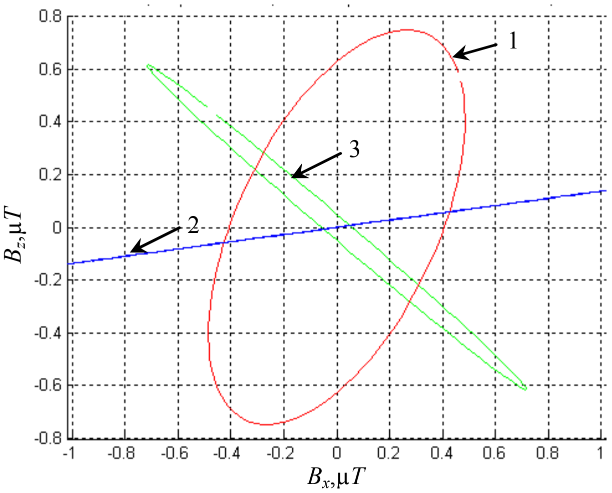

Fig. 5. Comparison between space-time characteristics of magnetic flux density without and with system of active shielding with only single second shielding coil and only single second shielding coil

As can seen from Fig. 4 and Fig. 5, STC of MF generated separately by only single first SC, or only single second SC are straight lines. However, STC of the resulting MF, which left after the operation of only single first (or second) SC, practically parallel with the MF STC of MF, generated by using only single second (or first) SC. It is the STC arrangement that provides ensures high shielding factor, when both SC work simultaneously.

Notice, that the initial magnetic flux density level ranges from 0.75 μT to 0.35 μT in all shielding space, as can be seen from Fig. 2. When SAS is on, the magnetic flux density level does not exceed 0.12 μT in all shielding space, as can be seen from Fig. 2.

However, when SAS is on and with only single first SC is used, the magnetic flux density level ranges from 1.5 μT to 0.3 μT in all shielding space. Consequently, when SAS is on and with only single first SC is used initial magnetic flux density level more than double due to overcompensation.

However, when SAS is on and with only single second SC is used, the magnetic flux density level ranges from 2 μT to 0.4 μT in all shielding space. Consequently, when SAS is on and with only single second SC is used initial magnetic flux density level also more than 2.5 due to recompensation. However, when SAS is on and with both first SC and second SC is used, the magnetic flux density level does not exceed 0.12 μT in all shielding space. Consequently, when SAS is on and with both first SC and second SC is used shielding factor is 6.25.

Notice also, that initial magnetic flux density level overcompensation effect with only single first SC also follows from comparison between MF STC without and with SAS with only single first SC. Similarly initial magnetic flux density level overcompensation effect with only single second SC also follows from comparison between MF STC without and with SAS with only single second SC.

Magnetic flux density level sanitary norms of Ukraine are 0.5 μT. When the SAS is on, the magnetic flux density level in shielding space is reduced to 0.12 μT at 250 A OPL current. Consider the results of the SAS synthesis at 700 A OPL current. In Fig. 6 are shown location of OPL and shielding space in which MF must mitigated to the sanitary norms level and location of both SC. SC upper parts are coordinates (2, 4) and (6, 3.1031). The SC lower parts are coordinates (6.6897, 1.5394) and (2, 0).

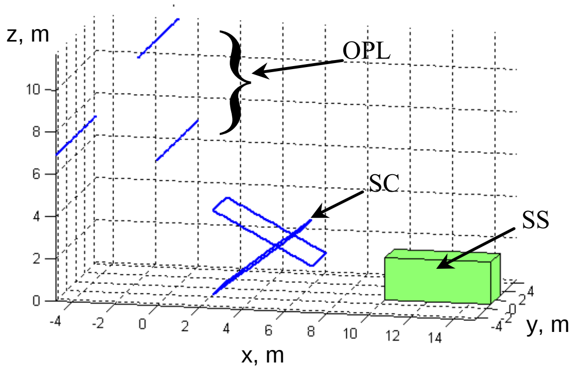

Fig. 6. The location of 110 kV overhead power line with phase conductors triangular arrangements, both shielding coils and shielding space

At 750 A OPL current, its necessary 158.9729 and –178.5417 AT in SC. Phase Current Shifts are 0.6934 rad and 1.5959 rad. In Figure 7 are shown comparison of magnetic flux density between with and without SAS. The initial magnetic flux density level in shielding space is 2.25 μT. When the SAS is on, the magnetic flux density level in shielding space is reduced to 0.55 μT. Therefore, the shielding factor is 4.1.

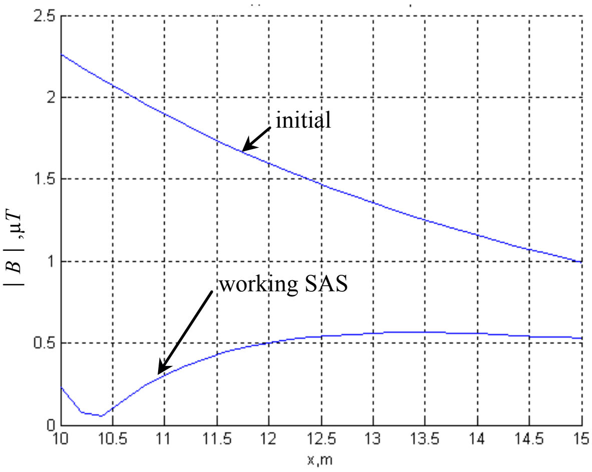

Fig. 7. Comparison of magnetic flux density between with and without system of active shielding

In Figure 8 are shown the MF STC, generated by OPL (1); both SC (2) and total MF with SAS is on (3).

The STC of initial MF generated by OPL with phase conductors triangular arrangements close to the circle. STC of MF generated by both SC is also close to the circle of the STC of initial MF, which ensures high shielding factor.

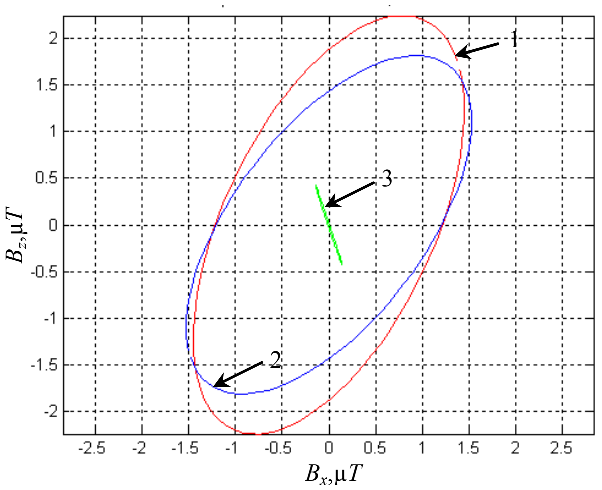

Fig. 8. Comparison of space-time characteristics of magnetic flux density between with and without system of active shielding and both shielding coils

The STC of the resulting MF generated by OPL and only single SC is an ellipse, which will be shielded by another SC. In Figure 9 are shown the STC of the initial MF generated by OPL, shielding MF generated by only single first SC and the resulting MF when only single first SC is used. The STC of the resulting MF is a strongly elongated ellipse, the semi-major axis of which is almost two times larger than the STC of the initial MF, and therefore, due to only single first SC work, initial MF is almost twice re compensated. However, then after second SC switching resulting MF STC becomes significantly less than the STC of initial MF, which ensures high shielding factor. Note that the STC of the resulting MF, left after the operation of only single first SC, practically parallel with the STC generated by the MF using only single second SC.

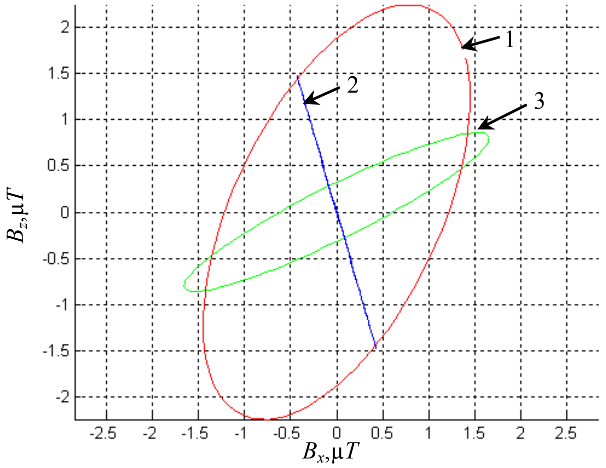

Fig. 9. Comparison between space-time characteristics of magnetic flux density without and with system of active shielding with only single first shielding coil and only single first shielding coil

In Figure 10 are shown the STC of the initial MF generated by OPL, shielding MF generated by only single second SC and the resulting MF when only single second SC is used.

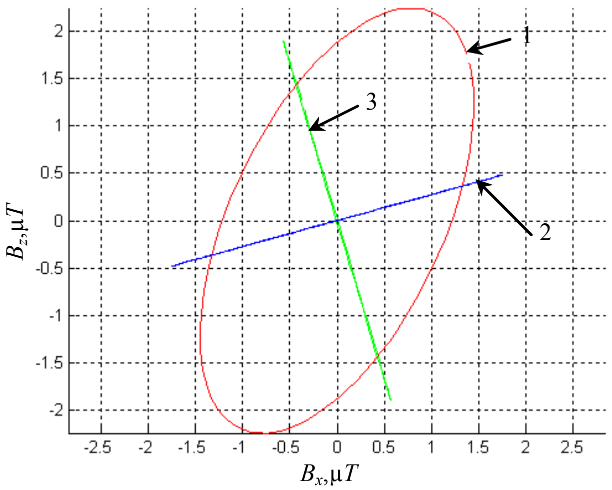

Fig. 10. Comparison between space-time characteristics of magnetic flux density without and with system of active shielding with only single second shielding coil and only single second shielding coil

The initial magnetic flux density level ranges from 2.25 μT to 1 μT in all shielding space, as can be seen from Fig. 7. However, when SAS is on and with only single first SC is used, the magnetic flux density level ranges from 2 μT to 0.8 μT in all shielding space. When SAS is on and with only single second SC is used, the magnetic flux density level ranges from 3.5 μT to 1.2 μT in all shielding space. Consequently, when SAS is on and with only single second SC is used initial magnetic flux density level also more than 1.5 due to recompensation. However, when SAS is on and with both first SC and second SC is used, the magnetic flux density level does not exceed 0.55 μT in all shielding space. Consequently, when SAS is on and with both first SC and second SC is used shielding factor is 4.1.

At 750 A OPL current when the SAS is on the magnetic flux density level in shielding space is reduced to 0.55 μT, which exceeds the magnetic flux density level sanitary norms of Ukraine is 0.5 μT. So consider the results of the SAS synthesis at 625 A OPL current. In Fig. 11 are shown location of OPL and shielding space in which MF must mitigated to the sanitary norms level and location of both SC. SC upper parts are coordinates (8.544, 2.6895) and (3.069, 2.8128). SC lower parts are coordinates (4.8693, 0.1461) and (8.4686, 0.2538). At 750 A OPL current, its necessary 77.5265 and –73.1804 AT in SC. Phase current shifts are 1.1091 rad and 0.8583 rad.

In Figure 12 are shown comparison of magnetic flux density between with and without SAS. The initial magnetic flux density level in shielding space is 1.9 μT. When the SAS is on, the magnetic flux density level in shielding space is reduced to 0.4 μT. Therefore, the shielding factor is 4.75.

In Figure 13 are shown the MF STC, generated by OPL (1); both SC (2) and total MF with SAS is on (3).

The STC of initial MF generated by OPL with phase conductors triangular arrangements close to the circle. STC of MF generated by both SC is also close to the circle of the STC of initial MF, which ensures high shielding factor.

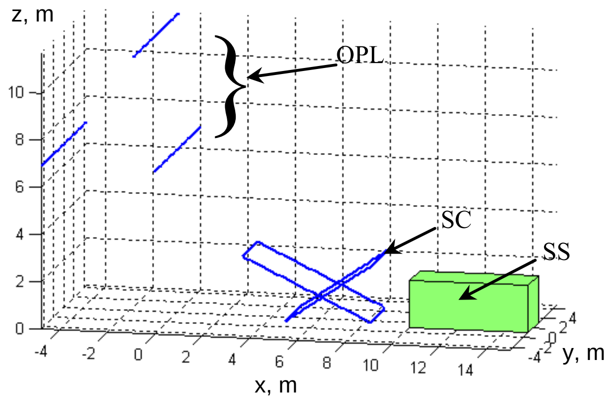

Fig. 11. The location of 110 kV overhead power line with phase conductors triangular arrangements, both shielding coils and shielding space

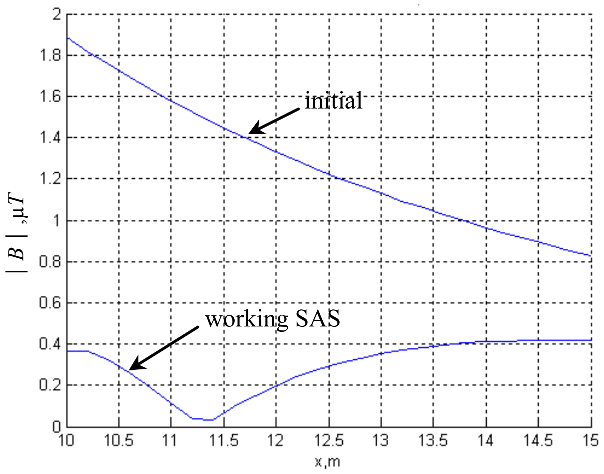

Fig. 12. Comparison of magnetic flux density between with and without system of active shielding

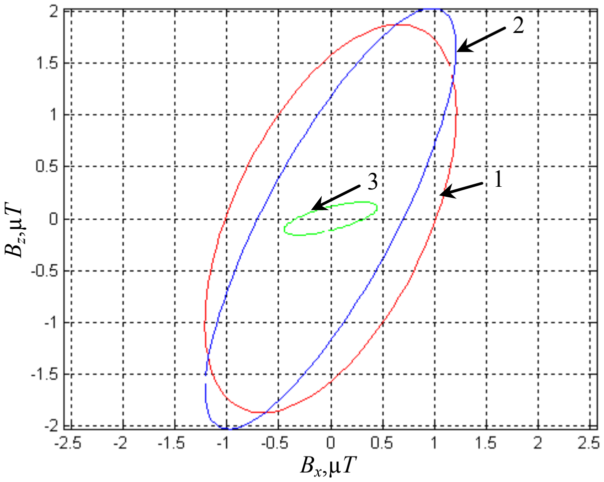

Fig. 13. Comparison of space-time characteristics of magnetic flux density between with and without system of active shielding and both shielding coils

The STC of the resulting MF generated by OPL and only single SC is an ellipse, which will be shielded by another SC. In Figure 14 are shown the STC of the initial MF generated by OPL, shielding MF generated by only single first SC and the resulting MF when only single first SC is used.

As can seen from Fig. 14, the STC of the resulting MF is a strongly elongated ellipse, the semi-major axis of which is almost two times larger than the STC of the initial MF, and therefore, due to only single first SC work, initial MF is almost twice re compensated. However, then after second SC switching resulting MF STC becomes significantly less than the STC of initial MF, which ensures high shielding factor. Note that the STC of the resulting MF, left after the operation of only single first SC, practically parallel with the STC generated by the MF using only single second SC.

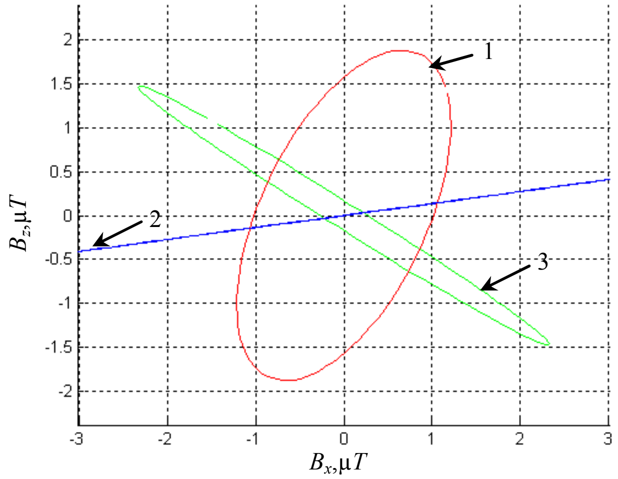

Fig. 14. Comparison between space-time characteristics of magnetic flux density without and with system of active shielding with only single first shielding coil and only single first shielding coil

In Figure15 are shown the STC of the initial MF generated by OPL, shielding MF generated by only single second SC and the resulting MF when only single second SC is used.

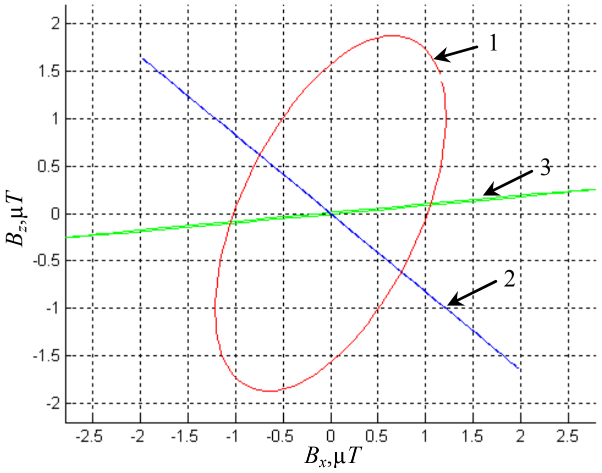

Fig. 15. Comparison between space-time characteristics of magnetic flux density without and with system of active shielding with only single second shielding coil and only single second shielding coil

At 625 A OPL current the initial magnetic flux density level ranges from 2 μT to 0.9 μT in all shielding space, as can be seen from Fig. 2. However, when SAS is on and with only single first SC is used, the magnetic flux density level ranges from 4 μT to 0.7 μT in all shielding space. Consequently, when SAS is on and with only single first SC is used initial magnetic flux density level more than double due to overcompensation.

However, when SAS is on and with only single second SC is used, the magnetic flux density level ranges from 5 μT to 1 μT in all shielding space. Consequently, when SAS is on and with only single second SC is used initial magnetic flux density level also more than double due to recompensation. However, when SAS is on and with both first SC and second SC is used, the magnetic flux density level does not exceed 0.4 μT in all shielding space. Consequently, when SAS is on and with both first SC and second SC is used shielding factor is 4.75.

The initial magnetic flux density level overcompensation effect with only single first SC also follows from comparison between MF STC without and with SAS with only single first SC, which Fig. 14 shows. Similarly initial magnetic flux density level overcompensation effect with only single second SC also follows from comparison between MF STC without and with SAS with only single second SC, which in Fig. 15 are shown.

To realize the SAS according to the first option of SC spatial arrangement which is shown in Fig. 1, even at a of 250 A OPL current , its necessary 86.2448 and 86.2768 AT in SC. Wherein SC upper parts are coordinates (3.0416, 3.4965) and (7.1943, 3.6818). SC lower parts are coordinates (6.3707, 0.6637) and (2.8478, 2.4522). To reduce the number of amperes in the SC, we bring the SC to the shielding space. Consider the results of the SAS synthesis at 250 *A* OPL current. In Fig. 16 are shown location of OPL and shielding space in which MF must mitigated to the sanitary norms level and location of both SC. The SC upper parts are coordinates (6.0278, 2.9014) and (7.9925, 3.1824). SC lower parts are coordinates (8.0261, 1.0391) and (5.9751, 0.1319).

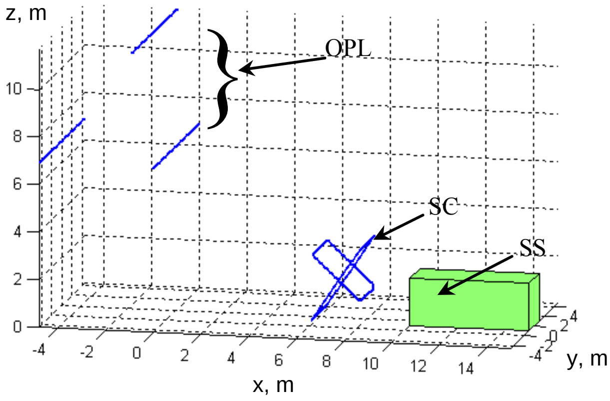

Fig.16. The location of 110 kV overhead power line with phase conductors triangular arrangements, both shielding coils and shielding space

In this SAS at 250 A OPL current, its necessary 28.7127 and –25.6121 AT in SC. Phase current shifts are 1.0056 rad and 1.6681 rad. In Figure 17 are shown comparison of magnetic flux density between with and without SAS. The initial magnetic flux density level in shielding space is 0.75 μT. When the SAS is on, the magnetic flux density level in shielding space is reduced to 0.26 μT. Therefore, the shielding factor is 2.88.

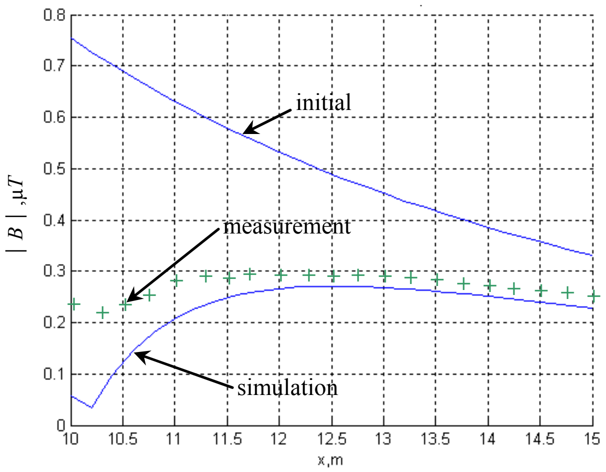

Fig. 17. Comparison of magnetic flux density between measurements and simulations with and without system of active shielding

In Figure 18 are shown the STC of MF, generated by OPL (1); both SC (2) and total MF with SAS is on (3).

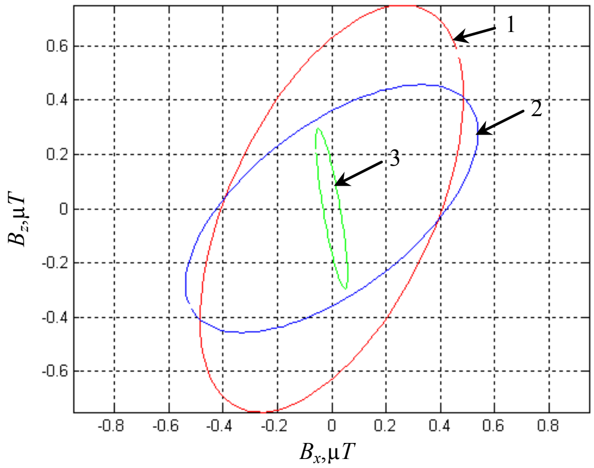

Fig. 18. Comparison of space-time characteristics of magnetic flux density between with and without system of active shielding and both shielding coils

The STC of initial MF generated by OPL with phase conductors triangular arrangements close to the circle. STC of MF generated by both SC is also close to the circle of the STC of initial MF, which ensures high shielding factor.

The STC of the resulting MF generated by OPL and only single SC is an ellipse, which will be shielded by another SC. In Figure 19 are shown the STC of the initial MF generated by OPL, shielding MF generated by only single first SC and the resulting MF when only single first SC is used.

As can seen from Fig. 19, the STC of the resulting MF is a strongly elongated ellipse, the semi-major axis of which is almost 1.5 times larger than the STC of the initial MF, and therefore, due to only single first SC work, initial MF is almost twice re compensated. However, then after second SC switching resulting MF STC becomes significantly less than the STC of initial MF, which ensures high shielding factor. Note that the STC of the resulting MF, left after the operation of only single first SC, practically parallel with the STC generated by the MF using only single second SC.

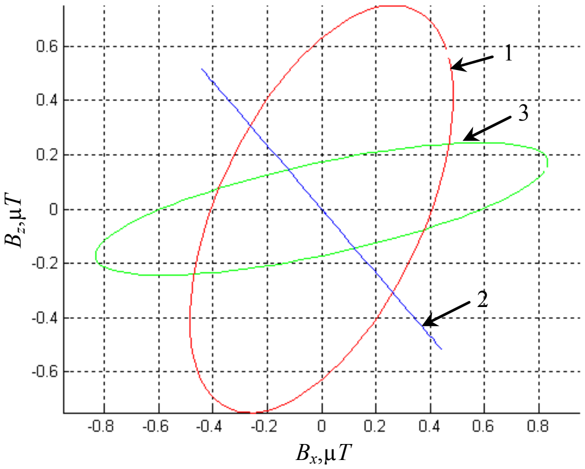

Fig. 19. Comparison between space-time characteristics of magnetic flux density without and with system of active shielding with only single first shielding coil and only single first shielding coil

In Figure 20 are shown the STC of the initial MF generated by OPL, shielding MF generated by only single second SC and the resulting MF when only single second SC is used.

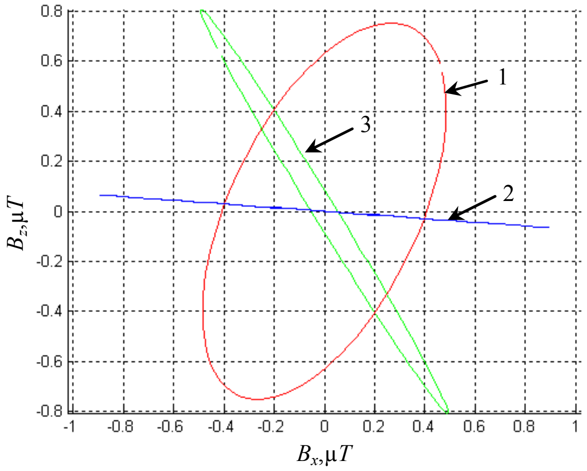

Fig. 20. Comparison between space-time characteristics of magnetic flux density without and with system of active shielding with only single second shielding coil and only single second shielding coil

At 250 A OPL current the initial magnetic flux density level ranges from 0.75 μT to 0.33 μT in all shielding space, as can be seen from Fig. 17. However, when SAS is on and with only single first SC is used, the magnetic flux density level ranges from 1.5 μT to 0.3 μT in all shielding space. Consequently, when SAS is on and with only single first SC is used initial magnetic flux density level more than double due to overcompensation. When SAS is on and with only single second SC is used, the magnetic flux density level ranges from 1.5 μT to 0.35 μT in all shielding space. Consequently, when SAS is on and with only single second SC is used initial magnetic flux density level also more than double due to recompensation. However, when SAS is on and with both first SC and second SC is used, the magnetic flux density level does not exceed 0.26 μT in all shielding space. Consequently, when SAS is on and with both first SC and second SC is used shielding factor is 2.88.

Note that with the first variant of the location of the SC shown in Fig. 1 and Fig. 2, magnetic flux density value of the initial MP decreases from 0.75 μT to 0.12 μT and, therefore, the shielding factor is 6.25. However, in this case, it is necessary to use 86.2448 AT and 86.2768 AT in a SC. Such a large value of the amperes turns in SC are due to the fact that in this variant the both SC are located closer to the transmission line, but with the variant of the location of the SC shown in Fig. 16 and Fig. 17, at the same 250 A OPL current, the initial magnetic flux density level are reduced from 0.75 μT to 0.26 μT and, therefore, the screening factor is 2.88. However, in this case, it is necessary to use 28.7127 AT and 25.6121 AT in a SC. Such a small value of the amperes turns in SC is because in this variant the both SC are located far from OPL.

Experimental research. Consider the field experimental research of the SAS model. SC upper parts of SC located at heights of 2.9 m and 3.2 m from the ground, and the SC lower parts located at heights of 1 m and 0.1 m from the ground. Both SC contains 20 winds and are powered by 1.4 A and 1.25 A current from amplifier type TDA7294. In Figure 17 are shown comparison of magnetic flux density between measurements (cross) and simulations (solid) with and without SAS. The experimental SAS shielding factor is also more than 2 units. A magnetic flux density difference between measurements and simulations in the shielding zone does not exceed 20 %.

Conclusions.

1. For the first time the synthesis, computer modeling and field experimental research of the effectiveness of system of active shielding of magnetic field with circular space-time characteristic, generated by overhead power lines with triangular conductor's arrangement, and with different shielding coils spatial positions are given.

2. The synthesis of two degree of freedom robust two-circuit system of active shielding is based on multi-criteria stochastic game decision, which is calculated by multiswarm stochastic multi-agent optimization from Pareto-optimal solutions. Multi-criteria game vector payoff is calculated based on the Maxwell equations solution. The spatial arrangement and currents in two shielding coils, the regulator parameters and resulting magnetic flux density value in the shielding space are determined by the system synthesis.

3. It was found, that depending on the shielding coils spatial positions, the shielding factor level varies in the range from 6.25 to 2.88. The closer the shielding coils are located to overhead power lines, the shielding factor level higher. However, the closer the shielding coils are located to overhead power lines, it is necessary the amperes of turns greater in shielding coils by shield the initial magnetic field in the shielding space. Naturally, with the same shielding coils arrangement when the overhead power line current changes, the shielding coils current changes in proportion to the line current.

4. It is shown, that when only single first shielding coil or only single second shielding coil is working separately, the initial magnetic flux density level may increases 2-3 times due to overcompensation by initial magnetic field. Moreover, the space-time characteristic of magnetic field, generated separately by only single first shielding coil or only single second shielding coils are straight lines. However the space-time characteristic of the resulting magnetic field, which left after the work of only single first (or second) shielding coil, practically parallel with the space-time characteristic of magnetic field generated by using only single second (or first) shielding coil. It is the space-time characteristic arrangement that provides ensures high shielding factor, when both shielding coils work simultaneously.

5. Based on field experimental research of two degree of freedom robust two-circuits system of active shielding of magnetic field with circular space-time characteristic, generated by overhead power lines with «triangle» type of phase conductor's arrangements, and with different shielding coils spatial positions are shown that experimental and calculated magnetic flux density values in the shielding space spread does not exceed 20 %.

REFERENCES

1. Rozov V., Grinchenko V. Simulation and analysis of power frequency electromagnetic field in buildings closed to overhead lines. *2017 IEEE First Ukraine Conference on Electrical and Computer Engineering (UKRCON)*. Kyiv, Ukraine, pp. 500-503. **doi: 10.1109/UKRCON.2017.8100538**.

2. Rozov V.Yu., Grinchenko V.S., Yerisov A.V., Dobrodeyev P.N. Efficient shielding of three-phase cable line magnetic field by passive loop under limited thermal effect on power cables. *Electrical engineering & electromechanics*, 2019, no.6, pp. 50-54. **doi: 10.20998/2074-272X.2019.6.07.**

3. Active Magnetic Shielding (Field Cancellation). Available at: http://www.emfservices.com/afcs.html (accessed 12 September 2019).

4. Rozov V.Yu., Reutskyi S.Yu., Pelevin D.Ye., Pyliugina O.Yu. The magnetic field of transmission lines and the methods of its mitigation to a safe level. *Technical Electrodynamics*, 2013, no. 2, pp. 3-9. (Rus).

5. Rozov V.Yu., Reutskyi S.Yu. Pyliugina O.Yu. The method of calculation of the magnetic field of three-phase power lines. *Technical electrodynamics*, 2014, no.5, pp. 11-13. (Rus).

6. Salceanu A., Paulet M., Alistar B.D., Asiminicesei O. Upon the contribution of image currents on the magnetic fields generated by overhead power lines. *2019 International Conference on Electromechanical and Energy Systems (SIELMEN)*. 2019. **doi: 10.1109/sielmen.2019.8905880.**

7. Bravo-Rodríguez J., Del-Pino-López J., Cruz-Romero P. A Survey on Optimization Techniques Applied to Magnetic Field Mitigation in Power Systems. *Energies*, 2019, vol.12, no.7, p. 1332. **doi: 10.3390/en12071332**.

8. Canova A., Giaccone L., Cirimele V. Active and passive shield for aerial power lines. *25th International Conference on Electricity Distribution Madrid*, 3-6 June 2019. Paper no. 1096, pp. 1-5.

9. Chorna O., Chornyi O., Tytiuk V. Identification of changes in the parameters of induction motors during monitoring by measuring the induction of a magnetic field on the stator surface. *2019 IEEE International Conference on Modern Electrical and Energy Systems (MEES)*. Kremenchuk, 2019. **doi: 10.1109/MEES.2019.8896554.**

10. Chystiakov P., Chornyi O., Zhautikov B., Sivyakova G. Remote control of electromechanical systems based on computer simulators. *2017 International Conference on Modern Electrical and Energy Systems (MEES)*. Nov. 2017. **doi: 10.1109/mees.2017.8248934.**

11. Shenkman A., Sonkin N., Kamensky V. Active protection from electromagnetic field hazards of a high voltage power line. *HAIT Journal of Science and Engineering. Series B: Applied Sciences and Engineering*, Vol. 2, Issues 1-2, pp. 254-265.

12. Korol S., Buryan S., Pushkar M., Ostroverkhov M. Investigation the maximal values of flux and stator current of autonomous induction generator. *2017 IEEE First Ukraine Conference on Electrical and Computer Engineering (UKRCON)*, May 2017. **doi: 10.1109/ukrcon.2017.8100302**.

13. Ostroverkhov M., Buryk M. Control of permanent magnet synchronous motor under conditions of parametric uncertainty. *2019 IEEE International Conference on Modern Electrical and Energy Systems (MEES)*, Sep. 2019. **doi: 10.1109/mees.2019.8896635.**

14. Ostroverkhov M., Pyzhov V., Korol S. Control of the electric drive under conditions of parametric uncertainty and coordinates' interrelation. *2017 International Conference on Modern Electrical and Energy Systems (MEES)*, Nov 2017. **doi: 10.1109/mees.2017.8248953.**

15. Panchenko V.V., Maslii A.S., Pomazan D.P., Buriakovskyi S.G. Determination of pulsation factors of the system of suppression of interfering harmonics of a semiconductor converter. *Electrical engineering & electromechanics*, 2018, no.4, pp. 24-28. **doi: 10.20998/2074-272X.2018.4.04.**

16. Buriakovskyi S.G., Maslii A.S., Panchenko V.V., Pomazan D.P., Denis I.V. The research of the operation modes of the diesel locomotive CHME3 on the imitation model. *Electrical engineering & electromechanics*, 2018, no.2, pp. 59-62. **doi: 10.20998/2074-272X.2018.2.10.**

17. Buriakovskyi S., Maslii A., Maslii A. Determining parameters of electric drive of a sleeper-type turnout based on electromagnet and linear inductor electric motor. *Eastern-European Journal of Enterprise Technologies*, 2016, vol.4, no.1(82), pp. 32-41. (Rus). **doi: 10.15587/1729-4061.2016.75860**.

18. Shchur I., Klymko V. Comparison of different types of electromechanical systems for creating of counter-rotating VAWT. *2017 IEEE First Ukraine Conf. on Electrical and Computer Engineering (UKRCON-2017)*, pp. 373-378. **doi: 10.1109/ukrcon.2017.8100513**.

19. Shchur I. Impact of nonsinusoidalness on efficiency of alternative electricity generation systems. *2010 International School on Nonsinusoidal Currents and Compensation*, Lagow, 2010, pp. 218-223. **doi: 10.1109/isncc.2010.5524483**.

20. Zagirnyak M., Bisikalo O., Chorna O., Chornyi O. A model of the assessment of an induction motor condition and operation life, based on the measurement of the external magnetic field. *2018 IEEE 3rd International Conference on Intelligent Energy and Power Systems (IEPS)*. 2018. pp. 316-321. **doi: 10.1109/ieps.2018.8559564.**

21. Zagirnyak M., Chornyi O., Nykyforov V., Sakun O., Panchenko K. Experimental research of electromechanical and biological systems compatibility. *Przegląd Elektrotechniczny*, 2016, vol.1, no.1, pp. 130-133. **doi: 10.15199/48.2016.01.31**.

22. Zagirnyak M., Serhiienko S., Chornyi O. Innovative technologies in laboratory workshop for students of technical specialties. *2017 IEEE First Ukraine Conference on Electrical and Computer Engineering (UKRCON)*, May 2017. **doi: 10.1109/ukrcon.2017.8100446**.

23. Sushchenko O.A., Tunik A.A. Robust optimization of the inertially stabilized platforms. *2012 2nd International Conference «Methods and Systems of Navigation and Motion Control» (MSNMC)*, Kiev, 2012, pp. 101-105. **doi: 10.1109/msnmc.2012.6475102.**

24. Sushchenko O.A. Robust control of angular motion of platform with payload based on H∞-synthesis. *Journal of Automation and Information Sciences*, 2016, vol. 48, no. 12, pp. 13-26. **doi: 10.1615/jautomatinfscien.v48.i12.20**.

25. Sushchenko O.A. Robust control of platforms with instrumentation. *2019 IEEE 2nd Ukraine Conference on Electrical and Computer Engineering (UKRCON)*, Lviv, Ukraine, 2019, pp. 518-521. **doi: 10.1109/ukrcon.2019.8879969**.

26. Zhiteckii L.S., Azarskov V.N., Solovchuk K.Y., Sushchenko O.A. Discrete-time robust steady-state control of nonlinear multivariable systems: a unified approach. *IFAC Proceedings Volumes*, 2014, vol. 47, no. 3, pp. 8140-8145. **doi: 10.3182/20140824-6-za-1003.01985.**

27. Zhiteckii L.S., Solovchuk K.Y. Robust adaptive pseudoinverse model-based control of an uncertain SIMO memoryless system with bounded disturbances. *2019 IEEE 2nd Ukraine Conference on Electrical and Computer Engineering (UKRCON)*, Lviv, Ukraine, 2019, pp. 621-627. **doi: 10.1109/ukrcon.2019.8879824.**

28. *Electrical installation regulations. 5th ed.* The Ministry of Energy and Coal Mining of Ukraine, 2014. 277 p. (Ukr).

29. Ren Z., Pham M.-T., Koh C.S. Robust Global Optimization of Electromagnetic Devices With Uncertain Design Parameters: Comparison of the Worst Case Optimization Methods and Multiobjective Optimization Approach Using Gradient Index. *IEEE Transactions on Magnetics*, 2013, vol.49, no.2, pp. 851-859. **doi: 10.1109/tmag.2012.2212713**.

30. Galchenko V.Y., Yakimov A.N. A turmitobionic method for the solution of magnetic defectometry problems in structural-parametric optimization formulation. *Russian Journal of Nondestructive Testing*, 2014, vol.50, no.2, pp. 59-71. **doi: 10.1134/s106183091402003x.**

31. Gal'chenko V.Y., Yakimov A.N., Ostapushchenko D.L. Pareto-optimal parametric synthesis of axisymmetric magnetic systems with allowance for nonlinear properties of the ferromagnet. *Technical Physics*, 2012, vol.57, no.7, pp. 893-899. **doi: 10.1134/s1063784212070110**.

32. Ummels M. *Stochastic Multiplayer Games Theory and Algorithms*. Amsterdam University Press, 2010. 174 p.

Received 23.12.2019

B.I. Kuznetsov[1], *Doctor of Technical Science, Professor,*
T.B. Nikitina[2], *Doctor of Technical Science, Professor,*
I.V. Bovdui[1], *Candidate of Technical Science,*
[1] State Institution «Institute of Technical Problems
of Magnetism of the NAS of Ukraine»,
19, Industrialna Str., Kharkiv, 61106, Ukraine,
phone +380 50 5766900,
e-mail: kuznetsov.boris.i@gmail.com
[2] Kharkov National Automobile and Highway University,
25, Yaroslava Mudroho Str., Kharkov, 61002, Ukraine,
e-mail: tatjana55555@gmail.com

How to cite this article:
Kuznetsov B.I., Nikitina T.B., Bovdui I.V. The effectiveness of active shielding of magnetic field with circular space-time characteristic and with different shielding coils spatial positions. *Electrical engineering & electromechanics*, 2020, no. 3, pp. 15-23. **doi: 10.20998/2074-272X.2020.3.03.**

UDC 537.85:621.315:504.06 **doi: 10.20998/2074-272X.2020.3.04**

V.Yu. Rozov, K.D. Kundius, D.Ye. Pelevin

ACTIVE SHIELDING OF EXTERNAL MAGNETIC FIELD OF BUILT-IN TRANSFORMER SUBSTATIONS

This paper deals with the mitigation of low-frequency magnetic field of build-in transformer substations down to the reference level 0.5 μT in nearby living spaces. To meet the reference level, we substantiate the actuality of the usage of active shielding methods having higher efficiency, comparably to metal consuming passive shielding. We show that the optimization of parameters and localization of compensation coils is the main goal of the synthesis of the active shielding system. The solution of synthesis problem is based on the developed 3D numerical model by using particles multiswarm optimization algorithms from Pareto-optimal solutions set taking into account binary preference relations. This allows justifying the usage of simple active shielding system for magnetic field mitigation down to the reference level in living spaces, located near build-in transformer substations (2×400 kVA, 6/0.4 kV). The synthesized active shielding system has two plane compensation coils installed near the ceiling (wall) of the substation room. The area of each coil is less than 10 m^2 and the number of ampere-turns is less than 30. We show that the efficiency of the active shielding system is 6 when it electric power consumption is less than 100 W. This allows mitigating the magnetic field down to 0.5 μT in 40 m^2 living space located on top or side from the substation. The application of synthesized active shielding system (subject to the positive results of experimental studies of their full-scale physical models) allows solving the actual and socially significant problem of the health protection of tenants of residential buildings with build-in transformer substations from the negative effects of power frequency magnetic field. References 16, tables 2, figures 8.

Key words: **urban transformer substation, living space, active shielding of the magnetic field.**

Показано, що основною задачею синтезу систем активного екранування (САЕ) є оптимізація параметрів і локалізації їх компенсаційних обмоток (КО) при забезпеченні високої ефективності екранування магнітного поля (МП) трансформаторної підстанції (ТП). Її рішення виконано на основі запропонованої тривимірної комп'ютерної моделі з використанням алгоритмів оптимізації мультироєм частинок з множини Парето- оптимальних рішень і урахуванням бінарних відносин переваги, що дозволило обґрунтувати можливість зменшення до рівня санітарних норм індукції МП в житлових приміщеннях, розташованих поруч з ТП 6/0,4 кВ потужністю до 2×400 кВА, за допомогою найпростіших САЕ. Синтезована САЕ має дві плоскі КО площею до 10 м^2 при кількості ампер-витків не більше 30, що встановлюються поблизу стелі (стін) приміщення ТП, і при енергоспоживанні не більше 0,1 кВт реалізує ефективність екранування САЕ не менше 6 одиниць, що дозволяє зменшити індукцію магнітного поля в розташованому зверху або збоку від ТП житловому приміщенні площею до 40 м^2 до рівня 0,5 мкТл. Бібл. 16, табл. 2, рис. 8.

Ключові слова: **міська трансформаторна підстанція, житлове приміщення, активне екранування магнітного поля.**

Показано, что основной задачей синтеза систем активного экранирования (САЭ) является оптимизация параметров и локализации их компенсационных обмоток (КО) при обеспечении высокой эффективности экранирования магнитного поля (МП) трансформаторной подстанции (ТП). Ее решение выполнено на основе предложенной трехмерной компьютерной модели с использованием алгоритмов оптимизации мультироем частиц из множества Парето-оптимальных решений с учетом бинарных отношений предпочтения, что позволило обосновать возможность уменьшения до уровня санитарных норм индукции МП в жилых помещениях, расположенных рядом с ТП 6/0,4 кВ мощностью до 2×400 кВА, с помощью простейших САЭ. Синтезированная САЭ имеет две устанавливаемые вблизи потолка (стен) помещения ТП плоские КО площадью до 10 м^2 при количестве ампер-витков не более 30, и при энергопотреблении не более 0,1 кВт реализует эффективность экранирования САЭ не менее 6 единиц, что позволяет уменьшить индукцию магнитного поля в расположенном сверху либо сбоку от ТП жилом помещении площадью до 40 м^2 до уровня 0,5 мкТл. Библ. 16, табл. 2, рис. 8.

Ключевые слова: **городская трансформаторная подстанция, жилое помещение, активное экранирование магнитного поля.**

Introduction. Much attention is paid to the problem of protecting the living environment from the influence of the magnetic field (MF) of electric power facilities around the world, since power frequency (50-60 Hz) MF is dangerous to human health even with its weak but prolonged exposure [1, 2]. The main sources of MF in a residential environment are overhead and cable power lines (PLs) located in residential areas, as well as urban transformer substations (TSs) [3].

Urban TSs are located in separate buildings or are built into residential buildings [3]. The most acute problem of reducing external MF of the TS is in residential buildings with built-in TS [2-4], when the distance between the TS and residential premises is reduced to several meters. Such buildings (Fig. 1) are quite widespread in Ukraine and other countries.

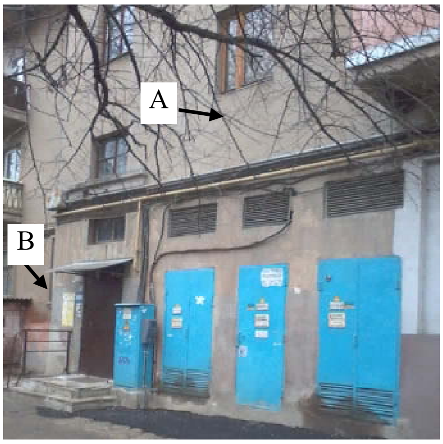

Fig. 1. Typical residential building in Kharkiv with built-in TP

In addition, built-in TPs began to be widely used in the world in modern ultra-high-rise residential buildings for individual high voltage power supply of sections of several tens of floors in order to reduce electricity losses [5, 6].

The studies conducted by the authors [3] show that the external MF of typical built-in TSs with power of 400 (800) kVA can exceed the level of sanitary standards in residential premises adjacent to the transformer substation by 3-10 times, which requires measures to reduce their MF. In this case, the main source of the external TS MF is their current leads, and the scattering MF of TS transformers at distances greater than 2 m from the transformer substation can be neglected [3].

The most urgent problem is the reduction of the TS MF in old buildings with built-in TS (Fig. 1), when the practical use of methods to reduce MF due to the improvement of the design of TS [3] is difficult. Currently, the most common technique in practice of reducing the MF in the spaces adjacent to the TS is passive shielding of the walls (ceilings) of the TS premises by electromagnetic (magnetostatic) shields [7]. However, this shielding method for low-frequency TS MF is characterized by high metal consumption and cost at low efficiency.

Therefore, a promising method of reducing the TS MF is active shielding (compensation) of the MF [3, 8-14]. Moreover, the global trend in the development of active shielding systems (ASS) aims to optimize their design for energy consumption and cost, provided that the necessary shielding efficiency is provided.

However, in Ukraine, the development of methods and means of active shielding of TS MF is not given due attention. So, up to the present, the possibility and the ways to create inexpensive budgetary ASSs with efficiency sufficient to reduce the TS MF in nearby residential premises to the level of sanitary standards have not been substantiated.

The goal of the work is an analysis of the possibility of reducing the magnetic flux density in residential premises located next to urban transformer substations to the level of sanitary standards using simple active shielding systems.

By the simplest ASS we mean a system with a minimum number of flat compensation windings (CWs) placed near the surface of the walls (floors) of the premises, which has a limited power consumption of hundreds of watts.

Active shielding method. The method of active shielding of the potential TS M in the volume of the living premise adjacent to the TS is realized through the formation of the ASS (Fig. 2) of the compensating MF of such a spatio-temporal structure, the superposition of which with the original TS MF reduces the effective value of the magnetic flux density in the entire protected volume of the living space from walls and floor to a distance of more than 0.5 m, to the level of sanitary standards (0.5 μT) for the population [12]. In this case, the compensating MF generated by the CW must also be potential in the volume of the living space, which imposes certain requirements on the configuration and location coordinates of the CW during their synthesis.

ASS (Fig. 2) consists of the following main elements: compensation windings (CW); regulated power source (PS) performing the function of a power amplifier, control system (CS); sensors (S) of current or MF. In the general case, ASS can have a different amount of CW, S and can be realized in a closed or open structure [11, 12].

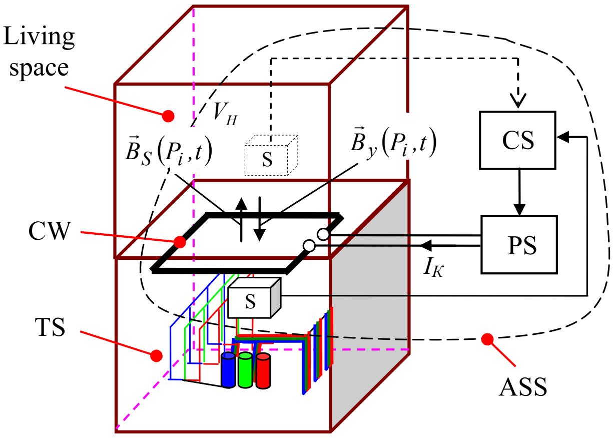

Fig. 2. Active shielding of the external TS MF

To determine the parameters of the ASS (Fig. 2), it is necessary to carry out its synthesis. The initial data for the synthesis of ASS are: the spatio-temporal characteristic of the initial MF of the urban TS in the protected volume (residential space); mutual spatial arrangement of active elements of the TS and residential premises; geometry and number of three-phase current leads of the TS; the standard value of the level of the magnetic flux density, which should be achieved as a result of shielding. In this case, the effect of shielding of the TS MF by the walls and floors of residential buildings is neglected due to its smallness [15, 16].

We carry out active shielding of TS MF using the proposed in [14] method of synthesis of ASS, created for shielding of the MF of high-voltage PLs in order to reduce it to a level safe for the population in nearby residential buildings. A feature of this method is the solution of the shielding problem in a 2D formulation, which is acceptable for extended PLs with an almost zero component of magnetic flux density directed along the PL, which allows to significantly simplify the solution to the synthesis problem for such ASS [13, 14].

A more complicated design of current leads of finite length [3], compared with PL [3], makes it necessary to model the TS MF in a 3D formulation, which significantly complicates the synthesis of the TS ASS. Another feature of solving the problem of synthesis of the TS ASS is the need to locate their CW outside residential premises. Taking into account these features, the synthesis of TS MF ASS is carried out on the basis of the modified method developed and presented below.

A modified method for the synthesis of TS ASS. The mathematical model of the initial external TS MF in the shielding zone (residential space), remote from the TS by more than 2 meters [3], not containing ferromagnetic elements and magnetic field sources, can be represented as:

$$\vec{B}_S(P_i,t) = -\sum_{k=1}^{K}\sum_{\alpha=1}^{3}\sum_{n=1}^{N}\nabla\left[\frac{\mu_0\left(\vec{m}(t)_{l\alpha n},\vec{R}_{l\alpha i}\right)}{4\pi R_{l\alpha i}^{3}}\right]; \tag{1}$$

$$\vec{m}(t)_{l\alpha n} = I(t)\cdot\vec{S}_{l\alpha n},$$

where N is the number of microcontours in the rectilinear contour of the TS current lead; k is the number of rectilinear contours; $\vec{S}_{l\alpha n}$ is the area vector of the microcontour; $\vec{n}_i$ is the unit vector normal to S_i; $\vec{R}_{l\alpha i}$ is the radius vector from the geometric center of the microcontour to the observation point P_i; $I(t)$ is the instantaneous value of the microcontour current; α is the phase number of the TS current lead (α = 1 ... , 3); μ_0 is the magnetic constant. In accordance with (1), the TS MF is potential and decreases with distance from the source.

Let us introduce the vector of the sought-for parameters R, the components of which are the sought-for geometrical parameters, the coordinates of the spatial arrangement of the ASS CWs and the sought-for parameters of the ASS CWs. Then, the flux density of the resulting potential MF generated by the TS current leads and ASS is determined as

$$\vec{B}(R,P_i,t) = \vec{B}_S(P_i,t) + \vec{B}_y(R,P_i,t), \tag{2}$$

where $\vec{B}_y(R,P_i,t)$ are the instantaneous values of the flux density of the MF generated by the ASS CWs in points P_i.

By analogy with [14], we reduce the determination of the vector of the sought-for parameters R to the solution of the multicriteria optimization problem of the vector criterion

$$B(R) = \left[B(R,P_1), B(R,P_2)\ldots B(R,P_m)\right]^T, \tag{3}$$

whose components $\vec{B}(R,P_i)$ are the values of the flux density of the resulting MF at points P_i.

This multicriteria optimization problem (3) will be solved in computer modelling based on algorithms for optimizing by particles multiswarm from the set of Pareto-optimal solutions taking into account binary preference relations [13, 14]. Modelling is carried out in the MATLAB software package.

Analysis of the effectiveness of active shielding of the TS MF. The efficiency (factor) of the shielding of the ASS MF at the point P_i in accordance with [11] can be determined by the relation

$$E_{Pi} = \frac{\left|\vec{B}_S(P_i)\right|}{\left|\vec{B}_S(P_i)+\vec{B}_y(P_i)\right|} = \frac{1}{\delta_{Pi}}, \tag{4}$$

where $\vec{B}_S(P_i)$, $\vec{B}_y(P_i)$ are the effective values of the initial and generated by ASS magnetic flux densities at the point P_i; δ_{Pi} is the relative error in the shielding of the ASS.

For example, with the above-mentioned excess of sanitary standards by 3-10 times, the required shielding efficiency will be 3 (10) units, and the permissible relative error in compensating the magnetic flux density should be no less than 0.33 (0.1), respectively. Here, the value δ_{Pi} can be defined as

$$\delta_{Pi} = \sqrt{\delta_{Pim}^2 + \delta_{Pir}^2}\ , \tag{5}$$

where δ_{Pim} is the relative methodological error of the ASS, determined by the mismatch of the spatial structure of the initial MF and the compensating MF generated by the CWs; δ_{Pir} is the relative error of regulation of the ASS.

An analysis of relation (5) shows that the main component of the ASS error is the methodological error δ_{Pim}, which is determined by the CW parameters and limited to 0.1 with shielding efficiency of no more than 10 units. In this case, the relative error δ_{Pir} of regulation of the ASS when using modern automatic control systems can be easily reduced to values of 0.01-0.03, at which it will not have a significant impact on the total shielding error of δ_{Pi} of the ASS. This allows at this stage to reduce the synthesis of ASS to the synthesis of its CWs. Therefore, the ASS control algorithm is not considered in this paper and is the subject of separate studies.

We carry out the solution of the problem of synthesis of ASS CWs and analysis of the efficiency of shielding of TS MF for a typical urban two-transformer substation (2×400 kVA, 6/ 0.4 kV), built into a residential building on the ground floor. The dimensions of the TS premises correspond to the sizes of neighboring residential premises. The arrangement of TS current leads is shown in Fig. 3, and their geometry is given in [3]. Three-phase current leads are connected with direct phase sequence.

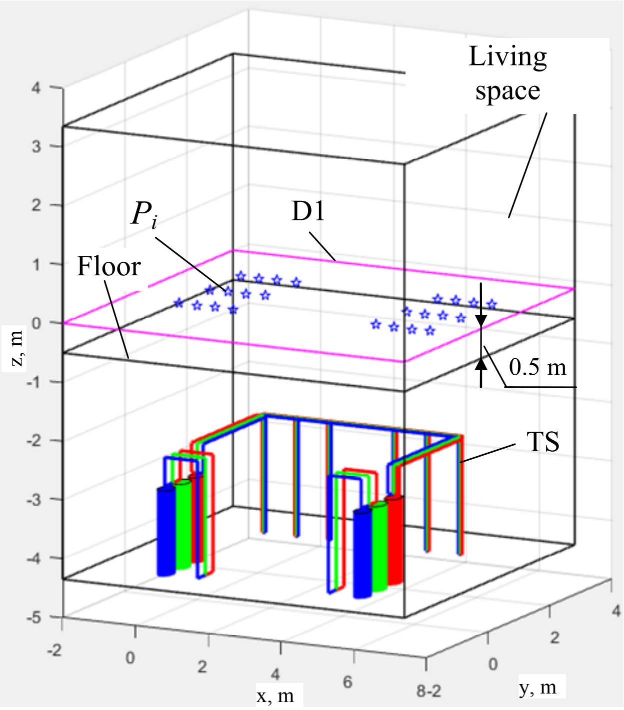

Fig. 3. Location of the premise over the TS (option A)

Computer simulation of the external TS MF is carried out in accordance with (1)-(3). In this case, two options for the location of the living space relative to the TS are considered (Fig. 1): option A – the premise is located over the TS; option B – the premise is located near the TS on one floor (on the side of the TS).

Shielding of the MF in the premise over the TS (option A). Let us carry out the synthesis of ASS CWs, which ensure the necessary efficiency of the MF shielding in the premise located over the TS (Fig. 3).

To guarantee a decrease in the flux density of the potential MF to the level of sanitary standards in the entire living space, it is enough to ensure a corresponding decrease in the MF on the control plane D1, which is 0.5 m from the floor of the room (Fig. 3), where the MF is normalized [1, 2].

The calculated value of the flux density of the initial TS MF at rated power of the TS is presented in Fig. 4. Here, the maximum value of the initial magnetic flux density is 3 μT, which is 6 times higher than the level of sanitary standards of 0.5 μT [2].

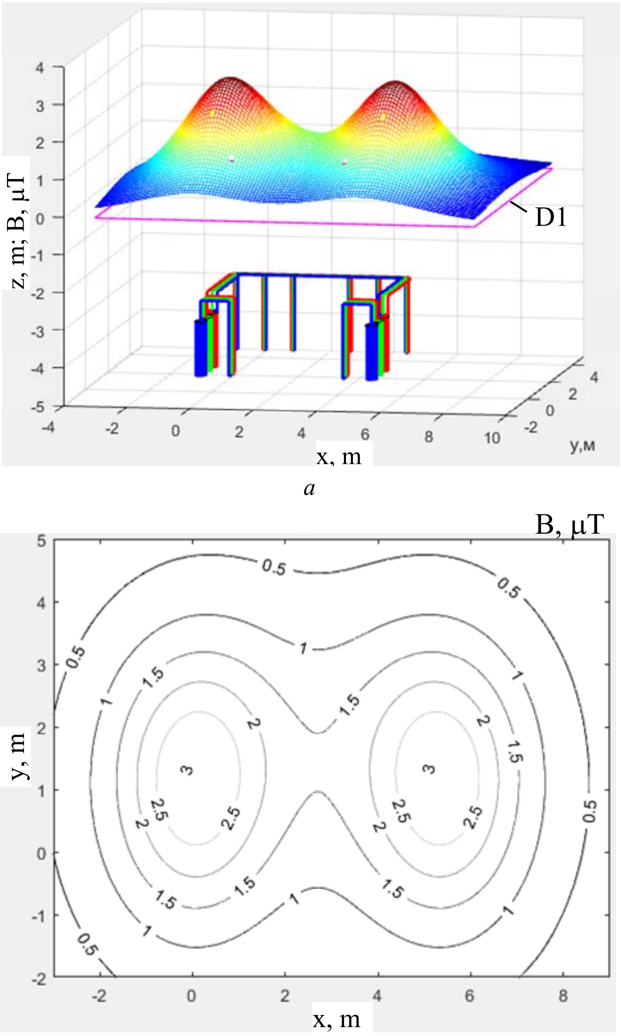

b

Fig. 4. Distribution of the initial magnetic flux density in the living space over the TS, option A:
(*a*) – indoors; (*b*) – on the control plane D1

Based on the simulation, synthesis of the ASS CWs is performed (Fig. 5), and their parameters are determined in accordance with Table 1. CWs are located in the TS premise, parallel to its ceiling, at a distance of 0.55 m from it, and make it possible to realize the necessary shielding efficiency, reducing the initial TS MF (Fig. 4) to the level of sanitary standards.

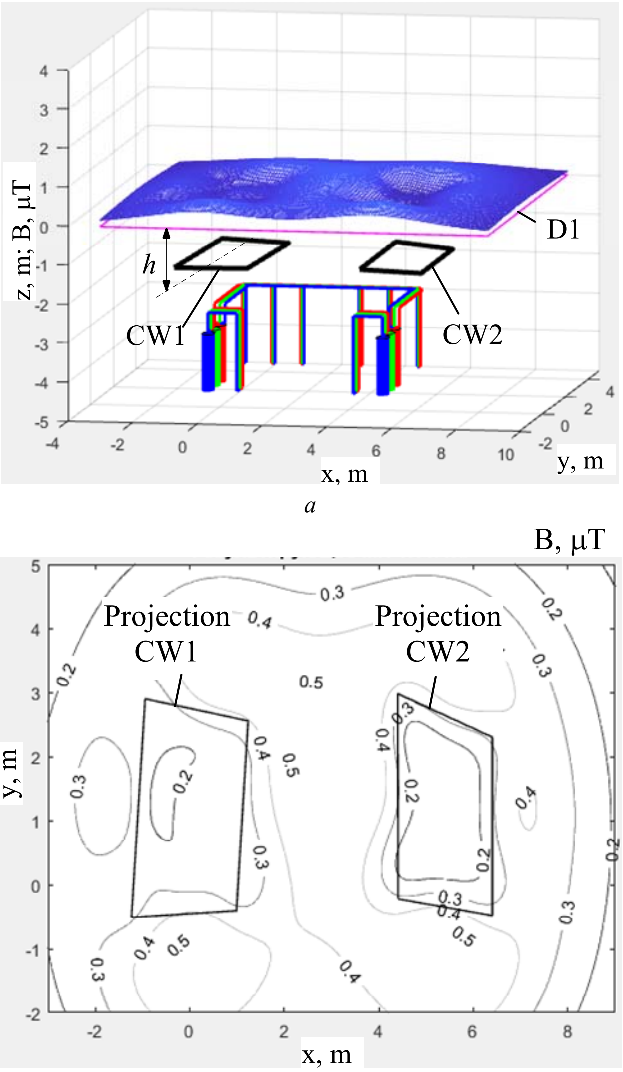

b

Fig. 5. Distribution of the resulting magnetic flux density in the living space over the TS using ASS, option A:
(*a*) – indoors; (*b*) – on the control plane D1

Table 1

Parameters of compensating windings of the ASS (option A)

CW No.	Ampere-turns, CW power	CW coordinates
1	$IW1$ = 24,5 A, S = 36 VA, h = 1,35 m.	$x11$ = –1,23 m, $y11$ = –0,51 m, $z11$ = –1,35 m, $x12$ = –0,94 m, $y12$ = 2,90 m, $z12$ = –1,35 m, $x13$ = 1,24 m, $y13$ = 2,55 m, $z13$ = –1,35 m, $x14$ = 0,99 m, $y14$ = –0,40 m, $z14$ = –1,35 m.
2	$IW2$ = 25,6 A, S = 36 VA, h = 1,35 m.	$x21$ = 4,41 m, $y21$ = –0,22 m, $z21$ = –1,35 m, $x22$ = 4,40 m, $y22$ = 2,98 m, $z22$ = –1,35 m, $x23$ = 6,40 m, $y23$ = 2,30 m, $z23$ = –1,35 m, $x24$ = 6,40 m, $y24$ = –0,48 m, $z24$ = –1,35 m.

As the simulation results show (Fig. 5), when using synthesized ASS, the level of the magnetic flux density both on the D1 plane and in the entire living space decreases to the safe value of 0.5 μT. Here, the synthesized ASS has a minimum number of CWs located in the TS premise and provides the necessary shielding efficiency (at least 6 units) with energy consumption of not more than 0.1 kW.

Shielding of the MF in the premise located near the TP (option B). Let us perform the synthesis of ASS CWs, providing the necessary efficiency of shielding of the MF in the premise located near the TS on the same floor (Fig. 6).

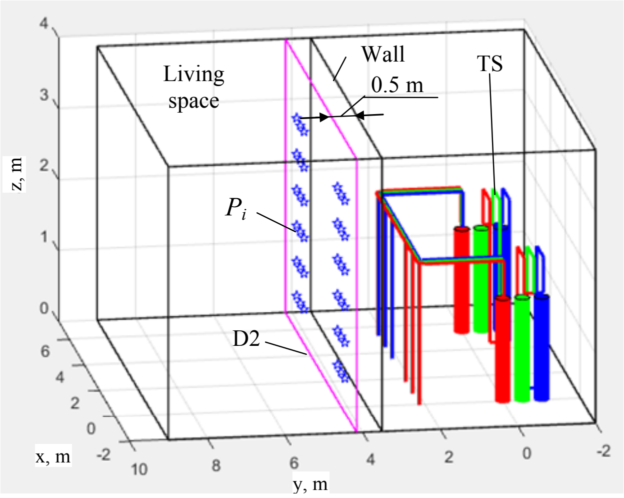

Fig. 6. The location of the premise on the side of the TS (option B)

Figure 7 shows the calculated value of the flux density of the initial TS MF, which reaches 1.2 μT, which is 2.4 times higher than the sanitary standards of 0.5 μT.

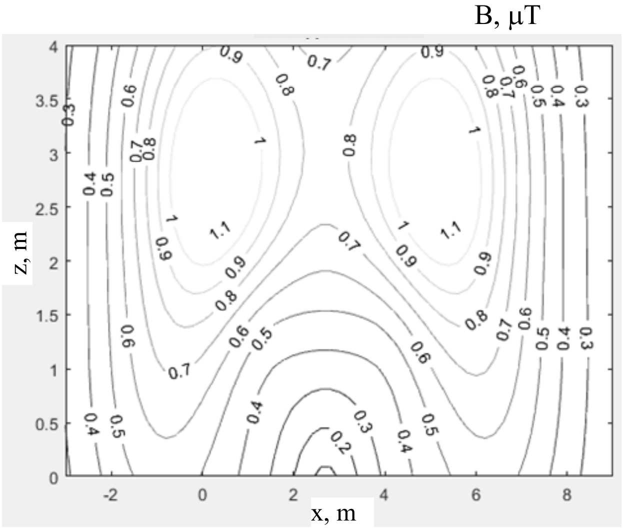

Fig. 7. Distribution of the initial magnetic flux density in the living space located on the side of the TS, option B, on the D2 plane, 0.5 m from the room wall

Based on the simulation, the synthesis of the ASS CWs (Fig. 8) located at a distance of 0.35 m from the plane of the wall of the TS premise is performed, allowing to realize the necessary shielding efficiency and reduce the flux density of the initial TS MF (Fig. 7) to the level of sanitary standards (0.5 μT) when using CWs with parameters in accordance with Table 2.

Table 2

Parameters of compensating windings of the ASS (option B)

CW No.	Ampere-turns, CW power	CW coordinates
1	*IW*1 = 9,45 A, *S* = 10 VA, *h* = 1,15 m	*x*11 = –1,42 m, *y*11 = 3,0 m *z*11 = 2,50 m, *x*12 = –2,0 m, *y*12 = 3,0 m, *z*12 = 3,70 m, *x*13 = 2,0 m, *y*13 = 3,0 m, *z*13 = 3,70 m, *x*14 = 2,0 m, *y*14 = 3,0 m, *z*14= 1,28 m.
2	*IW*2 = 9,44 A, *S* = 10 VA, *h* = 1,15 m.	*x*21 = 3,47 m, *y*21 = 3,0 m, *z*21 = 1,11 м, *x*22 = 3,74 m, *y*22 = 3,0 m, *z*22 = 3,70 m, *x*23= 7,40 m, *y*23 = 3,0 m, *z*23= 3,70 m, *x*24 = 6,56 m, *y*24= 3,0 m, *z*24 = 2,40 m.

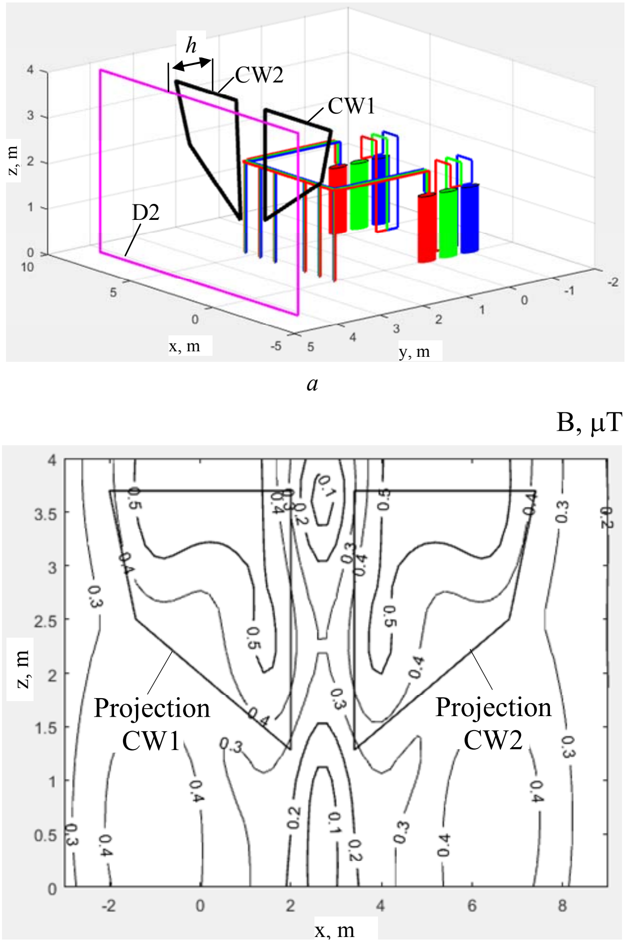

b

Fig. 8. Distribution of the resulting magnetic flux density in the living space on the side of the TS when using the ASS, option B: (*a*) – position of CWs and TS; (*b*) – MF on the control plane D2

The layout of the ASS CWs is shown in Fig. 8,*a* and the calculated distribution of the resulting magnetic flux density in the living space on the side of the TS when using the ASS (option B) on the control plane D2 of the premise wall is shown in Fig. 8,*b*.

As the simulation results show (Fig. 8), when using synthesized ASS, the level of the magnetic flux density in the volume of the living space decreases to the safe value of 0.5 μT. Here, the synthesized ASS also has a minimum number of CWs located near the plane of the wall of the TS premise and provides the necessary shielding efficiency (at least 2.4 units) with energy consumption of not more than 0.03 kW.

Thus, the above analysis confirms the possibility of reducing the magnetic flux density in residential premises with area of 40 m^2, located near urban transformer substations 2×400 kVA, 6/0.4 kV, to the level of sanitary standards with the help of simplest ASS with two flat compensation windings placed near the floor (wall) of the premises of the TS. Here, the energy consumption of the ASS is no more than 0.1 kW, the CW area is no more than 10 m^2 with the number of CW ampere-turns no more than 30. The shielding efficiency (factor) realized by the synthesized TS ASS (Fig. 2) reaches more than 6 units, which has experimental confirmation in laboratory conditions.

At the next stages of creating the TS MF ASS, it is planned to develop its structural elements (Fig. 2) and conduct experimental studies of full-scale models of the ASS in residential buildings with built-in TS.

Conclusions.

1. For the first time, the possibility of solving the problem of reducing to the level of sanitary norms of the magnetic flux density in a living space located near an urban transformer substation with power of up to 2×400 kVA using the simplest active shielding systems has been substantiated. The justification is carried out in computer simulation using algorithms for optimization of particles multiswarm from a multitude of Pareto-optimal solutions taking into account binary preference relations.
2. The synthesis of the simplest systems of active shielding of the magnetic field of transformer substations with two flat compensation windings located near the ceiling (walls) of the TS premise and allowing the magnetic field to be reduced to the level of sanitary standards in a nearby residential area of up to 40 m^2 is performed. In this case, the energy consumption of the active shielding system is no more than 0.1 kW, the area of the compensation windings is no more than 10 m^2 with the number of ampere-turns no more than 30, and the shielding efficiency (factor) reaches more than 6 units, which has experimental confirmation in laboratory conditions.
3. The practical use of synthesized active shielding systems, subject to the positive results of experimental studies of their full-scale physical models, will effectively solve the urgent and socially significant task of protecting the health of the population of residential buildings with built-in transformer substations from the negative effects of magnetic fields of power frequency.

REFERENCES

1. Serdiuk A.M., Dumanskiy V.Yu., Bitkin S.V., Didyk N.V., Dumanskiy Yu.D. Hygienical ground of requirements to placing and exploitation of cable busses of electricity transmission and their equipment in the conditions of modern municipal building. *Hygiene of populated places*, 2015, no.66, pp. 20-29. (Ukr).

2. *Pravila ulashtuvannya electroustanovok* [Electrical installation regulations]. Kharkiv, Fort Publ., 2017. 760 p. (Ukr).

3. Rozov V.Yu., Pelevin D.Ye., Pielievina K.D. External magnetic field of urban transformer substations and methods of its normalization. *Electrical engineering & electromechanics*, 2017, no.5, pp. 60-66. **doi: 10.20998/2074-272X.2017.5.10.**

4. Opoleva G.N. *Skhemy i podstantsii elektrosnabzheniia. Spravochnik* [Schemes and substations of power supply. Directory]. Moscow, Forum-Infra Publ., 2006. 480 p. (Rus).

5. Leung S.W., Chan K.H., Fung L.C. Investigation of power frequency magnetic field radiation in typical high-rise building. *European Transactions on Electrical Power*, 2011, vol. 21, no. 5, pp. 1711-1718. **doi: 10.1002/etep.517**.

6. Rahman N.A., Rashid N.A., Mahadi W.N., Rasol Z. Magnetic field exposure assessment of electric power substation in high rise building. *Journal of Applied Sciences*, 2011, vol. 11, pp. 953-961. **doi: 10.3923/jas.2011.953.961**.

7. Grbić M., Canova A., Giaccone L. Magnetic field in an apartment located above 10/0.4 kV substation: levels and mitigation techniques. *CIRED – Open Access Proceedings Journal*, 2017, vol. 2017, no. 1, pp. 752-756. **doi: 10.1049/oap-cired.2017.1230.**

8. Bravo-Rodríguez J., del-Pino-López J., Cruz-Romero P. A Survey on Optimization Techniques Applied to Magnetic Field Mitigation in Power Systems. *Energies*, 2019, vol. 12, no. 7, p. 1332. **doi: 10.3390/en12071332**.

9. Canova A., Giaccone L. Real-time optimization of active loops for the magnetic field minimization. *International Journal of Applied Electromagnetics and Mechanics*, 2018, vol.56, pp. 97-106. **doi: 10.3233/jae-172286**.

10. del Pino Lopez J.C., Giaccone L., Canova A., Cruz Romero P. Ga-based active loop optimization for magnetic field mitigation of MV/LV substations. *IEEE Latin America Transactions*, 2014, vol.12, no.6, pp. 1055-1061. **doi: 10.1109/tla.2014.6894000**.

11. Shydlovskyi A.K., Rozov V.Yu. The system of automatic compensation of external magnetic fields of energy-objects. *Technical electrodynamics*, 1996, no.1, pp. 3-9. (Rus).

12. Rozov V.Yu., Rezinkina M.M., Dumanskiy Yu.D., Gvozdenko L.A. The study of man-caused distortions in the geomagnetic field of residential and industrial buildings and to identify ways to reduce them to a safe level. *Technical electrodynamics. Thematic issue «Problems of modern electrical engineering»*. 2008, chapter 2, pp. 3-8. (Rus).

13. Kuznetsov B.I., Nikitina T.B., Bovdui I.V. High voltage power lines magnetic field system of active shielding with compensation coil different spatial arrangement. *Electrical engineering & electromechanics*, 2019, no.4, pp. 17-25. **doi: 10.20998/2074-272X.2019.4.03.**

14. Kuznetsov B.I., Nikitina T.B., Bovdui I.V. Active shielding of power frequency magnetic field in buildings in the vicinity of the electric airlines. *Problemele energeticii regionale*, 2019, no. 1-1(40), pp. 11-24. **doi: 10.5281/zenodo.3239130.**

15. Rozov V.Yu., Grinchenko V.S., Pelevin D.Ye., Chunikhin K.V. Simulation of electromagnetic field in residential buildings located near overhead lines. *Technical Electrodynamics*, 2016, no. 3, pp. 6-8. (Rus). **doi: 10.15407/techned2016.03.006.**

16. Pelevin D.Ye Screening magnetic fields of the power frequency by the walls of houses. *Electrical engineering & electromechanics*, 2015, no. 4, pp. 53-55. (Rus). **doi: 10.20998/2074-272X.2015.4.10.**

Received 04.05.2020

V.Yu. Rozov[1], *Professor, Corresponding member of NAS of Ukraine,*
K.D. Kundius[1], *Postgraduate Student,*
D.Ye. Pelevin[1], *Candidate of Technical Science,*
[1] State Institution «Institute of Technical Problems
of Magnetism of the NAS of Ukraine»,
19, Industrialna Str., Kharkiv, 61106, Ukraine,
e-mail: Rozov@nas.gov.ua, pelevindmitro@ukr.net

How to cite this article:
Rozov V.Yu., Kundius K.D., Pelevin D.Ye. Active shielding of external magnetic field of built-in transformer substations. *Electrical engineering & electromechanics*, 2020, no. 3, pp. 24-30. **doi: 10.20998/2074-272X.2020.3.04.**

UDC 621.3.07 **doi: 10.20998/2074-272X.2020.3.05**

N.J. Khlopenko

CALCULATION AND DESIGN OF A ROBUST SPEED CONTROLLER OF A FREQUENCY-CONTROLLED INDUCTION ELECTRIC DRIVE

Purpose. The aim of the work is the calculation and design of a robust speed controller of a frequency-controlled induction electric drive with parametric uncertainty and the presence of interferences in the feedback channel. Methodology. The calculation and design of the controller was carried out in four stages. At the first stage, a linearized mathematical model of the control object with parametric uncertainty was constructed and the transfer function of the H∞-suboptimal controller was calculated in the Robust Control Toolbox using the mixed sensitivity method. At the second stage, the stability of the robust system and the accuracy of stabilization of the induction machine speed with random variations of the object's and controller's uncertain parameters within the specified boundaries were explored. At the third stage, the influence of interferences arising in the feedback channel on the speed of the electric motor was explored in the Simulink package. At the final stage, the transfer function of the H∞-suboptimal controller was decomposed into a continued fraction using the Euclidean algorithm. This fraction was used to build the electric scheme of the controller. Results. Computer modelling of the transfer function of H∞-suboptimal controller, the robust stabilization system for the speed of the frequency-controlled electric drive with random variations of the uncertain parameters of the object and the controller at specified boundaries, as well as with the presence of varying intensity interferences in the feedback channel, was carried out. The choice of variable parameters was carried out according to the Monte-Carlo method. The curves of transient processes of the induction machine speed with parametric uncertainty and at different ranges of interference are constructed, as well as a Bode diagram for an open system. By the scatter of the obtained curves of the transient processes, the accuracy of speed stabilization of the machine was determined, and according to the Bode diagram, stability reserves in the amplitude and the phase of the robust system were determined. They are within tolerances with comparatively large deviations of the varied parameters and the range of interferences. Based on the investigations, an electrical circuit of the H∞-suboptimal robust controller was developed. Originality. The mathematical model has been developed and the methodology for calculating and designing of H∞-suboptimal robust speed controller of the frequency-controlled system of an induction electric drive with random variations of the uncertain parameters of the object and the controller at determined boundaries and the presence of interferences in the feedback channel, ensuring the stability of the system with allowable reserves of the amplitude and the phase and high accuracy of speed stabilization of the machine within the tolerances of uncertain system parameters and interferences was proposed. Practical value. The obtained structure of the controller from analog elements makes it possible to carry out modernization of the electric drives frequency-controlled systems in operation with minimal financial costs. References 11, figures 7.

Key words: **induction electric drive, frequency control, robust controller, electric circuit.**

Мета. Метою роботи є розрахунок і проектування робастного регулятора швидкості системи частотного управління асинхронного електроприводу з параметричною невизначеністю та наявністю перешкод в каналі зворотного зв'язку. Методологія. Розрахунок і проектування регулятора проводився в чотири етапи. На першому етапі будувалася лінеаризована математична модель об'єкта управління з параметричною невизначеністю і розраховувалася в пакеті Robust Control Toolbox передавальна функція H∞-субоптимального регулятора за методом мішаної чутливості. На другому етапі досліджувалася стійкість робастної системи і точність стабілізації швидкості асинхронної машини при випадкових варіаціях невизначених параметрів об'єкта і регулятора в заданих межах. На третьому етапі вивчався в пакеті Simulink вплив перешкод, що виникають в каналі зворотного зв'язку, на швидкість електродвигуна. На заключному етапі виконувалося розвинення передавальної функції H∞-субоптимального регулятора в ланцюгову дріб за алгоритмом Евкліда. Ця дріб використовувалася для побудови електричної схеми регулятора. Результати. Проведено комп'ютерне моделювання передавальної функції H∞-субоптимального регулятора, системи робастної стабілізації швидкості частотно-регульованого електроприводу при випадкових варіаціях невизначених параметрів об'єкта і регулятора в заданих межах, а також при наявності перешкод різної інтенсивності в каналі зворотного зв'язку. Вибір варійованих параметрів здійснювався за методом Монте-Карло. Побудовано криві перехідних процесів швидкості асинхронної машини з параметричною невизначеністю і при розмахах перешкод, а також діаграма Боде для розімкнутої системи. За розкидом отриманих кривих перехідних процесів визначалася точність стабілізації швидкості машини, а по діаграмі Боде – запаси стійкості за амплітудою і фазою робастної системи. Вони знаходяться в межах допусків при порівняно великих відхиленнях варійованих параметрів і розмахах перешкод. На базі проведених досліджень розроблено електричну схему H∞-субоптимального робастного регулятора. Новизна. Розроблена математична модель та запропонована методика розрахунку і проектування H∞-субоптимального робастного регулятора швидкості системи частотного управління асинхронного електроприводу при випадкових варіаціях невизначених параметрів об'єкта і регулятора в заданих межах і наявності перешкод в каналі зворотного зв'язку, яка забезпечує стійкість системи з запасами за амплітудою і фазою, що допускаються, та високу точність стабілізації швидкості машини в межах допусків невизначених параметрів системи і перешкод. Практичне значення. Отримана структура регулятора з аналогових елементів дає можливість проводити модернізацію систем частотного управління електроприводів, що знаходяться в експлуатації, з мінімальними фінансовими витратами. Бібл. 11, рис. 7.

Ключові слова: **електропривод асинхронний, частотне управління, робастний регулятор, електрична схема.**

Цель. Целью работы является расчет и проектирование робастного регулятора скорости частотно-регулируемого асинхронного электропривода с параметрической неопределенностью и наличием помех в канале обратной связи.

Методология. Расчет и проектирование регулятора проводился в четыре этапа. На первом этапе строилась линеаризованная математическая модель объекта управления с параметрической неопределенностью и рассчитывалась в пакете Robust Control Toolbox передаточная функция H_∞-субоптимального регулятора по методу смешанной чувствительности. На втором этапе исследовалась устойчивость робастной системы и точность стабилизации скорости асинхронной машины при случайных вариациях неопределенных параметров объекта и регулятора в заданных границах. На третьем этапе изучалось в пакете Simulink влияние помех, возникающих в канале обратной связи, на скорость электродвигателя. На заключительном этапе выполнялось разложение передаточной функции Н∞-субоптимального регулятора в цепную дробь по алгоритму Евклида. Эта дробь использовалась для построения электрической схемы регулятора. Результаты. Проведено компьютерное моделирование передаточной функции H_∞-субоптимального регулятора, системы робастной стабилизации скорости частотно-регулируемого электропривода при случайных вариациях неопределенных параметров объекта и регулятора в заданных границах, а также при наличии помех различной интенсивности в канале обратной связи. Выбор варьируемых параметров осуществлялся по методу Монте-Карло. Построены кривые переходных процессов скорости асинхронной машины с параметрической неопределенностью и при размахах помех, а также диаграмма Боде для разомкнутой системы. По разбросу полученных кривых переходных процессов определялась точность стабилизации скорости машины, а по диаграмме Боде – запасы устойчивости по амплитуде и фазе робастной системы. Они находятся в пределах допусков при сравнительно больших отклонениях варьируемых параметров и размахах помех. На базе проведенных исследований разработана электрическая схема H_∞-субоптимального робастного регулятора. Новизна. Разработана математическая модель и предложена методика расчета и проектирования H_∞-субоптимального робастного регулятора скорости системы частотного управления асинхронного электропривода при случайных вариациях неопределенных параметров объекта и регулятора в заданных границах и наличии помех в канале обратной связи, обеспечивающая устойчивость системы с допускаемыми запасами по амплитуде и фазе и высокую точность стабилизации скорости машины в пределах допусков неопределенных параметров системы и помех. Практическое значение. Полученная структура регулятора из аналоговых элементов дает возможность проводить модернизацию систем частотного управления электроприводов, находящихся в эксплуатации, с минимальными финансовыми затратами. Библ. 11, рис. 7.

Ключевые слова: **электропривод асинхронный, частотное управление, робастный регулятор, электрическая схема.**

Introduction. In frequency-controlled induction electric drives operating in conditions of uncertainty, the task of robust stabilization of the motor speed with a given accuracy is essential. Several methods are known [1-5], which are most often used at different times by domestic and foreign scientists to solve this problem. Of these, the method of synthesizing the stabilizing H_∞-suboptimal robust regulator is most widely used. In [6-9], on the basis of this method, a scientific research methodology, a calculation procedure, and an electrical circuit of a stabilizing H_∞-controller of the rotor flux linkage control system for random variations of undefined parameters at specified boundaries and interference in the feedback channel are developed.

In the present work, this methodology is used to construct a mathematical model as well as a method for calculating and designing the electrical circuit of the H_∞-suboptimal robust speed controller of the frequency control system of an induction electric drive.

The goal of the work is the calculation and design of a robust speed controller for the frequency control system of an induction electric drive with parametric uncertainty and the presence of interference in the feedback channel.

Research methods and results. Figure 1 is a structural diagram of the mechanical characteristic of the control object linearized within the working area in the input-output signal space [10, 11]. It contains the transfer functions of a frequency converter with the transmission coefficient K_{fc} and the time constant T_{fc} and a squirrel-cage induction motor. An induction motor is represented by a first-order aperiodic link with the stiffness module β and the electromagnetic time constant T_{e} and an integrating link with inertia moment J, taking into account the inertia moment of the actuator reduced to the rotor axis. The load torque (static moment of resistance) will be considered constant and applied to the rotor in steady state. Therefore, its increment M_{rs} at the working point of the static mechanical characteristic is neglected. The increment of the electromagnetic torque M of the motor at the same point is taken equal to this torque [10, 11].

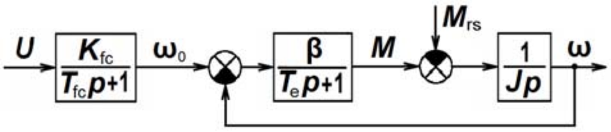

Fig. 1. Structural diagram of an induction electric drive

We pass from the structural diagram of the object to the equations of state in normal operator form:

$$p\omega = \frac{1}{J}M;$$
$$pM = -\frac{1}{T_{\text{e}}}M + \frac{\beta}{T_{\text{e}}}(\omega_0 - \omega); \qquad (1)$$
$$p\omega_0 = -\frac{1}{T_{\text{fc}}}\omega_0 + \frac{K_{\text{fc}}}{T_{\text{fc}}}U,$$

where

$$\beta = \frac{2M_{\text{cr}}}{\omega_{0\text{n}}s_{\text{cr}}}; \quad T_{\text{e}} = \frac{1}{z_{\text{p}}\omega_{0\text{n}}s_{\text{cr}}}; \qquad (2)$$

p is the Laplace operator; U is the control action; ω, ω_0 are the angular speed of the rotor and the rotating magnetic field relative to the stator, respectively; M, M_{cr} are, respectively, the electromagnetic and critical torques of the motor; s_{cr} is the critical slip; z_{p} is the number of pole pairs; n is the index of nominal values.

We introduce dimensionless quantities

$$x_1 = \frac{\omega}{\omega_{\text{n}}}; \; x_2 = \frac{M}{M_{\text{n}}}; \; x_3 = \frac{\omega_0}{\omega_{0\text{n}}}; \; u = \frac{U}{U_{\text{n}}}. \qquad (3)$$

We turn in equations (1) to dimensionless variables (3). Then, taking into account (2), we obtain the following equations of state of the object:

$$px_1 = \frac{M_n}{J\omega_n}x_2;$$
$$px_2 = 2z_p M_{cr}\left(\frac{\omega_{0n}}{M_n}x_3 - \frac{1}{\beta}x_2 - \frac{\omega_n}{M_n}x_1\right); \qquad (4)$$
$$px_3 = -\frac{1}{T_{fc}}x_3 + \frac{K_{fc}}{T_{fc}K_{fc\,n}}u.$$

Using equations (4), we construct a structural diagram of the object in the state space (Fig. 2).

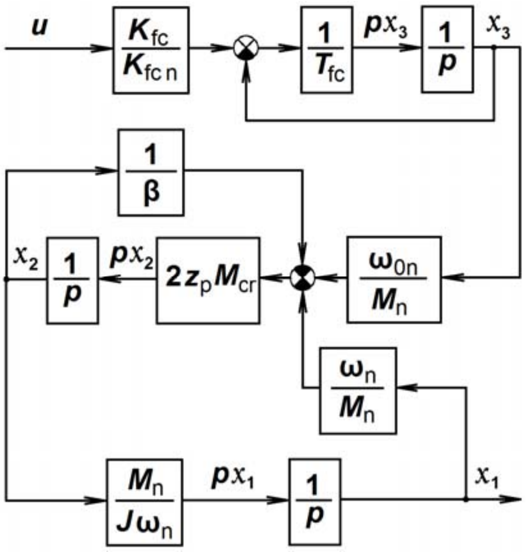

Fig. 2. Structural diagram of the control object in the state space

In this circuit, for the uncertain parameters that are most sensitive to changes in the object model, we take the transfer coefficient K_{fc} of the frequency converter, the critical torque M_{cr}, the stiffness module β, and the moment of inertia J of the induction motor.

Suppose that the indefinite system parameters K_{fc}, M_{cr}, β and J vary in the intervals:

$$K_{fc} = K_{fc\,n}(1 + p_{K_{fc}}\delta_{K_{fc}});$$
$$M_{cr} = M_{cr\,n}(1 + p_{M_{cr}}\delta_{M_{cr}}); \qquad (5)$$
$$\beta = \beta_n(1 + p_\beta\delta_\beta);$$
$$J = J_n(1 + p_J\delta_J),$$

where $p_{K_{fc}}$, $p_{M_{cr}}$, p_β, p_J are the coefficients that take into account the deviations of the relative values of the uncertain parameters $\delta_{K_{fc}}$, $\delta p_{M_{cr}}$, δ_β and δ_J.

We replace each of the parameters (5) presented in Fig. 2, by a structural diagram. As a result, we obtain a structural diagram of an object with parametric uncertainty, shown in Fig. 3.

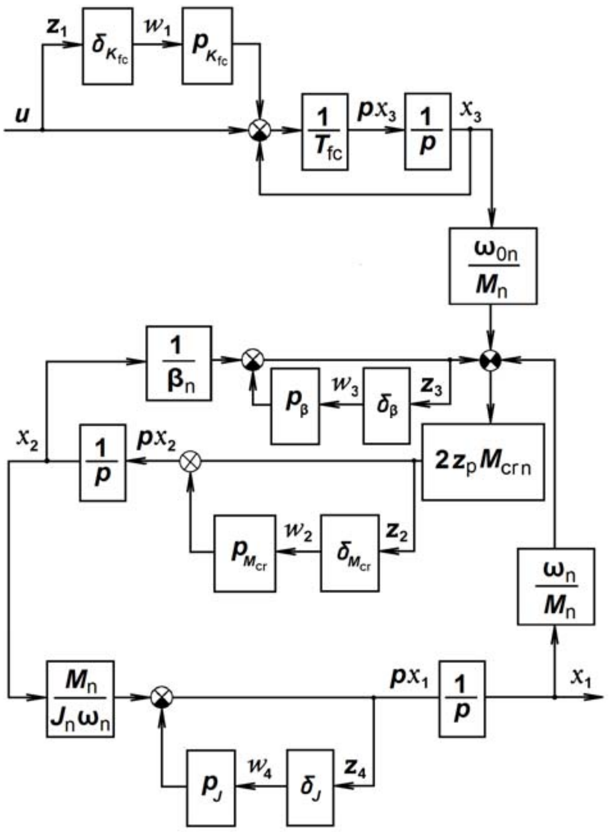

Fig. 3. Structural diagram of the control object with undefined parameters

Let's pass from the structural diagram shown in Fig. 3, to matrix equations of state in canonical form:

$$px = Ax + B_1w + B_2u;$$
$$z = C_1x + D_{11}w + D_{12}u; \qquad (6)$$
$$y = C_2x + D_{21}w + D_{22}u,$$

where

$$A = \begin{bmatrix} 0 & \frac{M_n}{J_n\omega_n} & 0 \\ -\frac{2z_p\omega_n M_{cr\,n}}{M_n} & -\frac{2z_pM_{cr\,n}}{\beta_n} & \frac{2z_p\omega_{0\,n}M_{cr\,n}}{M_n} \\ 0 & 0 & -\frac{1}{T_{fc}} \end{bmatrix};$$

$$B_1 = \begin{bmatrix} 0 & 0 & 0 & -p_J \\ 0 & 0 & 2z_pM_{cr\,n}p_\beta & 0 \\ \frac{p_{K_{fc}}}{T_{fc}} & 0 & 0 & 0 \end{bmatrix};$$

$$C_1 = \begin{bmatrix} 0 & 0 & 0 \\ -\frac{2z_p\omega_n M_{cr\,n}}{M_n} & -\frac{2z_pM_{cr\,n}}{\beta_n} & \frac{2z_p\omega_{0\,n}M_{cr\,n}}{M_n} \\ 0 & \frac{1}{\beta_n} & 0 \\ 0 & \frac{M_n}{J_n\omega_n} & 0 \end{bmatrix};$$

$$B_2^T = \begin{bmatrix} 0 & 0 & \dfrac{1}{T_{\text{fc}}} \end{bmatrix};\; C_2 = \begin{bmatrix} 1 & 0 & 0 \end{bmatrix};$$

$$D_{11} = \begin{bmatrix} 0 & 0 & 0 & 0 \\ 0 & 0 & 2z_p M_{\text{cr n}} p_\beta & 0 \\ 0 & 0 & -p_\beta & 0 \\ 0 & 0 & 0 & -p_J \end{bmatrix};\; D_{12}^T = \begin{bmatrix} 1 & 0 & 0 & 0 \end{bmatrix};$$

$$D_{21} = \begin{bmatrix} 0 & 0 & 0 & 0 \end{bmatrix};\; D_{22} = \begin{bmatrix} 0 \end{bmatrix};$$

$x = (x_1, x_2, x_3)^T$ is the phase vector; y is the one-dimensional output vector along which feedback is closed; $z = (z_1, z_2, z_3, z_4)^T$, $w = (w_1, w_2, w_3, w_4)^T$ are the input and output uncertainty vectors, which are related by the matrix expression $w(p) = \Delta(p) \cdot z(p)$ in which the uncertainty matrix $\Delta(p)$ has a diagonal form.

The resulting system of equations (6) allows, together with the weighting functions proposed in [4] for quality control of a robust system, to calculate the transfer function of the H_∞-suboptimal controller for a nominal object in the Robust Control Toolbox package using the mixed sensitivity method. For an induction electric drive with MDXMA 100-32 motor with power of 3 kW, parameters $z_p = 2$; $M_n = 20.2$ N·m; $M_{\text{cr n}} = 48.5$ N·m; $J_n = 0.013$ kg·m^2; $\omega_n = 148.178$ rad/s; $\omega_{0n} = 157.08$ rad/s; $\beta_n = 1.908$ N·m/(rad/s) and a frequency converter with the transmission coefficient $K_{\text{fc}} = 1.06$ rad/(V·s) and the time constant $T_{\text{fc}} = 10^{-4}$ s, the calculated transfer function of the H_∞-controller turned out to be equal to:

$$K(p) = \frac{b_1 p^2 + b_2 p + b_3}{a_1 p^3 + a_2 p^2 + a_3 p + a_4}, \tag{7}$$

where $a_1 = 1$; $a_2 = 1.524 \cdot 10^5$; $a_3 = 1.261 \cdot 10^6$; $a_4 = 4.729 \cdot 10^6$; $b_1 = 3.53 \cdot 10^5$; $b_2 = 7.385 \cdot 10^6$; $b_3 = 5.681 \cdot 10^8$.

Using the MATLAB commands, we attach the robust controller (7) and the unit feedback encompassing the «H_∞-controller-object» system to the object (4) programmatically. Using the Monte Carlo method [4], we study the accuracy of stabilization of the angular speed of the machine and the stability of the resulting system with random variations of the uncertain parameters of the object K_{fc}, M_{cr} in the range of ±15 %, β in the range of ±30 %, J in the range of ±25 % and the coefficients a_1, a_2, a_3, a_4, b_1, b_2, b_3 of the regulator (7) in the range of ±15 %.

Figure 4 presents 20 generated transient curves of the angular speed of the rotor of the induction motor with a single spasmodic change in the signal at the input of the system and a random selection of the uncertain parameters of the object and controller from the given ranges by the Monte Carlo method.

As expected, presented in Fig. 4 curves do not go beyond the boundaries of the 3 % tube.

To study the stability of the system, we apply the method of logarithmic frequency characteristics with a random selection by the Monte Carlo method of the indefinite parameters of the object and controller in the given ranges.

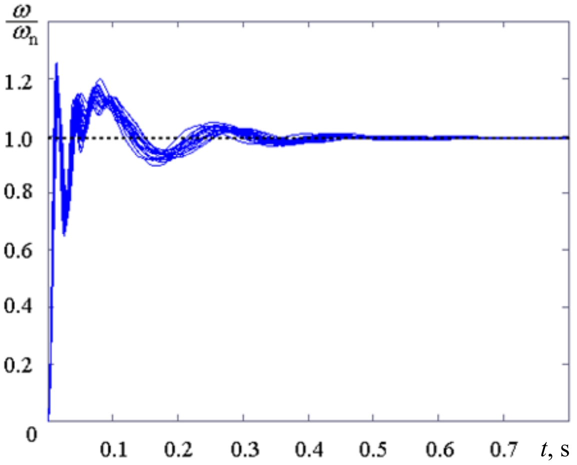

Fig. 4. Transients of the rotor angular speed

Figure 5 shows a Bode diagram with 20 generated curves of amplitude $L(\omega)$ and with 20 curves of phase $\varphi(\omega)$ frequency response curves for the same parameters what were used to calculate the curves shown in Fig. 4.

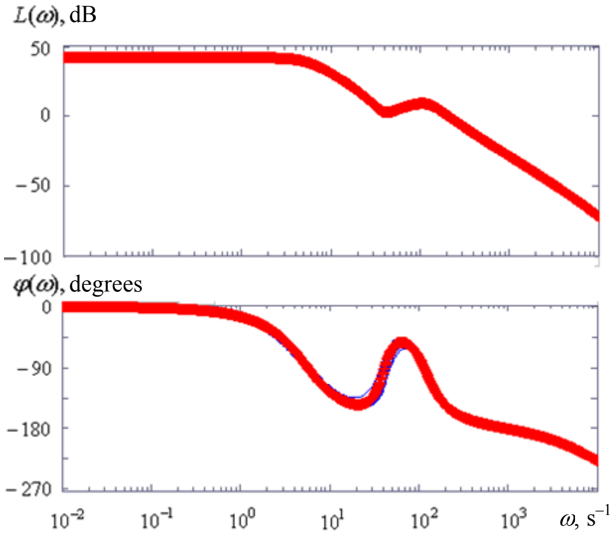

Fig. 5. Open system's Bode diagram

From the amplitude $L(\omega)$ and phase $\varphi(\omega)$ characteristics presented in this diagram, it can be seen that the system is stable, since the amplitude characteristic crosses the abscissa axis earlier than the phase characteristic, finally decaying, goes over the angle value of –180°. In this case, the calculated value of the stability margin in amplitude is 23.12 dB, and in phase – 31.75 ° for the nominal values of the parameters of the object and the regulator with scatter of random curves not exceeding 4 dB for amplitude and 15° for phase frequency characteristics.

We proceed to the construction of the electrical circuit of the H_∞-suboptimal robust controller.

We decompose the transfer function (7) into a continued fraction according to the Euclidean algorithm:

$$\frac{1}{\frac{28,33}{10^7}p+\frac{1}{2,32+\frac{1}{\frac{34,1}{10^3}p+\frac{1}{-0,252+\frac{1}{-\frac{31,78}{10^3}p+\frac{1}{r}}}}}},\quad(8)$$

where $r = 118.1$.

The electric circuit of the controller corresponding to the fraction (8) is shown in Fig. 6. When it was created, well-known methods and rules for performing electrical circuits were used.

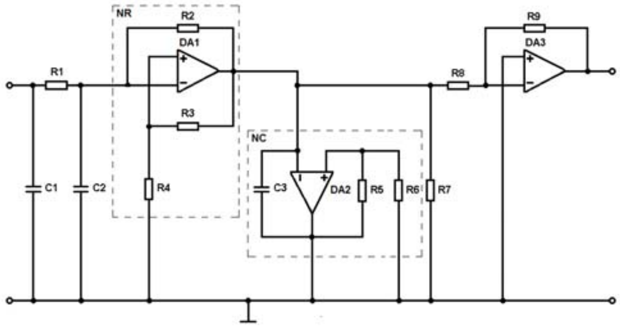

Fig. 6. Electric circuit of a robust controller

The circuit shown in Fig. 6, is made in the form of a four-terminal network and consists of a series-connected the first passive four-terminal network with a capacitor C1 connected in parallel, the second passive four-terminal network with a resistor R1 connected in series and a parallel capacitor C2, the third active four-terminal network with a negatron of the negative resistance NR in series, consisting of an operational amplifier DA1 and resistances R2, R3, R4, the fourth active four-terminal with a parallel connected negatron of the negative capacitance NC, consisting of an operational amplifier DA2, a capacitor C3 and resistors R5, R6, the fifth passive four-terminal with a parallel resistor R7, and an operational amplifier DA3 with resistors R8 and R9 connected to the output of the fifth four-terminal.

Parameters of its capacitors and resistors C1 = 28.4 pF; R1 = 2.32 kΩ; C2 = 34 μF; R2 = 252 Ω; C3 = 31.8 μF; R7 = 118 kΩ; R8 = 1 MΩ; R9 = 1 kΩ and they correspond to the standard values of rounded coefficients, fraction (8) when multiplying its numerator and denominator by a certain constant number, and R3 = R4 and R5 = R6 are chosen from design considerations.

As calculations performed by the method of [7] show, at such capacitance and resistance values, the values of the coefficients a_1, a_2, a_3, a_4, b_1, b_2, b_3 of controller (7) do not go beyond the limits of the range specified above ±15 %.

In the robust control system, interferences can occur, caused, for example, by sensor noise, connector pins, electromagnetic fields, interference with the frequency of the supply network and other reasons. A robust regulator, as an element of this system, is known to be able to filter these interferences. Therefore, the calculations of transients of the angular speed of the electric motor were performed at various values of the noise intensity in the feedback channel of the frequency control system with a robust controller. The calculations were carried out in the Simulink package. A static motor load of $0.75{\cdot}M_\text{n}$ was applied to the rotor of the machine in steady state.

The results of calculating the curves of transients of the angular speed of the rotor, filtered by the robust control system, for two different values of the generated span of interference with a single spasmodic change in the reference action are shown in Fig. 7.

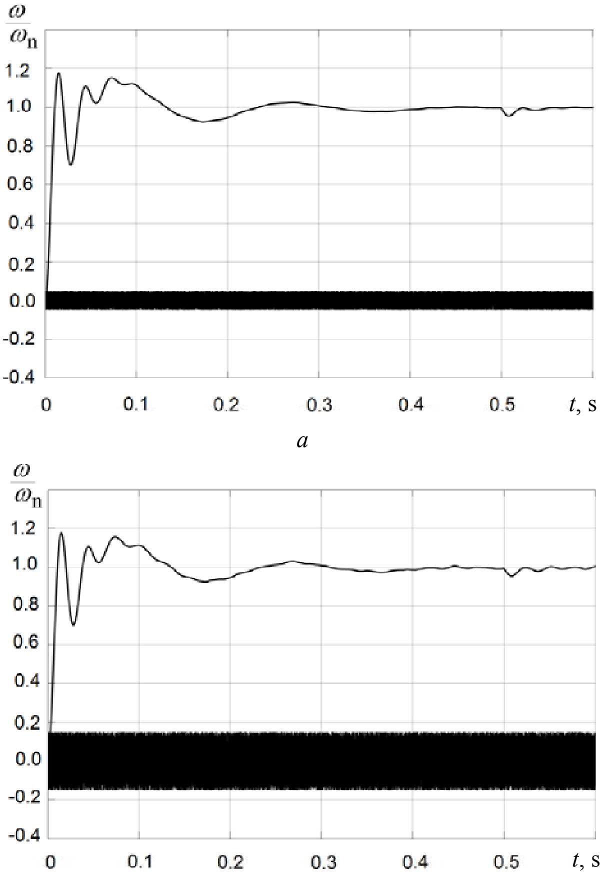

Fig.7. Transients of the angular speed ω/ω_n with interferences filtered by a robust system and a rotor load of $0.75M_\text{n}$ at time 0.5 s: *a* – interference span of 10 %; *b* – 30 %

An analysis of these curves shows that the level of interference filtering by the robust system largely depends on the intensity of the interference span and in the steady state it is within the tolerance range of ±2.5 %, except for the local area of the application of the M_rs load at 0.5 s.

Conclusions.

1. A mathematical model and a technique for calculating and designing an electrical circuit of the H_∞-suboptimal robust speed controller of the frequency control system of an induction electric drive with random variations of the uncertain parameters of the object and the controller within the specified boundaries and the presence of interferences in the feedback channel are developed.
2. The results of modelling of transients of the angular speed of the rotor according to the developed technique confirm the high accuracy of stabilization with random

variations of uncertain parameters at given boundaries and low sensitivity to interferences in the feedback channel.

REFERENCES

1. Balandyn D.V., Kogan, M.M. *Sintez zakonov upravlenija na osnove linejnyh matrichnyh neravenstv* [Synthesis of control rules based on linear matrix inequalities]. Moscow, Fizmatlit Publ., 2007. 280 p. (Rus).

2. Pupkov K.A., Egupov I.D. *Metody klassicheskoi i sovremennoi teorii avtomati-cheskogo upravleniia: Uchebnik v 5 tomakh. Tom 3: Sintez reguliatorov sistem avtomaticheskogo upravleniia* [Methods of the classical and modern theory of automatic control: A textbook in 5 vols. Vol. 3: Synthesis of regulators of automatic control systems]. Moscow, Bauman Moscow State Technical University Publ., 2004. 616 p. (Rus).

3. Nikitina T.B. Pareto optimal solution of multiobjective synthesis of robust controllers of multimass electromechanical systems based on multiswarm stochastic multiagent optimization. *Electrical engineering & electromechanics*, 2017, no. 2, pp. 34-38. **doi: 10.20998/2074-272X.2017.2.05.**

4. Richard Y., Chiang R., Michael G., Safonov M. *MATLAB: Robust Control Toolbox. User's Guide. Version 2*, 1998. 230 p. Available at: http://www.mathworks.com (Accessed 14 May 2018).

5. Rigatos G., Siano P., Wira P., Profumo F. Nonlinear H-infinity Feedback Control for Asynchronous Motors of Electric Trains. *Intelligent Industrial Systems*, 2015, vol. 1, no. 2, pp. 85-98. **doi:10.1007/s40903-015-0020-y.**

6. Khlopenko N.J., Khlopenko I.N. Structural synthesis of a stabilizing robust controller of the rotor flux linkage. *Electrical engineering & electromechanics*, 2017, no. 1, pp. 21-25. (Rus). **doi: 10.20998/2074-272X.2017.1.04.**

7. Khlopenko I.N., Rozhkov S.A., Khlopenko N.J. Stability and accuracy of the robust system for stabilizing the rotor flux-linkage of an asynchronous electric drive at random variations of the uncertain parameters within the specified boundaries. *Electrical engineering & electromechanics*, 2018, no.4, pp. 35-39. **doi: 10.20998/2074-272X.2018.4.06.**

8. Khlopenko N., Rozhkov S., Khlopenko I. Filtration Of Undesired Signals By The Robust Controller In The Rotor Flux-Linkage Control System. *Scientific Bulletin Kherson State Maritime Academy*, 2019, vol. 1, no. 20, pp. 122-131. (Rus). **doi: 10.33815/2313-4763.2019.1.20.122-131.**

9. Khlopenko N.Y., Rozhkov S.O., Khlopenko I.M. *Sistema vektornogo keruvannya shvidkistyu asinhronnogo elektrodviguna* [Asynchronous motor vector speed control system]. Patent UA, no. 137157, 2019. (Ukr).

10. Kliuchev V.I. *Teoriia elektroprivoda* [Theory of the electric drive]. Moscow, Energoatomizdat Publ., 2001. 704 p. (Rus).

11. Usol'tsev A.A. *Chastotnoe upravlenie asinkhronnymi dvigateliami: uchebnoe posobie* [Frequency Control of Asynchronous Motors: A Tutorial]. St. Petersburg, SPbGU ITMO Publ., 2006. 94 p. (Rus).

Received 26.03.2020

N.J. Khlopenko, Doctor of Technical Science, Professor,
Kherson State Marine Academy,
20, Ushakov Ave., Kherson, 73009, Ukraine,
e-mail: khlopenko.n@gmail.com

How to cite this article:
Khlopenko N.J. Calculation and design of a robust speed controller of a frequency-controlled induction electric drive. *Electrical engineering & electromechanics*, 2020, no. 3, pp. 31-36. **doi: 10.20998/2074-272X.2020.3.05.**

UDC 621.314 **doi: 10.20998/2074-272X.2020.3.06**

Y.O. Onikienko, V.V. Pilinsky, P.V. Popovych, V.S. Lazebnyi, O.I. Smolenska, V.S. Baran

MODELLING OF OPERATION MODES AND ELECTROMAGNETIC INTERFERENCES OF GaN-TRANSISTOR CONVERTERS

***Goal.** To analyze the efficiency and EMI of a half-bridge converter built on GaN transistors at different switching frequencies and to issue recommendations for its application. **Methodology.** An EPC9035 development board from Efficient Power Conversion was selected for research. This board is a half-bridge converter built on the EPC2022 eGaN® transistors and contains a driver for controlling these transistors. To simplify the assessment of the conversion efficiency, it is suggested to use a computer model of the development board and LISN, which simulates the active load with the LC filter. **Results.** Simulation results of the converter efficiency with the nominal values of the elements according to the EPC9035 manual showed significant deviations from the calculated values at frequencies above 50 kHz. This is explained by the presence of inrush current through transistors. The inrush current depends on the «dead time» between the intervals when the transistors are open and the delays specified in the SPICE model of LM5113 driver. To reduce the amplitude of inrush current and, accordingly, to increase the duration of the «dead time» interval, it is proposed to double the capacitors responsible for the formation of this interval. Simulation of the converter efficiency with the doubled values of the circuit elements showed that the results almost coincide with the calculated values of the efficiency in the range from 0.05 MHz to 5 MHz. The converter on the EPC2022 transistors has the highest efficiency at 50 kHz which decreases by 0.03-0.04 at 500 kHz. Therefore, it is recommended that the operating frequency should be set close to 500 kHz. Simulation of EMI levels resulted that the difference in the duration of the «dead time» does not have a significant effect on the levels of simulated EMI. The largest difference between the simulation results and the experiment is observed at frequencies about 30 MHz and is 3-6 dB. **Originality.** For the first time, the computer model was used to calculate the efficiency of a half-bridge converter on GaN transistors at different frequencies. **Practical significance.** Considering the high output current, high operating voltage and short switching times, GaN transistors are promising for use in pulse generators, power supplies with operating frequencies exceeding 500 kHz, and in powerful Class D hi-fi amplifiers with small dimensions, such as automotive ones.* References 10, tables 3, figures 5.

Key words: **GaN transistors, computer simulation, electromagnetics interferences, energy efficiency.**

У роботі досліджено вплив частоти перетворення на ефективність роботи напівмостового перетворювача на GaN транзисторах. Наведено результати комп'ютерного моделювання такого перетворювача з урахуванням втрат на різних частотах. Показано, що запропонована комп'ютерна модель дозволяє визначити рівень струму споживання, а, отже, і ККД напівмостового перетворювача на GaN транзисторах. Моделювання з параметрами, взятими зі схеми від виробника призводить до завищених оцінок споживання струму до 2,3 рази. Зміна параметрів RC-кіл, що формують інтервал «мертвого часу» транзисторів зменшує похибку визначення струму споживання до менш як 5 %. Збільшення тривалості «мертвого часу» суттєво не впливає на точність моделювання несиметричних електромагнітних завад і призводить до зміни їх рівня в межах 3 дБ. У результаті дослідження встановлено, що комп'ютерна модель має достатню точність для оціночних розрахунків, а розглянуті перетворювачі на GaN транзисторах найкраще використовувати з частотами перетворення близько 500 кГц. Такі перетворювачі можуть знайти застосування в джерелах живлення бортової апаратури і автомобільних підсилювачах класу D. Бібл. 10, табл. 3, рис. 5.

Ключові слова: **GaN-транзистори, комп'ютерне моделювання, електромагнітні завади, енергоефективність.**

В работе исследовано влияние частоты переключения на эффективность работы полумостового преобразователя на GaN транзисторах. Приведены результаты компьютерного моделирования такого преобразователя с учетом потерь на разных частотах. Показано, что предложенная компьютерная модель позволяет определить уровень тока потребления, а, следовательно, и КПД полумостового преобразователя на GaN транзисторах. Моделирование с параметрами, взятыми из схемы от производителя, дает завышенное потребление тока до 2,3 раз. Изменение параметров RC-цепей, задающих интервал «мертвого времени» транзисторов уменьшает погрешность определения тока потребления до менее 5 %. При этом, увеличение продолжительности «мертвого времени» не влияет в значительной степени на точность моделирования несимметричных электромагнитных помех, изменяя их уровень в пределах 3 дБ. В результате исследования установлено, что компьютерная модель имеет достаточную точность для оценочных расчетов, а рассмотрены преобразователи на GaN транзисторах лучше использовать на частотах переключения около 500 кГц. Такие преобразователи могут найти применение в источниках питания для бортовой аппаратуры и автомобильных усилителях класса D. Библ. 10, табл. 3, рис. 5.

Ключевые слова: **GaN-транзисторы, компьютерное моделирование, электромагнитные помехи, энергоэффективность**.

Introduction. In recent years, transistors based on gallium nitride (GaN) and silicon carbide (SiC) have become widespread. Such transistors have low control and switching losses, short switching time and good heat transfer. These properties give GaN transistors a number of advantages over silicon (Si) MOSFET and IGBT transistors and expand their scope. At present, GaN transistors are promising substitutes for high-power Si transistors. Their use ensures compliance with modern requirements for reducing energy consumption and dimensions of electronic equipment. But GaN transistors are still relatively expensive. Due to their advantages, GaN and SiC transistors are widely used in radars, telecommunications equipment and are promising for many applications, where the requirements for high efficiency and small size come first. For example, for use in Class D audio amplifiers and electric drives.

For example, in [1] the results of a comparative analysis of the efficiency of GaN and SiC transistors utilization for high-speed electric drives are presented. Increasing the conversion frequency, due to the use of GaN transistors, has reduced the losses of the rotor in the drive with permanent magnets and increased its efficiency and specific power in general. In [2] the efficiency of three transistor rectifiers is compared: IGBT, MOSFET and GaN FET. Due to the low frequency (50 Hz) selected, the GaN converter did not show greater efficiency than the others, but provided a lower harmonic ratio. The use of SiC transistors instead of IGBT in high-power converters (up to 12 kW) does not provide an advantage in terms of efficiency, but allows them to be used at high operating temperatures [3].

In [4], the results of comparison of asymmetric (Common Mode) electromagnetic interferences (EMI) generated by Si and GaN transistors are presented. For the study, the authors chose both types of transistors, the characteristics of which are similar and little different. As a result, their study did not reveal a significant difference in interference levels in the standard frequency range from 150 kHz to 30 MHz. Differences occurred only at frequencies above 30 MHz.

The influence of the value of the decoupling capacitor on the level of EMI generated by a half-bridge converter on GaN transistors is studied in [5]. The effect of additional capacitance on both symmetric and asymmetric interference components using a computer model is estimated. Simulation is widely used for EMI analysis because it greatly simplifies the process of research and development of converters, provides ease of model construction and the ability to quickly change it. In addition, it saves money on the development process.

However, in the literature, insufficient attention has been paid to the justification for the choice of the conversion frequency of converters on GaN transistors. Therefore, it is advisable to create a computer model of the converter, to investigate which parameters can provide the highest efficiency and how the simulation results coincide with the experimental data.

The goal of the work is to analyze the efficiency and electromagnetic interference of a half-bridge converter on GaN transistors at different switching frequencies using its computer model and to form recommendations for its use.

To achieve this goal it was necessary to solve the following tasks:

- evaluate the efficiency of the converter on GaN transistors depending on the frequency of conversion;
- evaluate the adequacy of the computer model of the converter to calculate the efficiency when operating at different frequencies;
- evaluate the adequacy of the computer model for calculating the EMI of the converter, measured at the output of the network equivalent;
- based on the results of research to formulate recommendations to developers on the feasibility of using GaN transistors for various tasks.

Description of the computer model. The EPC9035 development board from Efficient Power Conversion was chosen for the research. This board is a half-bridge converter module implemented on EPC2022 eGaN® transistors and contains a driver for controlling these transistors. Table 1 shows the main parameters of the EPC9035 board.

Table 1

The main electrical and time characteristics of the development board EPC9035

Parameter	Value
Output voltage, V	80
Output current, A	25
Time of rise and fall of output voltage, ns	3-5
Resistance of transistors in the open state, mΩ	4
Minimum width of the input pulse in the «high» state, ns	50
Minimum width of the input pulse in the «low» state, ns	100

The on and off times of the transistor EPC2022 are indicated approximately, they were measured during the experiment.

Computer simulation of a half-bridge converter on GaN transistors has previously been performed using the EPC9062 board [6]. The paper also presents the results of EMI simulation when operating on active load. The model proposed below takes into account the differences in the design of the boards, the components used and simulates the operation on active load with an LC-filter. The computer model of the EPC9035 board, connected to the power supply via the network equivalent, is shown in Fig. 1. Logic elements U1 and U2 are used on the EPC9035 board as buffers and to invert the input signal. RC circuit consisting of R2, C2 and diode D1 forms a switching on delay of transistor Q1, RC circuit R7, C4 and diode D2 forms a switching on delay of transistor Q2. Chip U3 is the driver of transistors Q1 and Q2.

Components for modelling the process of EMI propagation and losses on the printed circuit board (throttles L1, L3, resistors R1, R10), four decoupling capacitors C8–C11 are presented in the diagram with parasitic parameters: throttles L8–L11 (inductance of terminals) and resistors R15–R18 (internal resistance). The parasitic parameters of the supply wires are presented by throttles L6, L13 and resistors R11, R20. The load of the converter is the throttle L2, the load resistor R9 and the filter capacitor C3 with the inductance of the terminals L4. The network equivalent is presented by capacitors C6, C7, C12, C13, throttles L5, L12 and resistors R12, R19. The input resistance of the selective microvoltmeter is presented by resistor R14. Resistor R13 takes into account the internal resistance of the power supply and the resistance of the power wires. Capacitor C5 takes into account the parasitic capacitance between the output of the converter and the «ground».

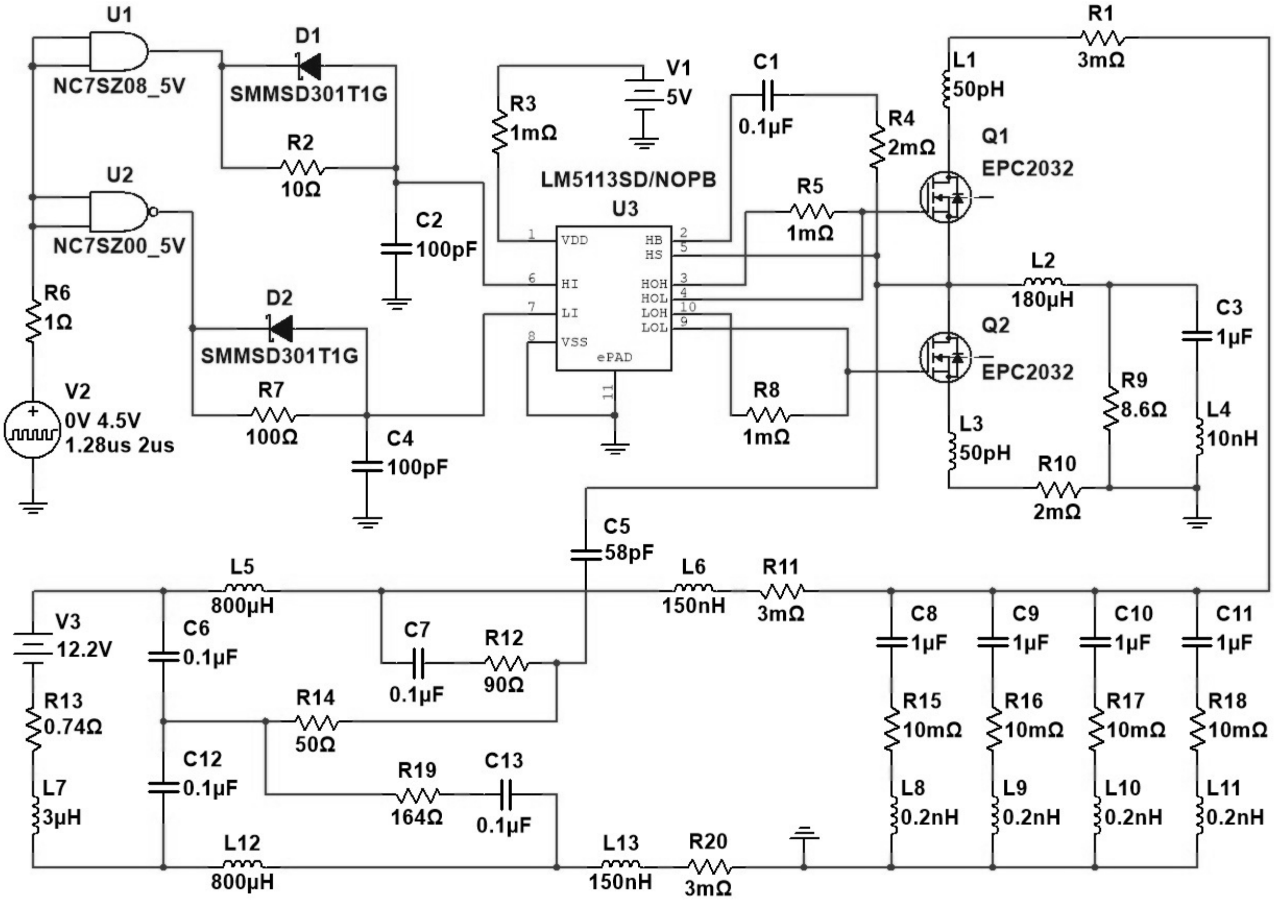

Fig. 1. Computer model of a half-bridge converter with network equivalent and power supply

Evaluation of energy efficiency of a half-bridge converter on GaN transistors. Figure 2 shows the oscillograms of the output voltage of GaN transistors EPC2022 during switching on (Fig. 2,*a*) and during switching off (Fig. 2,*b*).

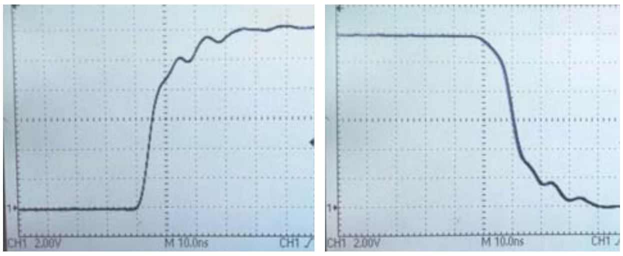

a *b*

Fig. 2. Shapes of output voltage pulse fronts of the half-bridge converter EPC9035:
a – pulse front, b – pulse fall

The power losses of the half-bridge converter are determined for each of the GaN transistors separately [7]. The total losses P_{Q1} of the transistor Q1 consist of losses in the open state P_{cond_Q1}, losses on recharging the output capacitance P_{OSS}, losses during switching on $P_{on\_overlap}$, losses during switching off $P_{off\_overlap}$, losses on recharging the input capacitance P_{G_Q1}. The total losses P_{Q2} of the transistor Q2 consist of losses in the open state P_{cond_Q2}, losses on recharging the output capacitance in reverse mode P_{OSS_sd}, losses on the built-in diode until the transistor opens P_{sd} and losses on recharging the input capacitance P_{G_Q2}. The losses of transistors Q1 and Q2 can be calculated by the formulas [8]:

$$P_{Q1} = P_{cond\_Q1} + P_{OSS} + P_{on\_overlap} + P_{off\_overlap} + P_{G\_Q1};$$

$$P_{Q2} = P_{cond\_Q2} + P_{OSS\_sd} + P_{sd} + P_{G\_Q2}.$$

For transistor Q1, the losses during switching off $P_{off\_overlap}$ and the losses on recharging the input capacitor recharge are insignificant and can be neglected. For transistor Q2, we can neglect the losses on recharging the output capacitor in the reverse mode P_{OSS_sd} and the losses on recharging the input capacitor P_{G_Q2}. Other types of losses can be determined by the formulas:

$$P_{cond\_Q1} = \left(I_{OUT}^2 + \frac{I_{ripple}^2}{12} \right) \cdot (D - t_{dt1} \cdot f_{sw}) \cdot R_{DS(on)\_Q1};$$

$$P_{OSS} = f_{sw} \cdot V_{BUS} \cdot \int_0^{V_{BUS}} C_{OSS}(V_{ds}) \cdot dV_{ds};$$

$$P_{on\_overlap} = f_{sw} \cdot \frac{1}{2} \cdot V_{BUS} \cdot I_{L,turn\_on} \cdot (t_{cr} + t_{vf});$$

$$P_{cond\_Q2} = \left(I_{OUT}^2 + \frac{I_{ripple}^2}{12} \right) \cdot \left(1 - D - t_{dt2} \cdot f_{sw}\right) \cdot R_{DS(on)\_Q2};$$

$$P_{OSS\_sd} = \left[\left(I_{L,turn\_off} \cdot V_{SD1} \cdot t_{SD1}\right) + \left(I_{L,turn\_on} \cdot V_{SD2} \cdot t_{SD2}\right) \right] \cdot f_{sw};$$

$$I_{ripple} = \frac{\left(V_{BUS} - V_{OUT}\right) \cdot D}{f_{sw} \cdot L_{OUT}};$$

$$I_{\text{L,turn\_on}} = I_{\text{OUT}} - \frac{I_{\text{ripple}}}{2};$$

$$I_{\text{L,turn\_off}} = I_{\text{OUT}} + \frac{I_{\text{ripple}}}{2},$$

where V_{BUS} is the input voltage, I_{OUT} is the output current, V_{OUT} is the output voltage, f_{sw} is the switching frequency, L_{OUT} is the throttle inductance, D is the fill factor, $R_{\text{DS(on)\_Q1}}$ is the resistance of transistor Q1 in the open state, $R_{\text{DS(on)\_Q2}}$ is the resistance of transistor Q2 in the open state, $C_{\text{OSS}}(V_{\text{ds}})$ is the dependence of the output capacitance on the resistance of the drain-source, t_{cr} is the time of increase of the drain current of the transistor, t_{vf} is the time of voltage drop of the transistor drain-source, t_{dt1} is the «dead time» before switching on the transistor Q1, t_{dt2} is the «dead time» before switching on transistor Q2, t_{SD1} and t_{SD2} are, respectively, the current flow time through the reverse diode until the opening of transistors Q1 and Q2, V_{SD1} i V_{SD2} are, respectively, the drain-source voltages of transistors Q1 and Q2 in reverse flow mode, I_{ripple} is the maximum value of throttle current, $I_{\text{L,turn\_on}}$, $I_{\text{L,turn\_off}}$ are, respectively, the values of throttle current at the moment of switching on and switching off.

Even an approximate calculation of losses in a half-bridge converter according to the above formulas is quite a time-consuming procedure. To simplify the evaluation of the conversion efficiency, we can use the computer model shown in Fig. 1. To calculate it is enough to set the conversion frequency, supply voltage, output voltage and load resistance. If we know period, it is easy to determine the duration of the control pulses, after determining the fill factor by the formula

$$D = \frac{V_{\text{OUT}}}{V_{\text{BUS}}}.$$

Table 2 shows the value of the efficiency of the GaN module with an LC filter and a load of 8.6 Ω with output voltage of 7.5 V, supply voltage of 12 V for different conversion frequencies. The efficiency of the converter is investigated at frequencies from 50 kHz to 5 MHz using the proposed computer model with element denominations according to the circuit given in the Development Board EPC9031/32/33/34/35 Quick Start Guide. Also for comparison Table 2 shows the efficiency values calculated using the results of measuring the voltage at the output of the power supply and the current consumption of the EPC9035 board.

Table 2

Dependence of converter efficiency on conversion frequency with denominations of elements according to the circuit

Frequency, MHz	0,05	0,5	1	2	3	5
U_{p}, V	11,74	11,73	11,71	11,67	11,62	11,52
$I_{\text{c m}}$, A	0,59	0,6	0,63	0,68	0,75	0,9
η_{calc}	0,94	0,93	0,89	0,82	0,75	0,63
$U_{\text{p mod}}$, V	11,77	11,64	11,44	11,0	10,8	10,48
I_{R13}, A	0,58	0,75	1,0	1,6	1,9	2,33
η_{model}	0,96	0,75	0,57	0,37	0,32	0,27

In Table 2 the following abbreviations are used: U_{p} is the power supply voltage, $I_{\text{c m}}$ is the measured DC power consumption from the power supply, η_{calc} is the efficiency calculated using U_{p} and $I_{\text{c m}}$, $U_{\text{p mod}}$ and I_{R13} are, respectively, the simulated power supply voltage and current through its internal resistance, η_{model} is the efficiency obtained by simulation.

As follows from Table 2, measured and simulated converter efficiencies quite accurately match only at frequency of 50 kHz. As the frequency increases, the difference between them increases. From the simulation results it follows that the current consumption contains the through current of the transistors, which reaches 80 A at the time of switching. The shape and amplitude of the current of transistor Q1 and the voltage at the gates of transistors Q1 and Q2 are shown in Fig. 3.

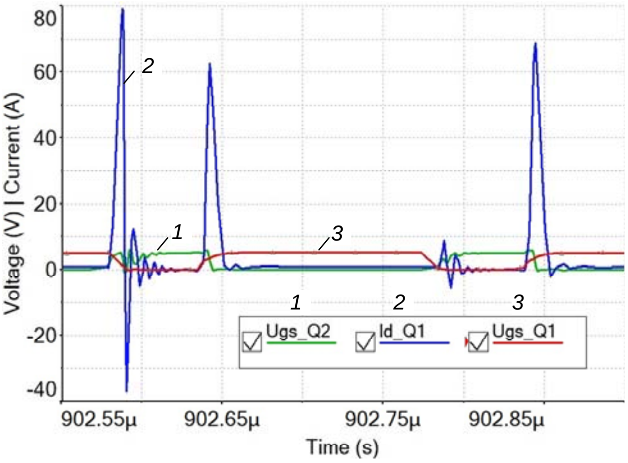

Fig. 3. Simulated control voltage and transistor drain current of the converter

As can be seen from Fig.3, jumps of through current through transistors occur when one of them has not yet closed, and the other has already opened. This current depends on the duration of the «dead time» between the intervals when transistors Q1 and Q2 are open, and the time delays that are set in the SPICE model of the LM5113 driver. The «dead time», in turn, is set by the RC link of the elements R8, C1 for the transistor Q1, and the RC link of the elements R7, C4 for the transistor Q2. Thus, the SPICE model of the LM5113 driver with the manufacturer-specified component denominations does not operate correctly at frequencies above 50 kHz. It is possible to reduce the amplitude of the through current through the transistors extending the duration of the «dead time» by replacing the parameters of the RC links R8C1 and R7C4. Resistors are selected with a value of 100 Ω, and the values of capacitors are doubled to 200 pF. Table 3 shows the results of modelling with a changed duration of «dead time». Also for comparison, the value of efficiency calculated from the results of the experiment is presented.

As can be seen from Table 3, the efficiency of the half-bridge converter on GaN transistors, obtained in the process of modelling η_{model} after changing the parameters of the RC links, almost coincides with the efficiency obtained experimentally η_{calc}. The converter on transistors EPC2022 has the highest efficiency at frequency of 50 kHz and decreases by 0.03-0.04 at frequency of 500 kHz. Thus, it is recommended to choose the operating frequency near this value, because with increasing frequency, the efficiency of the module decreases, and with decreasing frequency, the advantage in speed is lost.

Table 3

Dependence of converter efficiency on conversion frequency with changed denominations of model elements

Frequency, MHz	0,05	0,5	1	2	3	5
$U_{\text{p mod}}$, V	11,79	11,77	11,74	11,7	11,64	11,54
I_{R13}, A	0,56	0,59	0,61	0,67	0,76	0,89
η_{model}	0,98	0,94	0,91	0,83	0,74	0,64
η_{calc}	0,94	0,93	0,89	0,82	0,75	0,63

Evaluation of the EMI of the converter on GaN transistors using the proposed model. An important indicator of the converter is the level of generated EMI. In [8], a study of the EMI level of a boost converter with conversion frequency of 100 kHz is performed, in which Si IGBT IRG4BC30U, cascade GaN NCT8G206N and SiC SCT2120AF transistors in the TO-220 housing are alternately used. As a result, the difference in EMI levels in the frequency range up to 30 MHz is not more than 3 dB, except for one frequency with a frequency response failure, where the difference is 10 dB. Thus, the level of EMI in a given frequency range is more influenced by the conversion frequency, the parameters of the passive elements and the design of the converter, and much less by the type of transistors.

The parameters of the printed circuit board and the design determine the level of the asymmetric component of the interferences due to the parasitic capacitance. It is formed between the power and load wires, the PCB tracks and the «ground». The parasitic capacitance between the output circuits of the converter and the «ground» has the greatest influence on asymmetric interferences.

The parasitic capacitance of the converter board is measured by the method described in [9] using an additional capacitor, which is connected between the output of the converter and «ground». The EMI level is measured with and without an additional capacitor. Then the parasitic capacitance is calculated, which is 1.8–2 pF.

Below are the results of estimating the influence of model parameters on the level of simulated EMI in comparison with the measured ones. Figure 4 shows the levels of interferences for the circuit shown in Fig. 1. Figure 4,*a* shows the EMI with «dead time» according to the documentation, and Fig. 4,*b* – with extended «dead time» (capacitors C2, C4 have capacitance of 200 pF). The simulation is done with an additional capacitor, in order to increase the asymmetric component of the interferences. Capacitor C5 in the circuit has a nominal value of 58 pF (capacitance of the EPC9035 board plus the capacitance of the additional capacitor of 56 pF).

As can be seen from Fig. 4, the difference in the duration of the «dead time» does not have such a significant effect on the level of simulated EMI as on the efficiency. The biggest difference between the simulation results and the experimental ones is observed at frequencies around 30 MHz.

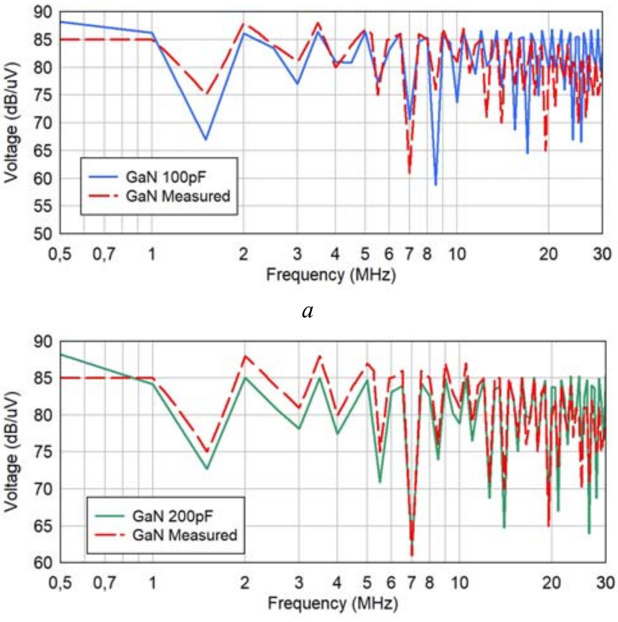

Fig. 4. EMI levels with an additional capacitance of 56 pF, connected to the output of the converters

Description of the test module and test bench. The EPC9035 is mounted on another board, which contains the elements necessary to ensure the correct order of on and off power and control signal supply in accordance with the Instructions for use of the EPC9035 board. It should be noted that the minimum duration of the output pulses provided by the LM5113 driver is 40 ns. This allowed to build on the basis of the EPC9035 board a short pulse generator with voltage of up to 90 V and current of up to 20 A [10].

As part of the test bench (Fig. 5) a selective microvoltmeter SMV11, V-shaped equivalent of the NNB101 network (Line Impedance Stabilization Network – LISN), ammeter and 12 V transformer power supply block with linear voltage stabilizer are used. The assembly of metal-film resistors with total resistance of 8 Ω is connected to the output of the converter by wires of minimum length.

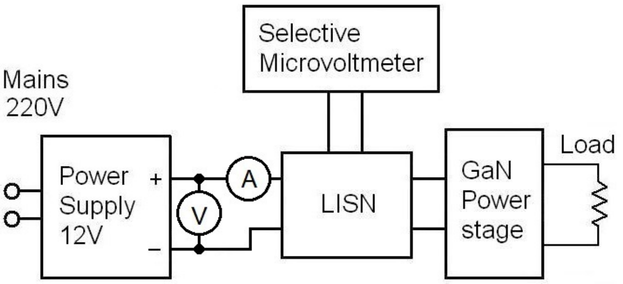

Fig. 5. Diagram of the test bench for measuring current consumption and EMI

Conclusions.

1. As a result of the investigation carried out using the proposed computer model, it is found that the simulation results with parameters taken from the manufacturer's

circuit have a large error (up to 2.3 times) due to inaccurate SPICE model of the GaN transistor driver. Changing the parameters of the RC circuits which form the interval of «dead time» increases the accuracy of determining the current consumption to at least 5 %.

2. The efficiency of the converter on GaN transistors does not practically change up to frequency of 500 kHz, which allows the use of capacitors and throttles of small denominations and dimensions. Then, with increasing conversion frequency, the efficiency decreases.

3. For a converter with additional output capacitance, the parameters of the SPICE model of the driver do not significantly affect the accuracy of modelling of the asymmetric EMI.

4. Thus, due to high output current, high operating voltage and short switching time, GaN transistors are promising for use in pulse generators, power supply blocks with operating conversion frequencies above 500 kHz and in powerful Hi-Fi Class D amplifiers with low required dimensions, such as automotive ones.

5. The disadvantage of GaN transistors is the high cost, several times higher than of silicon MOSFET and IGBT transistors.

REFERENCES

1. Tüysüz A., Bosshard R. Kolar J.W. Performance comparison of a GaN GIT and a Si IGBT for high-speed drive applications. *2014 International Power Electronics Conference (IPEC-Hiroshima 2014 – ECCE ASIA)*, Hiroshima, 2014, pp. 1904-1911. **doi: 10.1109/IPEC.2014.6869845**.

2. Lee D., Soh M.Y., Teo T.H., Yeo K.S. Evaluation of Low Voltage Rectifier Design Using IGBT, MOSFET, and GaN FETs. *TENCON 2018 – 2018 IEEE Region 10 Conference*, Jeju, Korea (South), 2018, pp. 0389-0393. **doi: 10.1109/TENCON.2018.8650321**.

3. Biela J., Schweizer M., Waffler S., Kolar J.W. SiC versus Si–Evaluation of Potentials for Performance Improvement of Inverter and DC–DC Converter Systems by SiC Power Semiconductors. *IEEE Transactions on Industrial Electronics*, 2011, vol. 58, no. 7, pp. 2872-2882. **doi: 10.1109/TIE.2010.2072896.**

4. Han D., Li S., Lee W., Choi W., Sarlioglu B. Trade-off between switching loss and common mode EMI generation of GaN devices-analysis and solution. *2017 IEEE Applied Power Electronics Conference and Exposition (APEC)*, Tampa, FL, 2017, pp. 843-847. **doi: 10.1109/apec.2017.7930794.**

5. Liu X., Costa F., Revol B., Gautier C. EMI investigation in a GaN HEMT power module. *PCIM Europe 2016; International Exhibition and Conference for Power Electronics, Intelligent Motion, Renewable Energy and Energy Management*, Nuremberg, Germany, 2016, pp. 1-8.

6. Gedz O., Lazebnyi V., Onikienko Y., Vlasjuk A. EMI simulation of GaN power stage for audio class D amplifiers. *2018 14th International Conference on Advanced Trends in Radioelecrtronics, Telecommunications and Computer Engineering (TCSET)*, Slavske, 2018, pp. 204-207. **doi: 10.1109/TCSET.2018.8336187.**

7. Lidow A., Strydom J., de Rooij M., Reusch D., Glaser J. *GaN Transistors for Efficient Power Conversion, Third Edition*. New York, John Wiley & Sons, 2020. **doi: 10.1002/9781119594406.**

8. Ibuchi T., Funaki T. A comparative study on conducted noise characteristics of SiC and GaN power transistor. *2016 International Symposium on Electromagnetic Compatibility – EMC EUROPE*, Wroclaw, 2016, pp. 193-198. **doi: 10.1109/emceurope.2016.7739169.**

9. Onikienko Y., Pilinsky V., Rodionova M. Conductive EMI of class D audio amplifiers prediction system. *2015 IEEE 35th International Conference on Electronics and Nanotechnology (ELNANO)*, Kiev, 2015, pp. 437-440. **doi: 10.1109/elnano.2015.7146925.**

10. Onikienko Y., Vlasyuk A., Marchenko O., Popovych P., Filipova N., Shevchenko I. High Frequency Half-Bridge GaN-Based Pulse Generator. *2019 IEEE 39th International Conference on Electronics and Nanotechnology (ELNANO)*, Kyiv, Ukraine, 2019, pp. 700-703. **doi: 10.1109/elnano.2019.8783532.**

Received 14.02.2020

Y.O. Onikienko[1]*, Candidate of Technical Science,*
V.V. Pilinsky[1]*, Candidate of Technical Science, Professor,*
P.V. Popovych[1]*, Candidate of Technical Science,*
V.S. Lazebnyi, Candidate of Technical Science, Associate Professor,
O.I. Smolenska[1]*, Master of Science,*
V.S. Baran[1]*, Master of Science,*
[1] National Technical University of Ukraine «Igor Sikorsky Kyiv Polytechnic Institute»,
37, Prospect Peremohy, Kyiv-56, 03056, Ukraine,
e-mail: yurionik@gmail.com, pww@ukr.net, ppv_ua@ukr.net, s.smolenska.05@gmail.com, vadymbrn@gmail.com

How to cite this article:

Onikienko Y.O., Pilinsky V.V., Popovych P.V., Lazebnyi V.S., Smolenska O.I., Baran V.S. Modelling of operation modes and electromagnetic interferences of GaN-transistor converters. *Electrical engineering & electromechanics*, 2020, no. 3, pp. 37-42. **doi: 10.20998/2074-272X.2020.3.06.**

UDC 621.319 **doi: 10.20998/2074-272X.2020.3.07**

G.V. Bezprozvannych, M.V. Grynyshyna, O.G. Kyessayev, O.M. Grechko

PROVIDING TECHNICAL PARAMETERS OF RESISTIVE CABLES OF THE HEATING FLOOR SYSTEM WITH PRESERVATION OF THERMAL RESISTANCE OF INSULATION

Introduction. The main purpose of resistive cables is to convert the current flowing through the cable into heat. The maximum operating temperature of the conductive core should not exceed 100 °C. Power output per cable per unit length (nominal specific electrical power per 1 m of heating cable at rated line voltage per 1m cable) is the main technical parameter of these cables. The heat released by the conductivity of the core current, taking into account the change in the resistivity of the core material from temperature, is directly proportional to the square of the linear voltage drop across the core, and inversely proportional to the linear resistance of the core. Typical heat dissipation in such cables does not exceed 10 W/m, provided the cable is placed in the air. Purpose. Determination of the specific power of the cable system when varying the thickness of the insulation and the protective polymer shell, provided the thermal stability of the insulation on the basis of thermal balance between the power released in the core and the power released into the environment from the surface of the resistive heating. Methodology. The calculation of the linear heat flux is performed in two steps: when changing the radius of insulation (thickness of insulation) and the constant thickness of the protective polymer shell; at constant thickness of insulation and change of radius of the protective polymer jacket. The highest values of linear heat flux at (70-90) W/m are achieved for the optimum design of a single-conductor resistive cable from a conductive core in the range of 0,4 mm to 1,6 mm when varying the thickness of the cross-linked polyethylene insulation and protective sheath based on polyvinyl chloride plastic. The specific power of heating resistive cables, provided the thermal stability of the crosslinked polyethylene insulation is determined based on the thermal balance between the power generated in the core and the power dissipated from the surface of the cable into the air. Practical value. The thickness of the insulation and the linear voltage of the heating resistive cable, depending on the material of the core, providing thermal stability of the insulation are substantiated. The methodology of substantiation of specific power, which corresponds to thermal stability of heating resistive cables on the basis of thermal balance, can be applied to both the floor heating system and other areas of application of heating cables. References 10, tables 2, figures 4.

Key words: **resistive single conductor heating cable, specific power, linear voltage, thermal stability, polyethylene thermosetting insulation.**

Встановлено діапазон значень лінійного теплового потоку в залежності від розмірів конструктивних елементів резистивного нагрівального кабелю коаксіальної конструкції. На підставі теплового балансу потужностей, що виділяється в струмопровідній жилі та розсіюється з поверхні кабелю, визначено питома потужність нагрівальних резистивних кабелів системи теплої підлоги за умови забезпечення теплової стійкості поліетиленової термореактивної ізоляції. Обґрунтовано товщина ізоляції та лінійна напруга нагрівального резистивного кабелю в залежності від матеріалу струмопровідної жили, що забезпечують теплову стійкість ізоляції. Бібл. 10, табл. 2, рис. 4.

Ключові слова: **резистивний однопровідниковий нагрівальний кабель, питома потужність, лінійна напруга, теплова стійкість, поліетиленова термореактивна ізоляція.**

Установлен диапазон значений линейного теплового потока в зависимости от размеров конструктивных элементов резистивного нагревательного кабеля коаксиальной конструкции. На основании теплового баланса мощностей, выделяемой в токопроводящей жиле и рассеиваемой с поверхности кабеля, определена удельная мощность нагревательных резистивных кабелей системы теплого пола при условии обеспечения тепловой устойчивости полиэтиленовой термореактивной изоляции. Обоснованы толщина изоляции и линейное напряжение нагревательного резистивного кабеля в зависимости от материала токопроводящей жилы, обеспечивающие тепловую устойчивость изоляции. Библ. 10, табл. 2, рис. 4.

Ключевые слова: **резистивный однопроводниковый нагревательный кабель, удельная мощность, линейное напряжение, тепловая устойчивость, полиэтиленовая термореактивная изоляция.**

Introduction. The cable heating floor system is based on cable. The most common are resistive heating cables, which in execution are single-conductor (two-way) and two-conductor (one-way). Single-conductor cables (Table 1) are conductive core (1) with insulation (2) in the metal screen (3) and the protective polymer shell (4). here, the insulation can be either single- or double-layer. The presence of a protective screen is mandatory according to the requirements of the Rules of operation of electrical installations, and at its intersection it must be equivalent to 1.0 mm^2 of copper conductor [1, 2].

The design of such cables is similar to radio frequencies ones intended, for example, for the transmission of television signals. The conductive core is copper, galvanized steel, or high resistance alloys. Polyethylene (thermally reactive insulation) crosslinked by chemical or physical method; organosilicon rubber, heat-resistant polyvinyl chloride plastic are used as insulation [3]. The insulation resistance must be at least 100 TΩ·m. The protective shell is made of polyvinyl chloride plastic or light stabilized polyethylene.

The main purpose of resistive cables is to convert the current flowing through the cable into heat. The maximum operating temperature of the conductive core should not exceed 100 °C [4, 5]. Power output per cable per unit length (nominal specific electrical power per 1 m of heating cable at rated line voltage per 1 m of cable) is the main technical parameter of these cables. Characteristic heat dissipation in such cables does not exceed 10 W/m, provided that the cable is placed in the air (Table 1) [4, 5].

Table 1
Typical characteristics of a single-conductor heating resistive cable for heating floor system

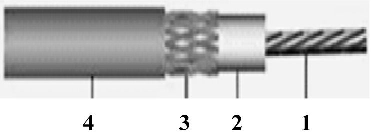	
Parameter	Value
Maximum temperature of the core, °C	100
Maximum allowable temperature without load, °C	100
Maximum linear heat dissipation, W/m	10
Minimum installation temperature, °C	–10
Rated frequency of 50 Hz, V	220
Maximum load current, A	16
Minimum bending radius at operation and storage, mm	150
Minimum allowed radius of single bending, mm	30

Problem definition. The heat P_v released by the current flow along the core, taking into account the change in the resistivity of the conductor material from the temperature [6, 7] $\rho_{gt} = \rho_{T_0} \cdot (1 + \alpha_\rho \cdot (T_g - T_0))$, is directly proportional to the square of the linear drop in the voltage U_p on the core and inversely proportional to the linear resistance $R_{gt} = \dfrac{\rho_{gt}}{\pi \cdot r_1^2}$ of the conductive core with radius r_1

$$P_v = U_p^2 / R_{gt} = \frac{U_p^2}{\rho_{gt}} \cdot \pi \cdot r_1^2 \text{ , [W/m]}, \tag{1}$$

where α_ρ is the temperature coefficient of resistivity ($\alpha_\rho = 0.004$ K^{-1} for copper, $\alpha_\rho = (0.0001\text{–}0.00025)$ K^{-1} for nichrome); T_g, T_0 are the temperature of the conductive core in the heated state due to the flow of the rated current and in the initial state (20 °C), respectively.

In resistive cables, the conductive core has a high internal resistance and, when connected to the mains, is uniformly heated throughout. This property makes it strictly follow the temperature of the operating cable: at deterioration of heat dissipation in a separate area overheat and burn of the cable are possible. Therefore, as a rule, these cables are connected via heating temperature controllers. Fixed cable resistivity imposes a limit on the overall length: reducing it relatively to the recommended values leads to an increase in the specific power, which reduces the durability of the cable. Conversely, increasing the length reduces the specific power and, accordingly, the heating efficiency.

The set of structural features and materials used in the design of cables for heating floor systems must provide a set of electrical, thermal and mechanical characteristics in accordance with the operating conditions at the optimum dimensions.

In [6], the problem of optimizing the power cable of a coaxial structure is formulated to ensure the maximum heat flux dissipated from the cable surface at a fixed thickness of polymer insulation. The target optimization function is the linear density of the heat flux dissipated from the cable surface, depending on the thickness of the protective polymer shell. In low-voltage heating resistive cables, ensuring maximum linear heat flux density is possible by varying both the thickness of the protective polymer shell and the thickness of the insulation. The basic condition for optimizing cable design is to provide thermal insulation resistance, which limits, firstly, the long-term operating temperature of the conductive core, and secondly, the temperature on the cable surface, which must not exceed 60 °C according to the requirements for an electrical cable heating system [2].

Therefore, **the goal of the paper** is to determine the specific power of the cable system when varying the thickness of the insulation and the protective polymer shell, provided the thermal stability of the insulation on the basis of thermal balance between the power released in the conductive core and the power released to the environment surface of resistive heating cable.

A model for determining linear heat flux. The linear heat flux q_l dissipated in the resistive cable of the coaxial structure (Fig. 1) during the flow of rated current through the core is defined as [6]

$$q_l = \frac{\pi \, (T_g - T_{OS})}{R_\Sigma} \text{, [W/m]}, \tag{2}$$

where T_{OS} is the ambient (air) temperature, K; R_Σ is the total thermal resistance of cable elements and the environment, (K·m)/W.

The calculation of the linear heat flux is performed in two stages: the first is at the radius along the insulation $r_{2\text{var}}$ (thickness of insulation) is changed and at the constant thickness of the protective polymer shell; the second one – on the contrary: at a constant thickness of insulation and change of radius $r_{4\text{var}}$ of the protective polymer shell.

In both cases, the total thermal resistance R_Σ [6-10]

$$R_\Sigma = R_2 + R_4 + R_{OS} \,, \tag{3}$$

is a function of the design dimensions of the cable.

The thermal resistances of the conductive metal core and the metal screen are assumed to be zero (the thermal conductivities of metals are 20-100 times greater than the thermal conductivity of insulating materials [7, 9]), that is, $R_1 = R_3 \approx 0$.

Components of thermal resistance: thermal insulation resistance (for the first stage of calculation when changing $r_{2\text{var}}$):

$$R_{2\,\text{var}} = \frac{1}{2\,\pi\,\lambda_2} \cdot \ln\left(\frac{2 r_{2\,\text{var}}}{2 r_1}\right), \tag{4}$$

thermal resistance of the protective polymer shell (for the second stage of calculation when changing $r_{4\text{var}}$):

$$R_{4\,\text{var}} = \frac{1}{2\,\pi\,\lambda_4} \cdot \ln\left(\frac{2 r_{4\,\text{var}}}{2 r_3}\right), \tag{5}$$

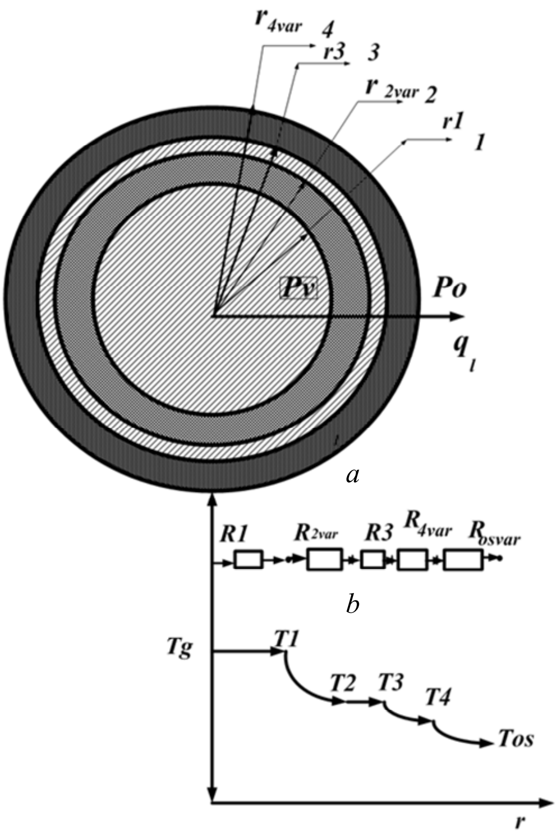

a

b

c

Fig. 1. Typical design (*a*), thermal substitution circuit (*b*) and schematic representation of temperature distribution (*c*) by thickness of resistive coaxial heating cable
(1 – conductive core, 2 – insulation, 3 – metal screen over insulation, 4 – protective polymer shell)

thermal resistance of the environment (air) (in both cases, changing each component of the thermal resistance leads to a change in the cooling surface S_{os} of the cable):

$$R_{os\,\mathrm{var}} = \frac{1}{\alpha_{ef}\cdot S_{os\,\mathrm{var}}}. \qquad (6)$$

In the formulas (4), (5) presented: λ_2, λ_4 are the thermal conductivities of insulation and protective polymer shell, respectively; α_{ef} is the effective coefficient of heat transfer to the environment due to convection and radiation, $2r_1$ is the diameter of the core, $2r_{2\mathrm{var}}$ is the diameter of the insulated wire, $2r_3$ is the diameter of the metal screen, $2r_{4\mathrm{var}}$ is the diameter along the polymeric protective shell.

Figure 2 shows the effect of the thickness of the polyethylene insulation (λ_2 = 0.25 W/(m·K)) and the polyvinyl chloride protective shell (λ_4 = 0.35 W/(m·K)) on the linear heat flux of the resistive heating cable of the coaxial structure. The calculation is made for three diameters of conductive core:

- $2r_1$ = 0.4 mm – curves 1 and 1';
- $2r_1$ = 0.8 mm – curves 2 and 2';
- $2r_1$ = 1.6 mm – curves 3 and 3' when varying the radius of insulation ($r_{2\mathrm{var}}$ / r_1) – curves 1, 2 and 3, and when varying the radius of the polymeric protective shell ($r_{4\mathrm{var}}$ / r_1) – curves 1', 2' and 3', respectively.

The effective heat transfer coefficient is 10 W/(m^2 K). The thickness of the polymer shell is 0.5 mm for curves 1, 2 and 3. Insulation thickness is 0.8; 1.6 and 3.3 mm for curves 1', 2' and 3', respectively.

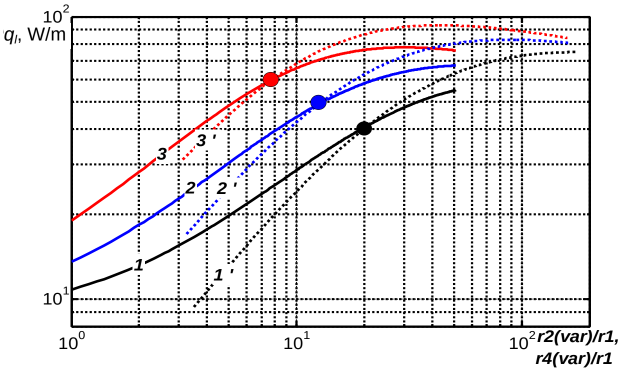

Fig. 2. Determination of expected values of linear heat flux depending on the size of structural elements of a resistive heating cable of a coaxial structure

As the calculation results prove (see Fig. 2), the maximum values of linear heat flux that can be dissipated from the cable surface are in the range of 70 to 90 W/m (curves 1 and 3). Such values correspond to a significant 40-100 times larger diameter along insulation and protective shell relative to the diameter of the conductive core. The values of the linear heat flux in the range (40-50) W/m are provided at smaller ratios of geometric dimensions (shown by points on curves 1, 2, 3 in Fig. 2).

Specific power of heating resistive cables, provided thermal insulation resistance. The value of the linear heat flux in the range (40-50) W/m (Fig. 3, curve 5) is provided by the cable design, conductive core of which is made on the basis of 0.8 mm diameter nichrome, with cross-linked polyethylene insulation 4.8 mm thick and polyvinyl chloride protective shell 0.5 mm thick.

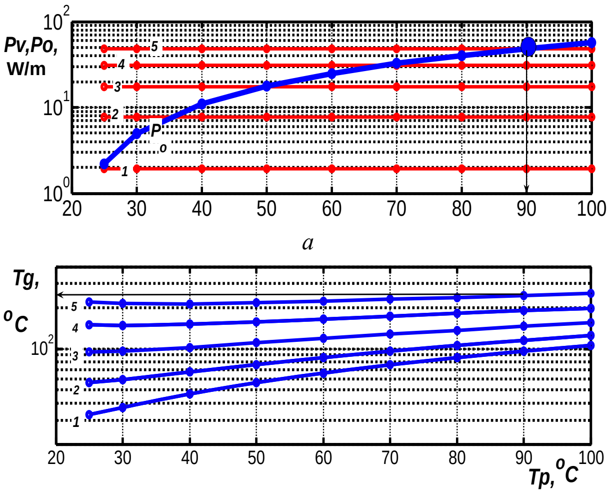

a

b

Fig. 3. On determination of the specific power provided thermal resistance of the insulation of the heating resistive cables
(curve 1 – linear voltage 2 V/m; curve 2 – 4 V/m;
curve 3 – 6 V/m; curve 4 – 8 V/m; curve 5 – 10 V/m)

The total cable diameter is 11.6 mm with aluminum screen thickness of 0.1 mm. Such values are observed at linear voltage of 10 V/m, which corresponds to the thermal balance between the power released in the core P_v and the power dissipated from the surface of the cable P_0 into the air (see Fig. 1,*a*; curve 5 in Fig. 3,*a*).

The temperature on the cable surface (T_p = T_4) is 90 °C, of the conductive core – T_g = 250 °C (curve 5 in Fig. 3,*b*). At these temperatures, the thermal stability of the cross-linked polyethylene insulation is disrupted, which makes it impossible for the heating cable to work in the floor heating system. The cross-linked polyethylene insulation temperature should not exceed 90 °C [3, 9]. The use of more heat-resistant polytetrafluoroethylene or mineral insulation ensures the creation of high-temperature cables for heating oil pipelines and process equipment [5].

Reducing the line voltage to 6 V/m (Fig. 3, curve 3) provides a thermal balance (P_v = P_0) at the level of 18 W/m at a cable surface temperature of 50 °C. In this case, the temperature of the conductive core exceeds the maximum permissible value of 100 °C and is 115 °C (see curve 3 in Fig. 3,*b*).

Reducing the thickness of the insulation to 1 mm ensures a thermal balance at the cable surface temperature 53 °C and the core temperature 86 °C at nominal linear voltage of 4 V/m (Fig. 4,*a*, curve 2). The expected value of the specific power is 8.8 W/m (Fig. 4,*a*, curve 2 in the upper figure).

When using a copper core of the same design, the value of the specific power is 7 W/m (Fig. 4,*b*, curve 2 in the upper figure) at linear voltage of 0.5 V/m. The surface temperature of the cable surface is 47 °C, the temperature of the core is 80 °C (Fig. 4,*b*, curve 2). The cable diameter is 4 mm.

Comparison of two identical by dimensions cable structures with different conductive core material proves that: at supply voltage of 220 V, the length of the cable section with a nichrome core is 55 m with total power of 484 W; the length of copper section cable is 440 m with total power of 3080 W. Eight sections based on the cable with nichrome core total length of 440 m provide power of 3872 W.

When placing the cable directly in the floor (cement-sand mortar), the thermal resistance of the environment [7]

$$R_{OS_t}=\frac{1}{2\pi\lambda_{OS}\cdot L}\ln\left(\frac{h}{d}+\sqrt{\left(\frac{h}{d}\right)^2-1}\right),$$

where λ_{OS} = 0.6 W/(m·K) is the thermal conductivity of cement-sand mortar; L = 1 m is the cable length, d is the cable diameter, h is the depth of cable location.

Table 2 shows a comparative analysis of thermal resistances at the location of the cable in the air and cement-sand mortar at a distance of 50 mm from the floor surface.

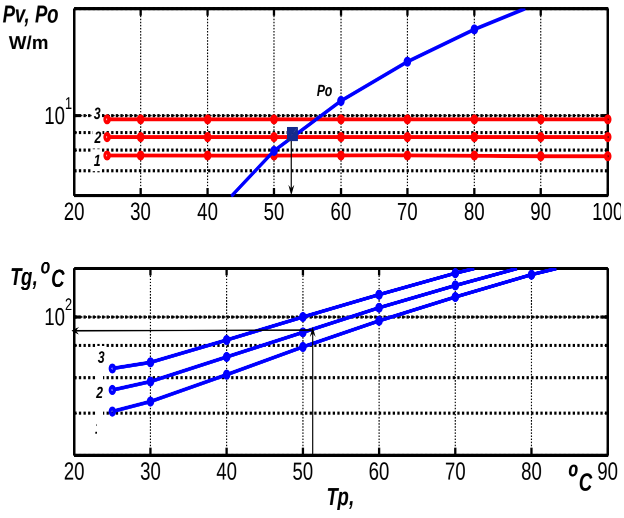

a

curve 1 – linear voltage 3.75 V/m;
curve 2 – 4 V/m; curve 3 – 4.25 V/m

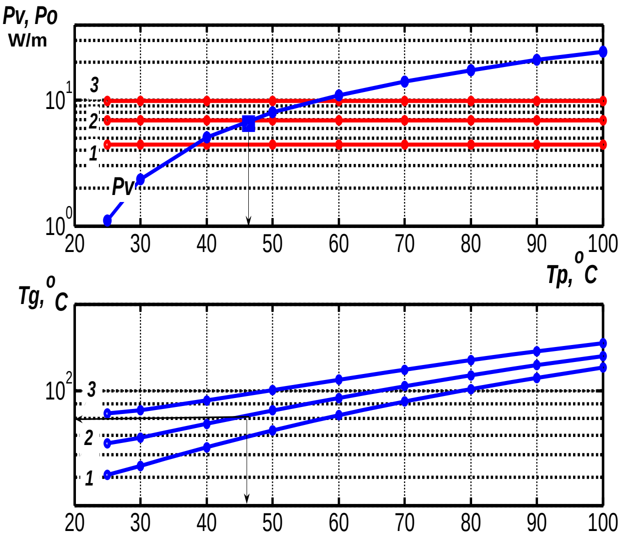

curve 1 – linear voltage 0.4 V/m;
curve 2 – 0.5 V/m; curve 3 – 0.6 V/m

b

Fig. 4. Effect of insulation thickness and line voltage of the heating resistive cable on thermal resistance of the thermosetting polyethylene insulation

Table 2
Impact of the environment surrounding the cable with diameter of 4 mm on the total thermal resistance

Cable thermal resistance: R_2 + R_4, K·m/W	When the cable is placed in the air		When the cable is placed in cement-sand mortar	
	Air thermal resistance: R_{OS}, K·m/W	Total thermal resistance R_Σ, K·m/W	Thermal resistance of the environment surrounding the cable: R_{OS}, K·m/W	Total thermal resistance R_Σ, K·m/W
1.3507	3.2811	4.6318	1.0376	2.3883

The location of the cable in the cement-sand mortar reduces the total resistance by 1.94 times compared to the location in the air, which ensures the effectiveness of the heating resistive cable.

Conclusions.

1. It is established that the highest values of linear heat flux at the level of (70-90) W/m are achieved for the

optimum design of a single-conductor resistive cable with conductive core in the range from 0.4 mm to 1.6 mm when varying the thickness of the cross-linked polyethylene insulation and protective shell based on polyvinyl chloride plastic.

2. Based on the heat balance of the power released in the conductive core and dissipated from the cable surface, the specific power of the heating resistive cables of the floor heating system is determined to ensure the thermal stability of the polyethylene thermosetting insulation. It is proved that for two identical cable designs with different conductive core material, the use of nichrome compared to copper is more efficient: the specific power is greater by 1.26 times, the linear voltage – by 8.5 times, respectively. In both cases, the thermal stability of the cross-linked polyethylene insulation is ensured.

3. The considered technique of substantiation of the specific power, which corresponds to the thermal stability of the heating resistive cables on the basis of thermal balance, can be applied to both the floor heating system and other areas of application of heating cables.

REFERENCES

1. *DNAOP 0.00-1.32-01. Pravyla ulashtuvannia elektroustanovok. Elektroobladnannia spetsialnykh ustanovok* [DNAOP 0.00-1.32-01. Rules of arrangement of electrical installations. Electrical equipment of special installations]. Kyiv, 2001. (Ukr).

2. *DBN V.2.5-24-2012 Elektrychna kabelna systema opalennia* [DBN B.2.5-24-2012. Electric cable heating system]. Kyiv, Minregion of Ukraine Publ., 2012. 83 p. (Ukr).

3. Mikhailin Yu.A. *Teplo-, termo- i ognestoikost' polimernykh materialov* [Heat, thermal and fire resistance of polymeric materials]. St. Petersburg, Scientific Foundations and Technologies Publ., 2011. 416 p. (Rus).

4. *DEVI Cable Systems. Manual*. Kyiv, 2018. 52 p. Available at: https://devi.rv.ua/data/pages/img/63/DEVI_posibnyk_2018.pdf (accessed 20 June 2018). (Ukr).

5. Strupinskii M.L., Khrenkov N.N., Kuvaldin A.B. *Proektirovanie i ekspluatatsiia sistem elektricheskogo obogreva v neftegazovoi otrasli* [Design and operation of electric heating systems in the oil and gas industry]. Moscow, Infra-Inzheneriia Publ., 2015. 272 p. (Rus).

6. Bezprozvannych G.V., Mirchuk I.A. Optimization of design of power ship cables under conditions of cooling in operation. *Bulletin of NTU «KhPI»*, 2019, no. 42 (948), pp. 65-68. (Rus).

7. Bezprozvannych G.V., Naboka B.G. *Matematicheskie modeli i metody rascheta elektroizoliatsionnykh konstruktsii* [Mathematical models and methods of calculation of electrical designs]. Kharkiv, NTU «KhPI» Publ., 2012. 108 p. (Rus).

8. *IEC 60287-2-1: 2001. Electric cables. Calculation of the current rating. Part 2-1: Thermal resistance – Calculation of thermal resistance*. – 84 p.

9. Bezprozvannych G.V., Zolotaryov V.M., Antonets Yu.A. Effect of the thickness of insulation of protected wires of high-voltage overhead transmission lines to their current carrying capacity. *Electrical engineering & electromechanics*, 2018, no. 2, pp. 41-46. **doi: 10.20998/2074-272X.2018.2.07.**

10. Carslaw H.S., Jaeger J.C. *Conduction of heat* ***in*** *solids. Second Ed.* Clarendon Press, London, 2003. 510 p.

Received 21.02.2020

G.V. Bezprozvannych[1]*, Doctor of Technical Science, Professor,*
M.V. Grynyshyna[2]*, Tech. Director,*
O.G. Kyessayev[1]*, Candidate of Technical Science,*
O.M. Grechko[1]*, Candidate of Technical Science, Associate Professor,*
[1] National Technical University «Kharkiv Polytechnic Institute»,
2, Kyrpychova Str., Kharkiv, 61002, Ukraine,
e-mail: bezprozvannych@kpi.kharkov.ua
[2] TOV «Interkabel Kiev»,
5, Dachnaya Str., p. Kapitanovka,
Kiev-Svyatoshinsky district, Kiev region, 08112, Ukraine,
e-mail: m.grynyshyna@interkabel.ua

How to cite this article:
Bezprozvannych G.V., Grynyshyna M.V., Kyessayev O.G., Grechko O.M. Providing technical parameters of resistive cables of the heating floor system with preservation of thermal resistance of insulation. *Electrical engineering & electromechanics*, 2020, no. 3, pp. 43-47. **doi: 10.20998/2074-272X.2020.3.07.**

UDC 621.3 **doi: 10.20998/2074-272X.2020.3.08**

I. Boukhechem, A. Boukadoum, L. Boukelkoul, R. Lebied

SENSORLESS DIRECT POWER CONTROL FOR THREE-PHASE GRID SIDE CONVERTER INTEGRATED INTO WIND TURBINE SYSTEM UNDER DISTURBED GRID VOLTAGES

Wind turbines with permanent magnet synchronous generator (PMSG) are widely used as sources of energy connected to a grid. The studied system is composed of a wind turbine based on PMSG, a bridge rectifier, a boost converter, and a controlled inverter to eliminate low-order harmonics in grid currents under disturbances of grid voltage. Traditionally, the grid side converter is controlled by using the control VFOC (Virtual Flux Oriented Control), which decouple the three-phase currents indirect components (id) and in quadratic (iq) and regulate them separately. However, the VFOC approach is dependent on the parameters of the system. This paper illustrates a new scheme for the grid-connected converter controller. Voltage imbalance and harmonic contents in the three-phase voltage system cause current distortions. Hence, the synchronization with the network is an important feature of controlling the voltage converter. Thus, a robust control method is necessary to maintain the adequate injection of the power during faults and/or a highly distorted grid voltage. The proposed new control strategy is to use the direct power control based virtual flux to eliminate side effects induced by mains disturbances. This control technique lowers remarkably the fluctuations of the active and reactive power and the harmonic distortion rate. The estimated powers used in the proposed control approach is calculated directly by the positive, negative, and harmonic items of the estimated flux and the measured current without line sensor voltage. References 27, tables 6, figures 13.

Key words: **direct power control based virtual flux, disturbances of grid voltage, permanent magnet synchronous generator.**

Ветряные турбины с синхронным генератором на постоянных магнитах (PMSG) широко используются в качестве источников энергии, подключенных к сети. Исследуемая система состоит из ветряной турбины на основе PMSG, мостового выпрямителя, повышающего преобразователя и управляемого инвертора для устранения гармоник низкого порядка в токах сетки при возмущениях напряжения сети. Традиционно преобразователь на стороне сети управляется с помощью виртуального потокоориентированного управления VFOC (Virtual Flux Oriented Control), который разделяет трехфазные токи на косвенные компоненты (id) и на квадратичные компоннеты (iq) и регулирует их отдельно. Однако подход VFOC зависит от параметров системы. Данная статья иллюстрирует новую схему для контроллера преобразователя, подключенного к сети. Дисбаланс напряжения и содержание гармоник в трехфазной системе напряжения вызывают искажения тока. Следовательно, синхронизация с сетью является важной особенностью управления преобразователем напряжения. Таким образом, надежный метод управления необходим для поддержания адекватной подачи энергии во время неисправностей и/или значительно искаженного напряжения сети. Предложенная новая стратегия управления заключается в использовании виртуального потока на основе прямого управления мощностью для устранения побочных эффектов, вызванных помехами в сети. Этот метод управления значительно снижает колебания активной и реактивной мощности и уровень гармонических искажений. Оценочные мощности, используемые в предлагаемом подходе к управлению, рассчитываются непосредственно по положительным, отрицательным и гармоническим элементам оцененного потока и измеренного тока без напряжения линейного датчика. Библ. 27, табл. 6, рис. 13.

Ключевые слова: **виртуальный поток на основе прямого управления мощностью, возмущения напряжения сети, синхронный генератор с постоянными магнитами.**

Introduction. Renewable sources connected to a grid with their inherent intermittent behavior inevitably impose a major challenge to the conception of the controller voltage source converter. The majority of control approaches have equivocal statements according to their performance under conditions of non-ideal voltage grid prevailing in an integrated micro-grid system with renewable energy. Renewable energy production has become a significant development trend for contemporary grids because of environmental concerns. Wind energy is one of the important sources of renewable energy and is a fast-growing technology [1, 2]. There are two types of wind energy systems: the grid-connected system and the stand-alone wind system. Actually, the application of grid-connected is largely preferred to stand-alone wind systems. The most common configuration for MWT systems connected to the grid of less than 20 kW normally consists of a high-pole-pair PMSG supplying a three-phase rectifier followed by a boost converter and an inverter [3]. At the generator terminals, a diode bridge rectifier can be used since no external excitation current is required. The non-controlled rectifier with a boost converter or supercharged converter serves to regulate the rotor voltage or speed. The interfaces between renewable energy sources and a grid-side have played a crucial role in terms of reliability, the flexibility of connection, and quality of energy and gradually attracted attention from the academic and the industrial worlds these last years. These interfaces can regulate the powers with a constant power factor or constant currents. Various studies of these electronic power interfaces and control methodologies have been largely realized, including the development of schemas of switching to improve the quality of the energy [4]. Traditionally, the grid side converter is controlled by using the control VFOC (Virtual Flux Oriented Control) [5] or VOC [6], which decouple the three-phase currents in Direct components (id) and in quadratic (iq) and regulate them separately. A reference frame aligned with the rotary vectors voltage or virtual flux [7]. However, the VFOC or VOC approaches are dependent on the parameters of the system and various simplifying approximations are made; for instance, the magnetic saturation of the inductor is not considered that is, the inductor is constant whatever of the current values [8]. The three-phase rectifier control approaches in width of impulse can be classified, as quoted in the literature, as vector control (VOC) and direct power control (DPC) [16]. The vector control (VC) can be based on grid side voltage [17-19] or virtual flux (VF) [20] using integral proportional controllers (PI). However, it offers some disadvantages, such as its addiction to the variation of system parameters, and that its performance largely depends on the agreement of the PI parameters. The direct power control strategy (DPC) has become one of the most recent research topics in recent years relying on its fast dynamic response, its a simple structure, and its high power factor [21, 22]. In DPC schemes developed, instant active and reactive powers are directly controlled [24]. This is what we need more than sensors (voltage sensors and AC mains sensors) that not only raises the volume and cost of the system but also lowers the reliability of the system [22]. The grid-connected three-phase rectifier can be seen as a virtual AC motor, its virtual flux link can be used to estimate the voltage of the rectifier [26]. Virtual flux (VF) based schematics are popular in voltage-free controller designs for the following two reasons. The application of VF remains the common benefits of sensorless strategies, such as cost reduction, reliability, and overall improvement. During this time, it eliminates the orientation point limitation for the control system [25] and improves the harmonic tolerance [26]. A more complete comparative study is conducted to evaluate the performance of the system in different grid voltage conditions where the voltage unbalances vary by up to 20 % and the distortion varies by 10 %. The global magnitude of total harmonic distortion (THD) presented by VF-DPC and the resilient direct power control RV-DPC is always inferior to that of V-DPC [15]. The V-DPC possesses a low immunity to asymmetric and deformed voltage; the VF-DPC shows a better reliability only under distorted grid voltage [15] a new method of VF-DPC control based on the virtual flux estimate Capable of handling these problems; it results in a stable and regular estimated virtual flux with a sectorial detection at a high precision [23].

The aim of this article is to inject all the power provided by a wind turbine based on the PMSG is a three-phase microgrid subjected to various voltage conditions. This document also seeks to propose a new strategy by integrating new theory, Direct Power Control, based on the virtual flux (VF_DPC) to ensure that the injected currents in the three-phase grid emulate the sinusoidal forms even when the grid voltage is no longer ideal.

Modeling Of The Wind Conversion. In the suggested system of energy, the PMSG is plugged to the grid through an inverter assisted by a rectifier bridge and a boost converter (Fig. 1). The rectifier consisted of diodes that convert the AC output voltage from PMSG to a DC voltage. The boost converter increases the output rectifier voltage at a regulated DC level. The boost converter regulates the speed of the generator or the active power of the generator to capture the maximum power of available wind energy. The grid-side converter (GSC) is then utilized to control the DC link voltage and transfer all the active power provided by the turbine to the grid.

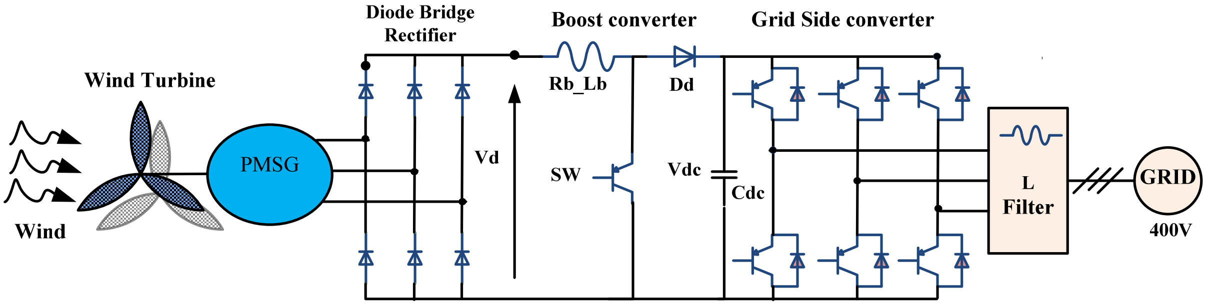

Fig. 1. The system under study comprising PMSG assisted with diode rectifier and boost converter

Wind Turbine Modeling. The wind turbine is three-dimensional, with complex shapes in movement, inundated in a stream air; it changes over the wind's motor vitality and conveys mechanical force portrayed by a rotating speed and mechanical torque. The dynamic force accessible to the turbine is given by:

$$P_\omega = \frac{1}{2}\rho S V_\omega^3 = \frac{1}{2}\rho \pi R^2 V_\omega^3, \qquad (1)$$

where ρ is density of air (1.25 kg/m^3), S is area swept by the turbine (m^2), R is turbine radius (m), V_ω is wind speed (m/s).

Aerodynamic shaft power is given by:

$$P_{turb} = C_p P_\omega = \frac{1}{2}\rho \pi R^2 V_\omega^3 C_p(\lambda, \beta), \qquad (2)$$

where C_p is the power coefficient which is a function of the pitch angle of rotor blades and of the tip speed ratio; β is orientation angle of the blades; λ is specific speed

$$\lambda = \frac{\omega_{turb} R}{V_\omega}, \qquad (3)$$

where ω_{turb} is speed of the turbine.

Modeling of PMSG. The model of PMSG in d−q transformation is given by the accompanying voltage framework condition

$$\begin{aligned} V_d &= -R_s I_d - L_d \frac{d}{dt} I_d + \omega L_q I_q; \\ V_q &= -R_s I_q - L_q \frac{d}{dt} I_q + \omega L_d I_d + \omega \varphi_f. \end{aligned} \qquad (4)$$

The electromagnetic coupling

$$\begin{cases} \varphi_d = L_d i_d + \varphi_f; \\ \varphi_q = L_q i_q, \end{cases} \qquad (5)$$

where L_d is stator inductance in d-axis, L_q is stator inductance in q-axis, L_q and L_d are supposed independent of θ, φ_f is magnet flux.

Equation (6) represent the expression of electromagnetic torque:

$$\begin{aligned} V_d &= -R_s I_d - C_{em} = \\ &= \frac{3}{2} p\left[\left(L_d - L_q\right) i_d i_q + i_q \varphi_f\right] L_d \frac{d}{dt} I_d + \omega L_q I_q; \\ V_q &= -R_s I_q - L_q \frac{d}{dt} I_q + \omega L_d I_d + \omega \varphi_f, \end{aligned} \qquad (6)$$

in which $C_{em} = 3/2 \cdot p \cdot \varphi_f \cdot I_q$, where p is the pole pair number; R_s is stator resistance; V_d and V_q are stator voltage components; I_d and I_q are stator current components.

Control Of Boost Converter. At the output of certain renewable sources (such as wind systems) in general, the voltage generated is not enough to ensure the proper functioning of the inverter. For this, a DC/DC boost converter must be used, built with electronic semiconductor devices, an inductor and a capacitor in parallel [12]. The wind generator is tied to a boost converter, and its input voltage is controlled so that the wind generator delivers the maximum power to its output terminals. The boost converter is connected between the output terminals of the non-controlled rectifier and the input of the inverter, as shown in Fig. 2.

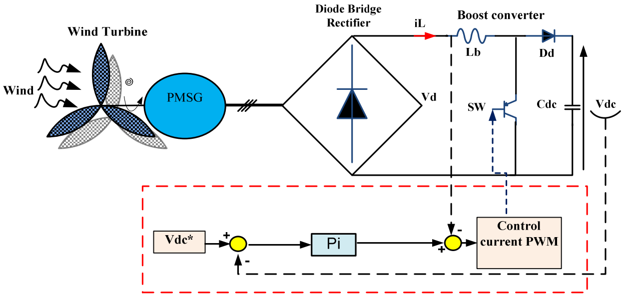

Fig. 2. Structure and principle control of an AC / DC converter

The essential role of the boost converter is to convert the variable input DC voltage, due to different operating conditions, to a suitable constant DC voltage. The DC link voltage can be maintained constant at the reference value by adjusting the duty cycle of the converter. In doing so, the DC voltage is controlled to sufficient and non-fluctuating levels so that maximum power is injected under better conditions through the grid side inverter. The control framework of the DC-DC boost converter is founded on the use of the PI controller to keep the DC link voltage at the reference value as shown in Fig. 2. The voltage/current input/output relationship of the boost converter can be written as [13].

Direct Power Control Based On Virtual Flux (VF_DPC). In this situation, the direct power control based on the virtual flux (DPC-VF) is used instead of the direct power control (DPC). This control technique greatly lowers the fluctuations of the active and reactive power and the harmonic distortion rate THD, keeping the advantage of control without the line voltage sensor. In the VF concept, the virtual AC motor is assumed from the behavior of grid voltages and AC side coupling impedance with inductance L in series with equivalent resistance R. As a result, L and R are analogous to the leakage inductance and the stator resistance of an AC motor, respectively [26]. The control of the active (P_{ref}) and reactive (Q_{ref}) power are compared with the estimated active and reactive power values (P_{es} and Q_{es}) by hysteresis controllers, respectively. The output digitized signals (SP) and (SQ) and the vector position (θ_φ) make it possible to select the appropriate voltage vector according to the switching table defined in [24].

Figure 3 shows the maximum power point tracking (MPPT) control charts for the optimal torque control method respectively. The torque reference multiplied by the speed of the turbine (ωt) gives the optimal power reference. As shown in Fig. 3, the maximum power of the wind turbine is calculated from the equation [$P_{ref}^* = T_{ref}^* \cdot \omega t$] which represents the power reference injected into the grid.

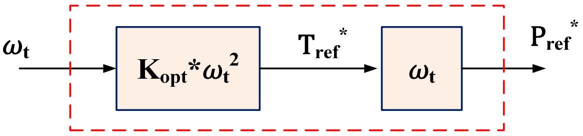

Fig. 3. Block diagram of MPPT Optimal torque control

Model of Grid Side Converter. The vector of virtual flux $\varphi_{\alpha\beta}$ can be estimated from the integration of the vector of grid voltages $e_{\alpha\beta}$ as indicated follow in equation (8).

The voltages of the converter (Fig. 4) are estimated in the block ais follows

$$\begin{cases} V_{s\alpha} = \sqrt{\dfrac{2}{3}} V_{dc} \times \left(S_a - \left(S_b + S_c\right)\right); \\ V_{s\beta} = \sqrt{\dfrac{1}{2}} V_{dc} \times \left(S_b - S_c\right), \end{cases} \qquad (7)$$

where S_a, S_b, and S_c are the switching states of the rectifier and ($V_{s\alpha}$, $V_{s\beta}$) are the AC side voltages of the converter. V_{dc} is rectified voltage.

The components of the virtual flux φ_s are calculated as follows:

$$\begin{cases} \varphi_{s\alpha} = \int (V_{s\alpha} + L \dfrac{di_\alpha}{dt}) dt; \\ \varphi_{s\beta} = \int (V_{s\beta} + L \dfrac{di_\beta}{dt}) dt, \end{cases} \qquad (8)$$

where $V_{s(\alpha\beta)}$ is the voltage at the output of the inverter at the α, β mark; i_α and i_β are grid currents in the Concordia.

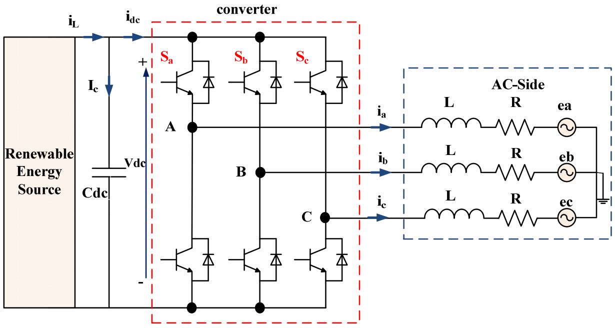

Fig. 4. Simplified representation of a three-phase PWM inverter

The virtual flux concept has been developed for a better estimate of instantaneous active and reactive power in AC-free sensor operation. The use of an ideal integrator for computing the virtual flux produces a DC offset. According to (7) and (8) the integrator can be used to estimate the virtual flux, but the initial value of the flux has to be estimated first, this complicates the simulation and the DC offset could be produced easily [14]. The virtual line stream observer (Fig. 5) shows that the new algorithm responds faster than traditional control.

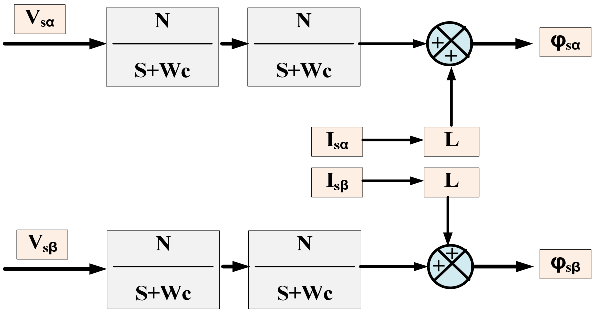

Fig. 5. The virtual line flux linkage observer

The active and instantaneous reactive powers are observed in the (power observer block) by the measurement of the line current and the observation of the virtual flux components in equation [9]. Instant active and reactive powers can be estimated as

$$\begin{cases} P_{es} = \omega(\varphi_{s\alpha} \times i_{s\beta} - \varphi_{s\beta} \times i_{s\alpha}); \\ Q_{es} = \omega(\varphi_{s\alpha} \times i_{s\alpha} + \varphi_{s\beta} \times i_{s\beta}). \end{cases} \tag{9}$$

There is a change in the sector. These sectors may be expressed as follows (Fig. 6)

$$(N-5)\frac{\pi}{6} \prec \theta_N \prec (N-4)\frac{\pi}{6}.$$

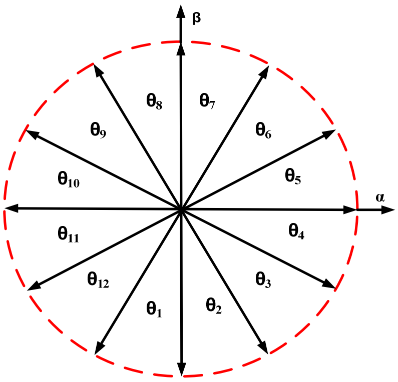

Fig. 6. Virtual flux plane 12 sectors

The position of the VF vector

$$\theta_N = \tan^{-1}\left(\frac{\varphi_{s\beta}}{\varphi_{s\alpha}}\right)$$

is used in the VF-DPC scheme to select the appropriate converter voltage vector according to the switch table defined in Table 1.

Table 1

Switching Table

S_p	S_q	θ1	θ2	θ3	θ4	θ5	θ6	θ7	θ8	θ9	θ10	θ11	θ12
1	0	V_5	V_6	V_6	V_1	V_1	V_2	V_2	V_3	V_3	V_4	V_4	V_5
	1	V_3	V_4	V_4	V_5	V_5	V_6	V_6	V_1	V_1	V_2	V_2	V_3
0	0	V_6	V_1	V_1	V_2	V_2	V_3	V_3	V_4	V_4	V_5	V_5	V_6
	1	V_1	V_2	V_2	V_3	V_3	V_4	V_4	V_5	V_5	V_6	V_6	V_1

Modified Direct Power Control (M DPC) for Converter. When the grid is unbalanced and harmonized, according to the theory of symmetrical decomposition, an unbalanced and distorted three-phase system can be decomposed into three symmetrical components: the positive sequence, the negative sequence, and the zero sequence.

In fixed reference systems the flux and the measured current are expressed as

$$\begin{cases} \varphi_{s\alpha} = \left(\varphi_{s\alpha}^{+} + \varphi_{s\alpha}^{-} + \varphi_{s\alpha}^{h}\right); \\ \varphi_{s\beta} = \left(\varphi_{s\beta}^{+} + \varphi_{s\beta}^{-} + \varphi_{s\beta}^{h}\right). \end{cases} \tag{10}$$

$$\begin{cases} i_{s\alpha} = \left(i_{s\alpha}^{+} + i_{s\alpha}^{-} + i_{s\alpha}^{h}\right); \\ i_{s\beta} = \left(i_{s\beta}^{+} + i_{s\beta}^{-} + i_{s\beta}^{h}\right). \end{cases} \tag{11}$$

According to the theory of symmetric decomposition:

$$\begin{bmatrix} X^{+} \\ X^{-} \end{bmatrix} = \frac{1}{3}\begin{bmatrix} 1 & a & a^2 \\ 1 & a^2 & a \end{bmatrix}\begin{bmatrix} X_a \\ X_b \\ X_c \end{bmatrix}, \tag{12}$$

here the indices (+) and (–) indicate the positive sequence and the negative sequence, $a = e^{j\left(\frac{2\pi}{3}\right)}$, the zero sequence is $X^h = X - X^{+} - X^{-}$.

After substituting the flux and the current by their values indicated in (10) and (11), the results of the active and reactive powers can be grouped as follows

$$P_{es} = \omega \times \begin{bmatrix} \left(\varphi_{s\alpha}^{+} + \varphi_{s\alpha}^{-} + \varphi_{s\alpha}^{h}\right) \times \left(i_{s\beta}^{+} + i_{s\beta}^{-} + i_{s\beta}^{h}\right) - \\ -\left(\varphi_{s\beta}^{+} + \varphi_{s\beta}^{-} + \varphi_{s\beta}^{h}\right) \times \left(i_{s\alpha}^{+} + i_{s\alpha}^{-} + i_{s\alpha}^{h}\right) \end{bmatrix};$$

$$P_{es} = \omega \times \begin{bmatrix} \left(\varphi_{s\alpha}^{+} \times i_{s\beta}^{+} - \varphi_{s\beta}^{+} \times i_{s\alpha}^{+}\right) + \left(\varphi_{s\alpha}^{-} \times i_{s\beta}^{-} - \varphi_{s\beta}^{-} \times i_{s\alpha}^{-}\right) + \\ + \left(\varphi_{s\alpha}^{h} \times i_{s\beta}^{h} - \varphi_{s\beta}^{h} \times i_{s\alpha}^{h}\right) + \left(\varphi_{s\alpha}^{+} \times i_{s\beta}^{-} - \varphi_{s\beta}^{+} \times i_{s\alpha}^{-}\right) + \\ + \left(\varphi_{s\alpha}^{+} \times i_{s\beta}^{h} - \varphi_{s\beta}^{+} \times i_{s\alpha}^{h}\right) + \left(\varphi_{s\alpha}^{-} \times i_{s\beta}^{+} - \varphi_{s\beta}^{-} \times i_{s\alpha}^{+}\right) + \\ + \left(\varphi_{s\alpha}^{-} \times i_{s\beta}^{h} - \varphi_{s\beta}^{-} \times i_{s\alpha}^{h}\right) + \left(\varphi_{s\alpha}^{h} \times i_{s\beta}^{+} - \varphi_{s\beta}^{h} \times i_{s\alpha}^{+}\right) + \\ + \left(\varphi_{s\alpha}^{h} \times i_{s\beta}^{-} - \varphi_{s\beta}^{h} \times i_{s\alpha}^{-}\right) \end{bmatrix}; \tag{13}$$

$$Q_{es} = \omega \times \begin{bmatrix} \left(\varphi_{s\alpha}^{+} + \varphi_{s\alpha}^{-} + \varphi_{s\alpha}^{h}\right) \times \left(i_{s\alpha}^{+} + i_{s\alpha}^{-} + i_{s\alpha}^{h}\right) + \\ + \left(\varphi_{s\beta}^{+} + \varphi_{s\beta}^{-} + \varphi_{s\beta}^{h}\right) \times \left(i_{s\beta}^{+} + i_{s\beta}^{-} + i_{s\beta}^{h}\right) \end{bmatrix};$$

$$Q_{es} = \omega \times \begin{bmatrix} \left(\varphi_{s\alpha}^{+} \times i_{s\alpha}^{+} + \varphi_{s\beta}^{+} \times i_{s\beta}^{+}\right) + \left(\varphi_{s\alpha}^{-} \times i_{s\alpha}^{-} + \varphi_{s\beta}^{-} \times i_{s\beta}^{-}\right) + \\ + \left(\varphi_{s\alpha}^{h} \times i_{s\alpha}^{h} + \varphi_{s\beta}^{h} \times i_{s\beta}^{h}\right) + \left(\varphi_{s\alpha}^{+} \times i_{s\alpha}^{-} + \varphi_{s\beta}^{+} \times i_{s\beta}^{-}\right) + \\ + \left(\varphi_{s\alpha}^{+} \times i_{s\alpha}^{h} + \varphi_{s\beta}^{+} \times i_{s\beta}^{h}\right) + \left(\varphi_{s\alpha}^{-} \times i_{s\alpha}^{+} + \varphi_{s\beta}^{-} \times i_{s\beta}^{+}\right) + \\ + \left(\varphi_{s\alpha}^{-} \times i_{s\alpha}^{h} + \varphi_{s\beta}^{-} \times i_{s\beta}^{h}\right) + \left(\varphi_{s\alpha}^{h} \times i_{s\alpha}^{+} + \varphi_{s\beta}^{h} \times i_{s\beta}^{+}\right) + \\ + \left(\varphi_{s\alpha}^{h} \times i_{s\alpha}^{-} + \varphi_{s\beta}^{h} \times i_{s\beta}^{-}\right) \end{bmatrix}. \tag{14}$$

The target control of the DPC strategy is to eliminate the negative and harmonic components of the current, so we can force

$$i_{s\alpha}^{-} = i_{s\beta}^{-} = i_{s\alpha}^{h} = i_{s\beta}^{h} = 0. \tag{15}$$

Leading to

$$P_{neg} = \omega \times \left[\left(\varphi^{-}_{s\alpha} \times i^{+}_{s\beta} - \varphi^{-}_{s\beta} \times i^{+}_{s\alpha}\right)\right];$$
$$Q_{neg} = \omega \times \left[\left(\varphi^{-}_{s\alpha} \times i^{+}_{s\alpha} + \varphi^{-}_{s\beta} \times i^{+}_{s\beta}\right)\right], \qquad (16)$$

where P_{neg} and Q_{neg} represent the interaction between the negative sequence and the positive sequence of flux and currents that generate oscillation in active and reactive power with a frequency of 2ω.

So we have

$$P_{har} = \omega \times \left[\left(\varphi^{h}_{s\alpha} \times i^{+}_{s\beta} - \varphi^{h}_{s\beta} \times i^{+}_{s\alpha}\right)\right];$$
$$Q_{har} = \omega \times \left[\left(\varphi^{h}_{s\alpha} \times i^{+}_{s\alpha} + \varphi^{h}_{s\beta} \times i^{+}_{s\beta}\right)\right], \qquad (17)$$

where P_{har} and Q_{har} represent the interaction between the harmonic parts of the flux and the positive sequence of the currents.

It can be seen from equations [16, 17] that if we want to eliminate the effect of the negative and harmonic components of the unbalanced and deformed grid, the active and reactive power of compensation can be obtained as

$$P_{com} = \omega \times \left[\left(\varphi^{-}_{s\alpha} \times i^{+}_{s\beta} - \varphi^{-}_{s\beta} \times i^{+}_{s\alpha}\right) + \left(\varphi^{h}_{s\alpha} \times i^{+}_{s\beta} - \varphi^{h}_{s\beta} \times i^{+}_{s\alpha}\right)\right];$$
$$Q_{com} = \omega \times \left[\left(\varphi^{-}_{s\alpha} \times i^{+}_{s\alpha} + \varphi^{-}_{s\beta} \times i^{+}_{s\beta}\right) + \left(\varphi^{h}_{s\alpha} \times i^{+}_{s\alpha} + \varphi^{h}_{s\beta} \times i^{+}_{s\beta}\right)\right]. \qquad (18)$$

Figure 7 shows the overall configuration of the direct power control without a voltage sensor based on the virtual flux.

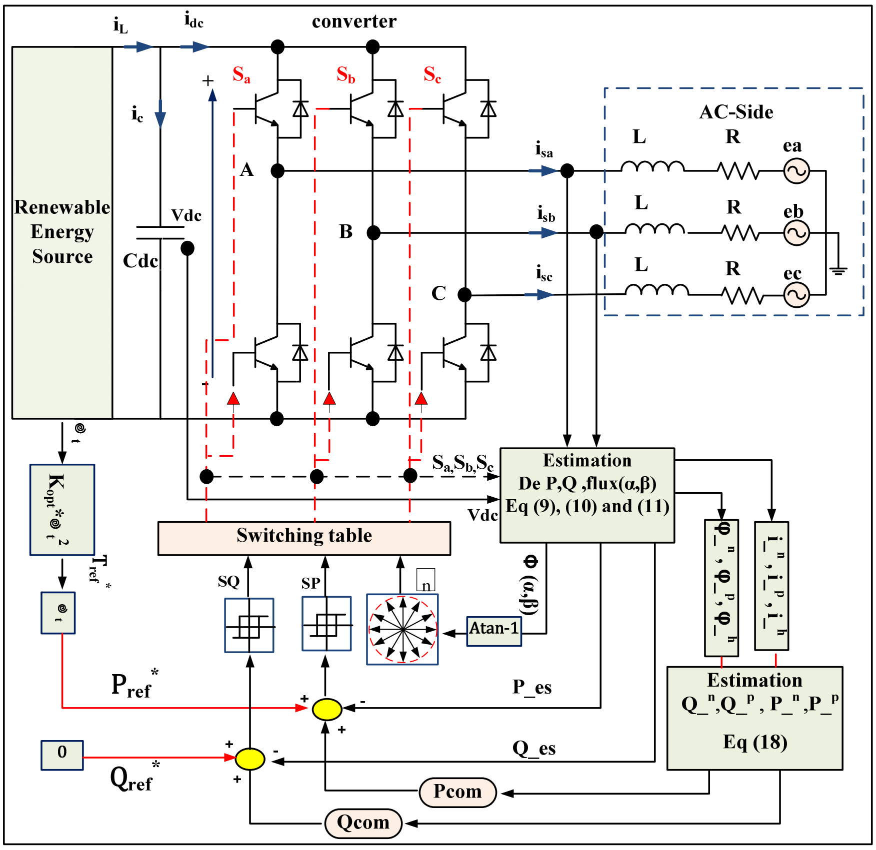

Fig. 7. Control block diagram of the grid-side converter

Simulation Results. In order to verify the performance of the optimal VF-DPC proposed on a two-level voltage source inverter, simulation studies were performed in the Matlab/Simulink environment under various grid voltage conditions. All the results are obtained at the maximum power of the wind turbine P_{ref}^{*}[W] and Q_{ref}^{*} of 0 [VAR].

The simulation model is developed from a Kollmorgen 6 kW industrial permanent magnet synchronous machine [27]. The values of the turbine and the PMSG used parameters are given in Appendix in Table A.1 and Table A.2. The converter power and its monitoring algorithm are also implemented and included in the model. The sampling time used for the simulation is $2 \cdot 10^{-5}$ s.

Test 1. Maximum Power Generation injected. In this test, the purpose of the algorithm is to follow the maximum power of the system. Fig. 8 and 9 show several results obtained.

Figure 8 shows the system response for a gradual change in wind speed from 9 m/s to 7.5 m/s to 8 m/s then back to 9.5 m/s. It can be seen in Fig. 8,*d* that the electromagnetic torque of the generator T_g also follows the reference torque of the turbine T_m. Figures 8,*c* and 8,*e* show that the voltage of the PMSG varies with wind speed as well as the DC voltage at the output of the rectifier. Figure 8,*f* shows that the current is controlled according to the MPPT strategy and can be better regulated to reach the optimum current. Figure 8,*g* illustrates that the DC capacitor voltage (V_{dc}) reaches its reference quickly to 700 V using the proposed power factor correction controller (PFC). The PFC attests its capability to give a fast response time and to pursue the reference voltage regardless of the variation in wind speed.

Figure 9 shows the performance of the converter with a balanced and free-harmonic voltage (Fig. 9,*a* and 9,*b*). Figure 9,*c* and 9,*d* exhibit that the injected current in the range is controlled to be sinusoidal and balanced. Figure 9,*g* and 9,*h* indicate that the estimated active and reactive powers are identical to the measured power.

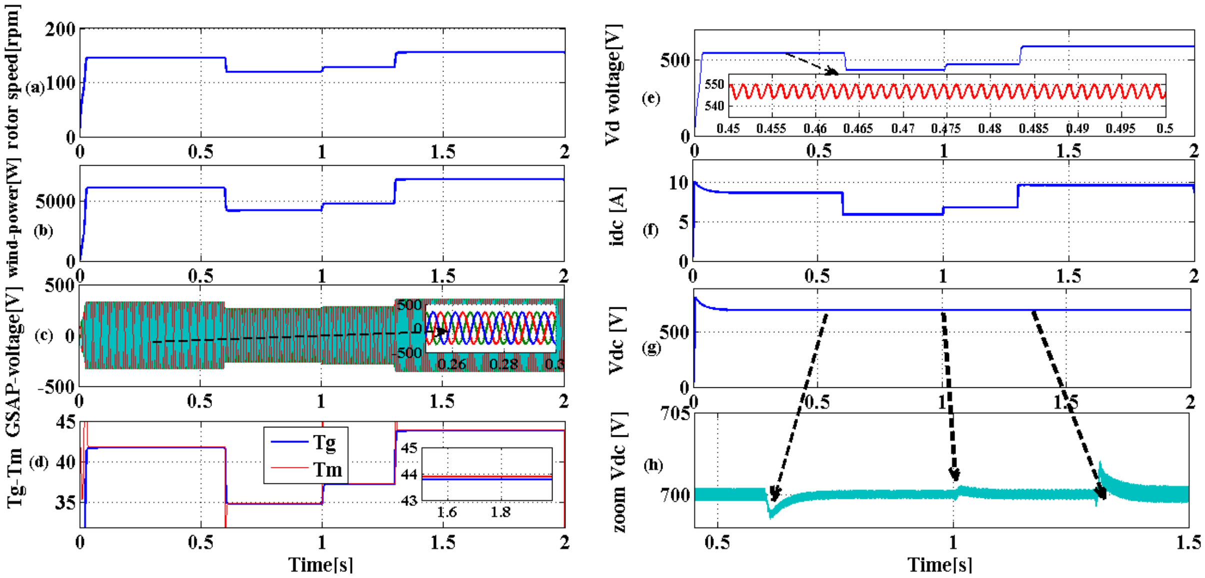

Fig. 8. System response for a change of wind speed at 9 m/s to 7.5 m/s to 8 m/s to 9.5 m /s:
(*a*) rotor speed; (*b*) output power; (*c*) voltage generator; (*d*) torque reference and generator electromagnetic torque;
(*e*) output voltage rectifier; (*f*) current boost converter; (*g*) voltage boost converter; (*h*) zoom of voltage boost converter

This indicates that the applied virtual flux DPC has high performance. The injected currents rise and drop according to the variation of the wind speed and thus the power. It can easily be shown that the dynamic response for a brusque change in the speed level is preferable for the proposed system.

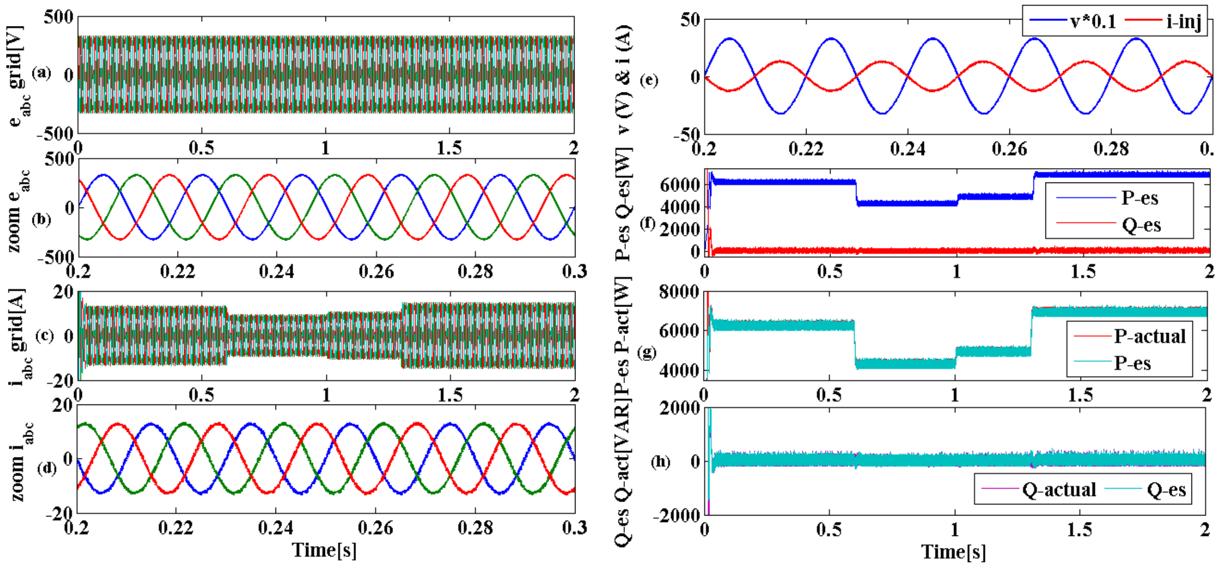

Fig. 9. Performance of the VF_DPC in a balanced and non-distorted grid during different periods of wind variation:
(*a*) grid voltage; (*b*) zoom grid voltage; (*c*) grid current injected; (*d*) zoom grid current; (*e*) current injected with the grid voltage;
(*f*) the estimated active and reactive power; (*g*) the active power estimated at the measured power;
(*h*) the reactive power estimated at the measured reactive power

Test 2. Simulated Transient Responses in Various Grid Voltage Conditions.

1. Without Compensation. In order to check the implementation of the VF_DPC on a two-level voltage source inverter, simulations were performed under various grid voltage conditions. Four grid voltage states are applied. Initially, the main voltages are balanced and sinusoidal, afterward, a voltage unbalance of 30 % is created. secondly, the amplitude of each phase voltage is restored. But, the 5th and 7th harmonics with an amplitude of 20 % are added to the fundamental. Hence, the grid voltages are balanced but distorted. Finally, the worst case of grid voltages, both unbalanced and distorted of 20 % and harmonic 7th of 20 %, is also included in the last condition. The curves in Fig. 10 are three-phase mains voltages, three-phase mains currents, active and reactive power. For further justification, comprehensive quantitative analyses were performed for grid voltages with a defined range of rate and distortion imbalance. To guarantee the normal operation of the system, the European Standard (EN 50160) recommends that the worst case for limiting THD voltage should hold at most 8 %; the permissible variation of the supply voltage should not exceed ±10 % [14]. However, the IEEE Standard 519 recommends a THD voltage limit of 5 % [15] for general applications.

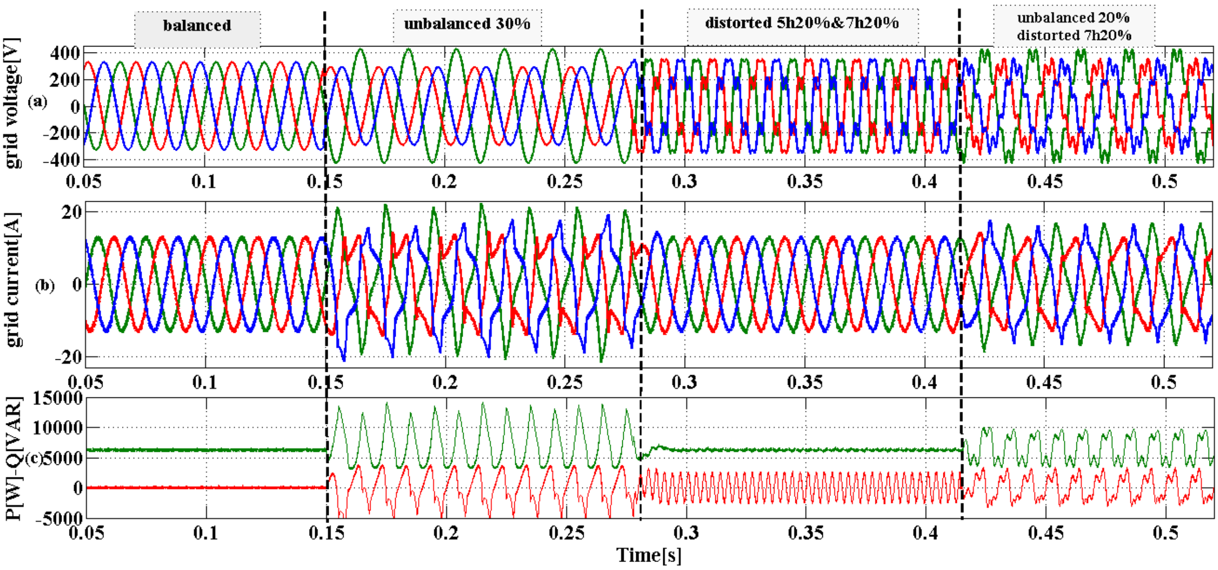

Fig. 10. The response of currents and injected power in distorted grid voltage:
(*a*) grid voltage; (*b*) grid current; (*c*) active power and reactive power

The study is conducted to evaluate the performance of the system under different grid voltage conditions. It is seen that under balanced gate voltages, the results give a sinusoidal grid current. Table 2 shows the THD ratio of two periods for each applied condition.

Table 2

Currents THD

Case	Balanced	Unbalanced 30 %	Distorted 5th and 7th 20 %	Unbalanced and distorted 7th 20 %
THD	1.89 %	27.83 %	2.38 %	18.46 %

According to Table 2, the THD of the currents is different for each condition of the applied voltages. The more unbalance in grid voltage, the more increase in THD we get, however it is not affected by the harmonic content in voltage as mentioned in [9].

2. With Proposed FV-DPC Compensation. Figures 11 and 12 show the results of the simulation after compensation. Figure 11 shows the performance of VF_DPC proposed under unbalanced and distorted voltages.

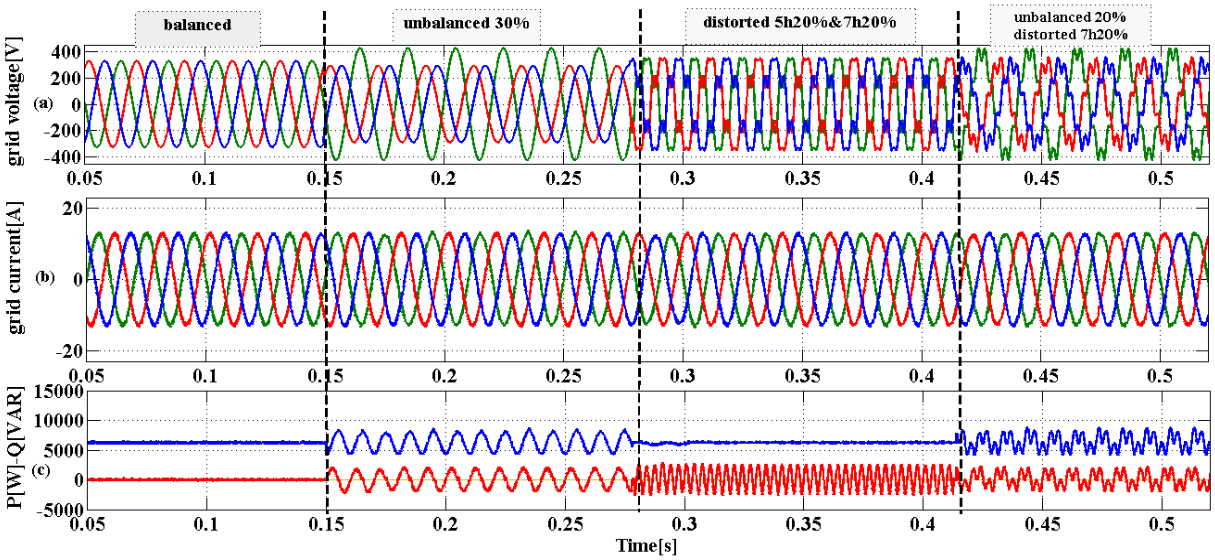

Fig. 11. The performance of the proposed VF_DPC in an unbalanced and distorted grid during different periods of wind variation:
(*a*) grid voltage; (*b*) grid current; (*c*) the active power and reactive power

As indicated in Figure 11,*b*, that the currents after the compensation are sinusoidal and balanced even for distorted and unbalanced voltages. The negative sequence and higher harmonic components of the gate currents are also controlled at zero. The THD of the grid currents, according to the IEEE Standard 519 harmonic, after compensation is limited. Table 3 presents the THD percentage of two periods of each condition applied.

Table 3

Currents THD

Case	Balanced	Unbalanced 30 %	Distorted 5th and 7th 20 %	Unbalanced and distorted 7th 20 %
THD	1.7 %	1.73 %	0.25 %	2.26 %

From Table 3, it is clear that the proposed control satisfactorily compensates for distortions and imbalances under all three-phase grid conditions demonstrating the superiority and performance of the proposed control.

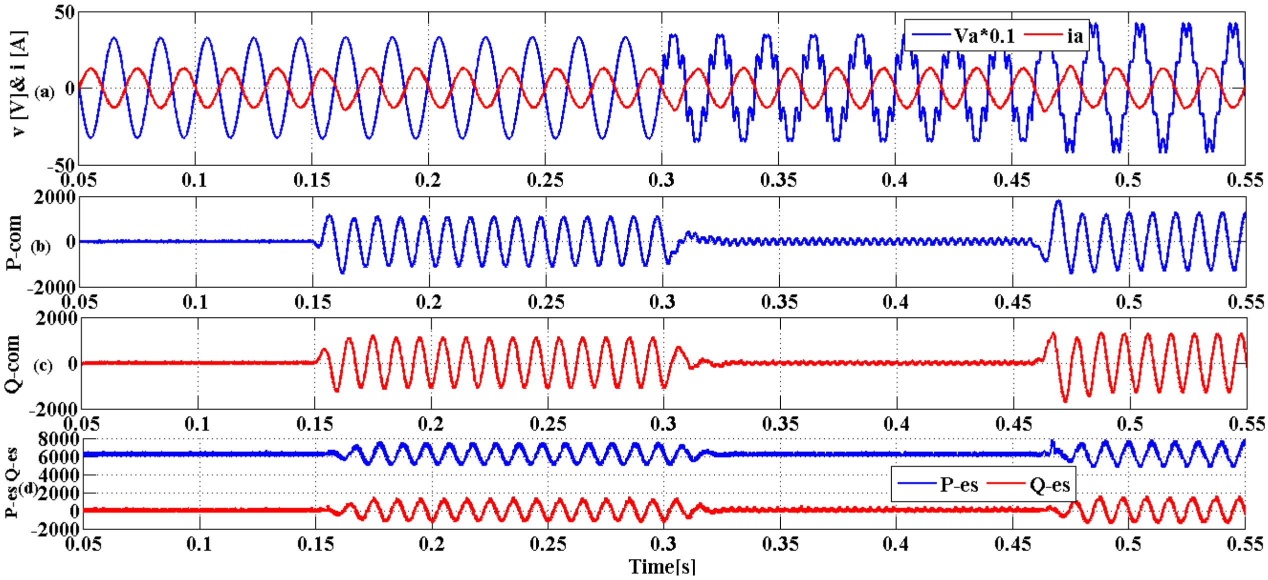

Fig. 12. Performance of the proposed VF_DPC in an unbalanced and distorted grid during different periods of wind variation: (*a*) grid voltage and current injected; (*b*) active power compensation; (*c*) reactive power compensation; (*d*) reactive and active power estimated and injected into the grid

Figure 12,*d* reveals that both active and reactive powers are well controlled. The reactive power is controlled to be zero to get a unity power factor. Figure 12,*b* and 12,*c* show the estimation block response of compensation powers. The use of this control process removes the effect of harmonic content and unbalanced voltages on the currents. We also note that the compensating powers of the distorted part are almost null in the case of harmonics in voltages, Figure 12,*b* and 12,*c*) [0.3 s 0.55 s].

The following relations show how to compensate with only negative power. We have

$$P_{har} = \omega \times \left[\left(\varphi_{s\alpha}^{h} \times i_{s\beta}^{+} - \varphi_{s\beta}^{h} \times i_{s\alpha}^{+}\right)\right] \cong 0;$$

$$Q_{har} = \omega \times \left[\left(\varphi_{s\alpha}^{h} \times i_{s\alpha}^{+} + \varphi_{s\beta}^{h} \times i_{s\beta}^{+}\right)\right] \cong 0.$$

So, it becomes

$$P_{com} = \omega \times \left[\left(\varphi_{s\alpha}^{-} \times i_{s\beta}^{+} - \varphi_{s\beta}^{-} \times i_{s\alpha}^{+}\right)\right];$$

$$Q_{com} = \omega \times \left[\left(\varphi_{s\alpha}^{-} \times i_{s\alpha}^{+} + \varphi_{s\beta}^{-} \times i_{s\beta}^{+}\right)\right].$$

Figure 13 shows the simulation results with only negative power compensation.

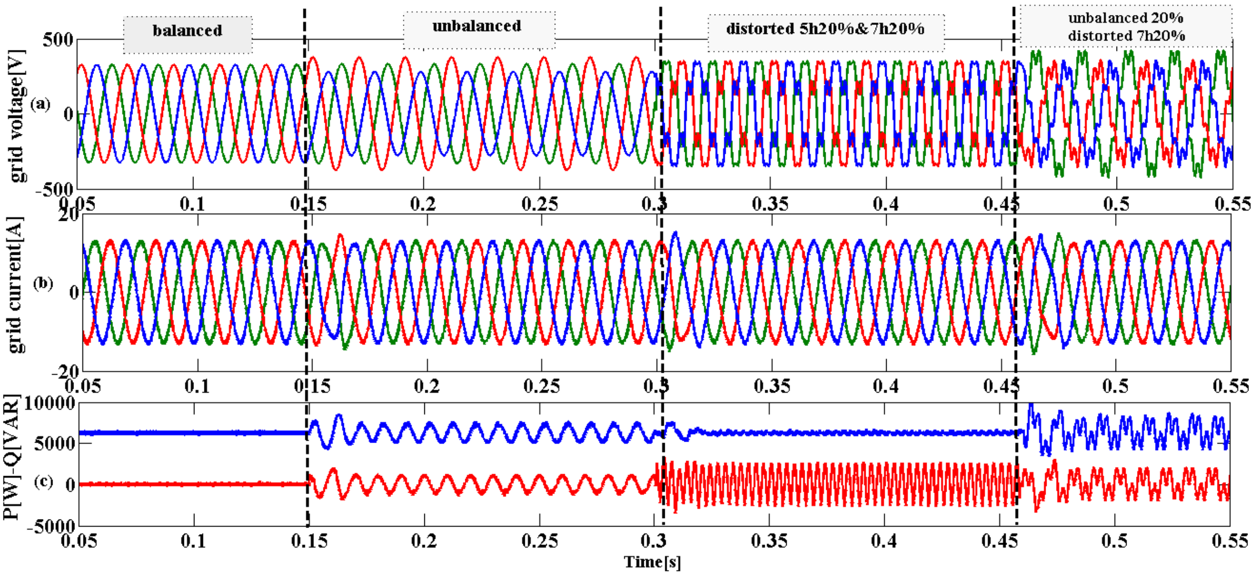

Fig. 13. The performance of VF_DPC with only negative power compensation: (*a*) grid voltage; (*b*) grid current; (*c*) active and reactive powers

Figure 13 shows that this method (compensation with negative powers) gives almost the same results similar to the previous method in terms of THD as shown in Table 4, except that a delay in response is estimated for one period. This is shown in Figure 13,*b*.

Table 4 presents the THD percentage of two periods of each condition applied.

Table 4

Currents THD

Case	Balanced	Unbalanced 30 %	Distorted 5th and 7th 20 %	Unbalanced and distorted 7th 20 %
THD	1.7 %	1.9 %	2.22 %	2.53 %

Conclusion.

This article proposes a strategy of controlling a micro wind turbine based on a PMSG by injecting maximum power and adapting to all disturbances that occur in the grid.

For this, a new control strategy VF_DPC is suggested for the grid converter. Thanks to the efficiency of the proposed controller, the three-phase grid currents are effectively regulated to be balanced and sinusoidal with very low direct current component despite deformed and unbalanced grid voltages. All the results are obtained at the maximum power of the wind turbine P_{ref}^* [W] and Q_{ref}^* of 0 [VAR].

The total harmonic distortion and the direct current component of the grid current are still kept very low and completely comply with European Standard (EN 50160) and IEEE Standard 519.

The simulation results gave 2.26 % for umbalanced and distorted voltage. In addition to good steady-state performance, this controller also provides a very fast dynamic response under the reference variation. The use of this control process removes the effect of harmonic content and unbalanced voltages on the currents.

The proposed current control scheme can be implemented without the need for grid-side voltage sensors; it can be easily integrated into the grid with reduced cost.

APPENDIX

Table A.1

Parameters of wind turbine

Parameter	Symbol	Value
Power	P_t	7.5 kW
Radius	R	3.24 m
Rated wind speed	N	296 rpm
Wind speed range	$V_{\text{cut-in}}$, $V_{\max}$	4-12 m/s
Inertia	J_t	7.5 kg·m^2
Friction coefficient	B_t	0.06 N·m·s/rad

Micro grid parameters: V_{rms} = 230 V, R_s = 0.1 Ω, L_s = 0.01 H, N = 50.

Table A.2

Parameters of PMSG

Parameter	Symbol	Value
Rated power	P_g	6 kW
Rated torque	T_g	40 N·m
Rated current	I	12 A
Rated speed	v	153 rad/sec
Number of poles	p	10
Magnet flux linkage	φm	0.433 Wb
Armature resistance	R_a	0.425 Ω
Stator inductance	L_s	8.4 mH

REFERENCES

1. Mendis N., Muttaqi K.M., Sayeef S., Perera S. Standalone Operation of Wind Turbine-Based Variable Speed Generators With Maximum Power Extraction Capability," IEEE Transactions on Energy Conversion, vol. 27, no. 4, pp. 822–834, Dec. 2012. **doi: 10.1109/tec.2012.2206594**.

2. Barote L., Marinescu C., Cirstea M.N. Control Structure for Single-Phase Stand-Alone Wind-Based Energy Sources. *IEEE Transactions on Industrial Electronics*, 2013, vol. 60, no. 2, pp. 764-772. **doi: 10.1109/tie.2012.2206346**.

3. Zammit D., Staines C.S., Micallef A., Apap M., Licari J. Incremental Current Based MPPT for a PMSG Micro Wind Turbine in a Grid-Connected DC Microgrid. *Energy Procedia*, 2017, vol. 142, pp. 2284-2294. **doi: 10.1016/j.egypro.2017.12.631.**

4. Venkatraman R., Bhat A. K. S. Large-signal transient analysis of a soft-switching, two-switch AC-to-DC converter. *IEE Proceedings - Circuits, Devices and Systems*, 2000, vol. 147, no. 2, pp. 146-152. **doi: 10.1049/ip-cds:20000177**.

5. Razali A.M., Rahman M.A. Virtual grid flux oriented control method for front-end three phase boost type voltage source rectifier. *2012 25th IEEE Canadian Conference on Electrical and Computer Engineering (CCECE)*, Montreal, Quebec, Canada, Apr. 2012. **doi: 10.1109/ccece.2012.6334922**.

6. Dannehl J., Wessels C., Fuchs F.W. Limitations of Voltage-Oriented PI Current Control of Grid-Connected PWM Rectifiers With LCL Filters. *IEEE Transactions on Industrial Electronics*, 2009, vol. 56, no. 2, pp. 380-388. **doi: 10.1109/tie.2008.2008774.**

7. Xu Lie, Zhi Dawei, Williams B.W. Predictive Current Control of Doubly Fed Induction Generators. IEEE Transactions on Industrial Electronics, 2009, vol. 56, no. 10, pp. 4143-4153. **doi: 10.1109/tie.2009.2017552**.

8. Lorenz R.D., Lipo T.A., Novotny D.W. Motion control with induction motors. *Proceedings of the IEEE*, 1994, vol. 82, no. 8, pp. 1215-1240. **doi: 10.1109/5.301685.**

9. Lee S.S., Heng Y.E. Table-based DPC for grid connected VSC under unbalanced and distorted grid voltages: Review and optimal method. *Renewable and Sustainable Energy Reviews*, 2017, vol. 76, pp. 51-61. **doi: 10.1016/j.rser.2017.03.033.**

10. Malinowski M. *Sensorless Control Strategies for Three-Phase PWM Rectifiers*. Ph.D. Thesis Warsaw University of Technology Faculty of Electrical Engineering Institute of Control and Industrial Electronics. Warsaw, Poland, 2001.

11. Zheng Z., Wang C. Research on Direct Power Control Strategy for PWM Rectifier. *2010 International Conference on Future Power and Energy Engineering*, Jun. 2010. **doi: 10.1109/ICFPEE.2010.30.**

12. Lauria D., Coppola M. Design and control of an advanced PV inverter. *Solar Energy*, 2014, vol. 110, pp. 533-542. **doi: 10.1016/j.solener.2014.09.040**.

13. Hussein M.M., Senjyu T., Orabi M., Wahab M.A.A., Hamada M.M. Load power management control for a stand alone wind energy system based on the state of charge of the battery. *2012 IEEE International Conference on Power and Energy (PECon)*, Dec. 2012. **doi: 10.1109/pecon.2012.6450352**.

14. European Standard EN 50160. Voltage characteristics of electricity supplied by public distribution systems. CENELEC, 2005.

15. IEEE Std 519-1992. IEEE Recommended Practices and Requirements for Harmonic Control in Electrical Power Systems, 1993, 112 p. **doi: 10.1109/IEEESTD.1993.114370**.

16. Allagui M., Hasnaoui O.B.k., Belhadj J. A 2MW direct drive wind turbine; vector control and direct torque control techniques comparison. *Journal of Energy in Southern Africa*, 2017, vol. 25, no. 2, pp. 117-126. **doi: 10.17159/2413-3051/2014/v25i2a2679.**

17. Prasad A.R., Ziogas P.D., Manias S. An active power factor correction technique for three-phase diode rectifiers.

IEEE Transactions on Power Electronics, 1991, vol. 6, no. 1, pp. 83-92. **doi: 10.1109/63.65006**.

18. Mohd Yusoff N.A., Razali A.M., Abdul Karim K., Sutikno T., Jidin A. A Concept of Virtual-Flux Direct Power Control of Three-Phase AC-DC Converter. *International Journal of Power Electronics and Drive Systems (IJPEDS)*, 2017, vol. 8, no. 4, pp. 1776-1784. **doi: 10.11591/ijpeds.v8.i4.pp1776-1784.**

19. Verdelho P., Marques G.D. DC voltage control and stability analysis of PWM-voltage-type reversible rectifiers *IEEE Transactions on Industrial Electronics*, 1998, vol. 45, no. 2, pp. 263-273. **doi: 10.1109/41.681225**.

20. Xiang L., Minxiao H. Direct Virtual Power Control. *Telkomnika*, 2014, vol. 12, no. 7, pp. 5144-5153 **doi: 10.11591/telkomnika.v12i7.5806.**

21. Malinowski M., Kazmierkowski M. Simple Direct Power Control of Three-Phase PWM Rectifier Using Space Vector Modulation – A Comparative Study. *EPE Journal*, 2003, vol. 13, no. 2, pp. 28-34. **doi: 10.1080/09398368.2003.11463529.**

22. Malinowski M., Kazmierkowski M.P., Hansen S., Blaabjerg F., Marques G.D. Virtual-flux-based direct power control of three-phase PWM rectifiers. *IEEE Transactions on Industry Applications*, 2001, vol. 37, no. 4, pp. 1019-1027. **doi: 10.1109/28.936392.**

23. Rahab A., Senani F., Benalla H. Direct Power Control of Three-Phase PWM Rectifier based DSOGI-VF Estimator for No-Ideal LineVoltages Conditions. *Int. Journal of Engineering Research and Application*, 2018, vol. 8, iss. 1 (part-1), pp. 10-18. **doi: 10.9790/9622-0801011018.**

24. Bouafia A., Gaubert J.P., Chaoui A. Direct Power Control Scheme Based on Disturbance Rejection Principle for Three-Phase PWM AC/DC Converter under Different Input Voltage Conditions. *Journal of Electrical Systems*, 2012, vol. 8, iss. 4, pp. 367-383.

25. Suul J.A., Undeland T. Impact of Virtual Flux reference frame orientation on voltage source inverters in weak grids. *The 2010 International Power Electronics Conference – ECCE ASIA*, Jun. 2010. **doi: 10.1109/ipec.2010.5542230.**

26. Malinowski M., Kazmierkowski M.P., Hansen S., Blaabjerg F., Marques G.D. Virtual-flux-based direct power control of three-phase PWM rectifiers. *IEEE Transactions on Industry Applications*, 2001, vol. 37, no. 4, pp. 1019-1027. **doi: 10.1109/28.936392.**

27. Haque M.E., Negnevitsky M., Muttaqi K.M. A Novel Control Strategy for a Variable Speed Wind Turbine with a Permanent Magnet Synchronous Generator. *2008 IEEE Industry Applications Society Annual Meeting*, Oct. 2008. **doi: 10.1109/08ias.2008.374.**

Received 10.02.2020

Ismail Boukhechem[1]*, Ph.D.,*
Ahcen Boukadoum[1]*, Doctor of Electrotechnical, Professor,*
Lahcene Boukelkoul[1]*, Doctor of Electrotechnical,*
Rima Lebied[1]*, Ph.D.,*
[1] Electrotechnical Laboratory Skikda (LES),
University 20 August 1955,
26 Road El Hadaiek 21000, Skikda, Algeria.
e-mail: sameu25@gmail.com,
boukadoum2003@yahoo.fr,
l_boukel@yahoo.co.uk,
rima42453@gmail.com

How to cite this article:
Boukhechem I., Boukadoum A., Boukelkoul L., Lebied R. Sensorless direct power control for three-phase grid side converter integrated into wind turbine system under disturbed grid voltages. *Electrical engineering & electromechanics*, 2020, no. 3, pp. 48-57. **doi: 10.20998/2074-272X.2020.3.08.**

UDC 621.3 **doi: 10.20998/2074-272X.2020.3.09**

S. Kalkoul, H. Benalla, K. Nabti, R. Abdellatif

AN ADAPTIVE HARMONIC COMPENSATION STRATEGY FOR THREE-PHASE SHUNT ACTIVE POWER FILTER BASED ON DOUBLE SECOND-ORDER GENERALIZED INTEGRATOR WITH PREFILTER

Abstract. This study presents a straightforward adaptive prefiltering algorithm based on a double second-order generalized integrator with prefilter to solve one of the power quality issues, this algorithm is in charge of the determination of the reference harmonic currents in the control of three-phase shunt active power filter which presents an effective way to enhance the grid current quality. The proposed algorithm is used twice, to extract the harmonic currents produced by the non-linear loads and be an interesting part in the estimation of the frequency and amplitude of the fundamental voltage in various anomalies which can be noticed on the grid voltage. The performance, precision, and robustness of the proposed method are evidenced under balanced, unbalanced, and distorted grid voltage in the simulation and experimental results obtained by the implementation of the shunt active power filter on MATLAB-Simulink environment and the dSPACE 1104 platform respectively. References 17, tables 2, figures 11.

Key words: **SOGI-WPF, SAPF, harmonic currents, power quality, DSOGI-PLL-WPF.**

Аннотация. В данной работе представлен простой адаптивный алгоритм предфильтрации, основанный на двойном обобщенном интеграторе с предфильтром второго порядка (DSOGI-WPF) для решения одного из вопросов качества электроэнергии. Данный алгоритм отвечает за определение опорных гармонических токов при контроле трехфазного фильтра шунта активной мощности (SAPF). Предложенный алгоритм используется дважды: для извлечения гармонических токов, создаваемых нелинейными нагрузками, и также является интересной частью оценки частоты и амплитуды основного напряжения при различных аномалиях, которые можно заметить по напряжению сети. Эффективность, точность и надежность предложенного метода подтверждаются при сбалансированном, несбалансированном и искаженном напряжении сети результатами моделирования и экспериментов, полученными при реализации SAPF в среде MATLAB-Simulink и платформе dSPACE 1104, соответственно. Библ. 17, табл. 2, рис. 11.

Ключевые слова: **обобщенный интегратор с предфильтром второго порядка (SOGI-WPF), фильтр шунта активной мощности (SAPF), гармонические токи, качество электроэнергии, двойной обобщенный интегратор с предфильтром второго порядка с фазовой синхронизацией (DSOGI-PLL-WPF).**

Introduction. The situation at the level of electrical energy networks has become very worrying, the quality of the current in electrical installations is undeniably deteriorating and some disturbances can act on the proper operation of many equipment and loads connected to the grid [1]. Therefore, it becomes a major concern for the distributors of this energy and its customers, this degradation results directly from the proliferation of charges that consume a non-sinusoidal current, called «non-linear loads», whereas using this kind of loads is not inevitable in the conversion and control of electrical power in different domains of industrial or domestic installations [2, 3].

In order to clean up the grid from the harmonic pollution there are several methods have been used, such as passive filter, where it can prevent harmonic currents from spreading in the grid, but, this type of filter has certain problems, like shortcoming of adaptability during variations of the impedance of grid and the load, considerable size, etc. [4]. To overcome the drawbacks of passive filter, the SAPF (shunt active power filter) presents a good alternative solution, which provides an unprecedented capacity for compensation and correction the harmonic distortions generated by non-linear loads. The role of SAPF based on the continuous injection of current at the connection point or PCC (point of common coupling), this current corresponds at any time to the harmonic current components absorbed by the load. In this way, the current supplied by the energy source remains sinusoidal [5].

To perform the SAPF task under any constraint that may appear in the grid (imbalance, frequency variation and so on), several methods of control and extraction of harmonic currents have been implemented in the time domain. Some have used in the balanced grid such as synchronous reference frame theory [6, 7], PQ theory [8], [9], others based on artificial neural networks have proposed in [10-12], which have proved its accuracy and performance in estimation of harmonic currents, but those structures present large complexity. In [13], the method based on multi second-order generalized integrator (MSOGI) has benne used to extract the multiple harmonic currents, but this structure cannot identify the inspected harmonics as the sub-harmonics or harmonics that have frequencies below the fundamental, furthermore, its implementation leads to increasing computing time [14]. A third-order complex-vector prefilter [15] known as third-order sinusoidal integrator has used in [17].

For the purpose of enhancing the performance of SAPF at high grid distortion, this paper employs an adaptive prefiltering method based on two-order SOGI to extract the harmonic currents and estimate the grid frequency, the two-order SOGI known as the second-order generalized integrator with prefilter SOGI-WPF in [14]. For the first time, the SOGI-WPF has been used in double SOGI-WPF structure or DSOGI-WPF with the frequency lock loop in the photovoltaic system to estimate the frequency and improve the speed of voltage sequence detection under abnormal grid conditions and cancel out the DC offset from the input signal [14]. In [16], the DSOGI-WPF is named as dual SO-SOGI, which has adopted as a step before phase detector PD in PLL (phase-locked loop) to generate the fundamental source current in distribution static synchronous compensator.

The **goal** of this paper is applying the double second-order generalized integrator with prefilter structure to extract the reference harmonic currents in the control of three-phase shunt active power filter and improve its operation under unusual grid voltage conditions (unbalanced, distorted). The method of double second-order generalized integrator with prefilter will be used to estimate the grid frequency, positive sequence components of the grid voltage, and extract the harmonic current components in the grid.

Description of the studied network. The general structure of SAPF is shown in Fig. 1, in addition to the grid elements (voltage source, grid impedance, and non-linear load). The SAPF constitutes of two parts. The first one is the power circuit which consists of a three-phase two-level voltage inverter fed by a DC-link capacitor (C_{dc}), the inverter is connected to the PCC through an inductance L_f and a resistance R_f which represent the output filter. The second part represents the control circuit, its first phase uses the method based on DSOGI-WPF to extract the reference harmonic currents and estimate the instantaneous angular frequency of the fundamental voltage (ω_1), a corrector of the V_{dc} voltage at terminals of capacitor C_{dc} is used to ensures a sufficient and non-fluctuations supply to the inverter by keeping the measured V_{dc} voltage at the reference voltage (in this case, PI corrector has been implemented), finally, a modulator based on the PWM technique for generating the pulses of the IGBTs of the inverter.

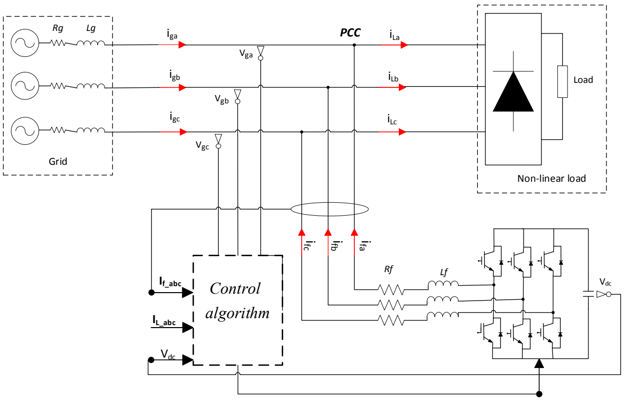

Fig. 1. Scheme diagram of three-phases SAPF

Second-order generalized integrator with prefilter. Fig. 2 shows the structure of the second-order generalized integrator with prefilter. Which is constituted of two SOGI connected in series, this allows building a fourth-order band-pass filter system for the in-phase and a fourth-order low-pass filter system for quadrature-phase. The k_1 and k_2 represent the proper gains of each SOGI, where $k_1 = 2\zeta 1$ and $k_2 = 2\zeta 2$ ($\zeta 1$ and $\zeta 2$ are the damping factors). For high-performance of the SOGI-WPF, those damping factors should be equals i.e. $\zeta 1 = \zeta 2 = \zeta$ [14]. The relation between the input signal and outputs in SOGI-WPF can be summarized from the block diagram presented in Fig. 2 by the transfer functions defined as

$$H(s)=\frac{V_1(s)}{V_g(s)}=\left(\frac{2\zeta\omega_n s}{s^2+2\zeta\omega_n s+\omega_n^2}\right)^2; \tag{1}$$

$$qH(s)=\left(\frac{2\zeta\omega_n s}{s^2+2\zeta\omega_n s+\omega_n^2}\right)\left(\frac{2\zeta\omega_n^2}{s^2+2\zeta\omega_n s+\omega_n^2}\right). \tag{2}$$

The transfer functions of SOGI are

$$G(s)=\frac{V_1^{'}(s)}{V_g(s)}=\frac{2\zeta\omega_n s}{s^2+2\zeta\omega_n s+\omega_n^2}; \tag{3}$$

$$qG(s)=\frac{qV_1^{'}(s)}{V_g(s)}=\frac{2\zeta\omega_n^2}{s^2+2\zeta\omega_n s+\omega_n^2}. \tag{4}$$

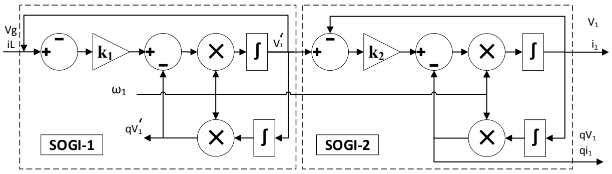

Fig. 2. Block diagram of SOGI-WPF

The bode plots of the SOGI and SOGI-WPF transfer functions are shown in Fig. 3. From the bode plots, it can be seen that the SOGI-WPF allows overcoming the drawbacks of the basic SOGI by eliminating the DC-offset from the quadrature signal and has a high performance at sub-harmonics attenuation of the input signal, which makes the SOGI-WPF more efficient and accurate at the separation of the fundamental component and the harmonic components.

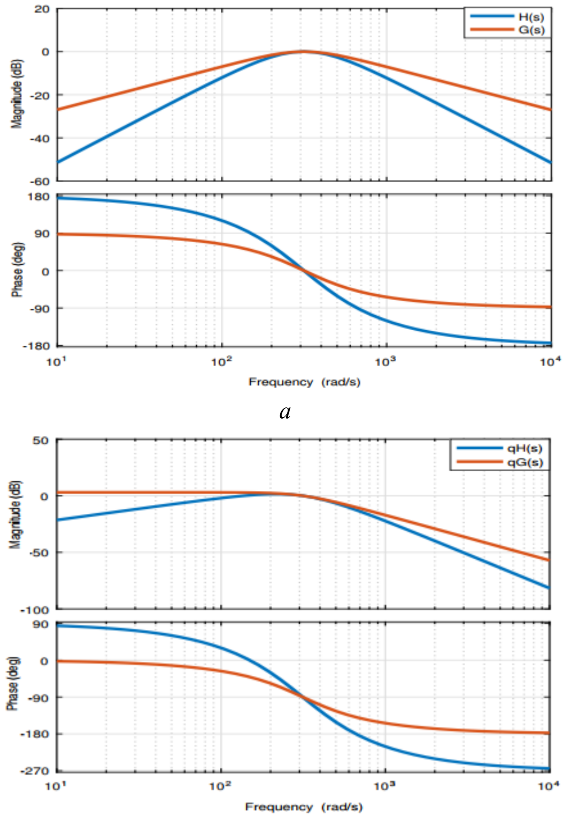

a

b

Fig. 3. Bode plot of SOGI and SOGI-WPF: *a* – $H(s)$ and $G(s)$ of in-phase voltage, *b* – $qH(s)$ and $qG(s)$ of quadrature voltage

Modeling the control of shunt active power filter. The proposed control algorithm that is depicted in Fig. 4, aims to generate the pulses of the inverter using the reference harmonic currents for compensating the grid harmonics produced by the non-linear load.

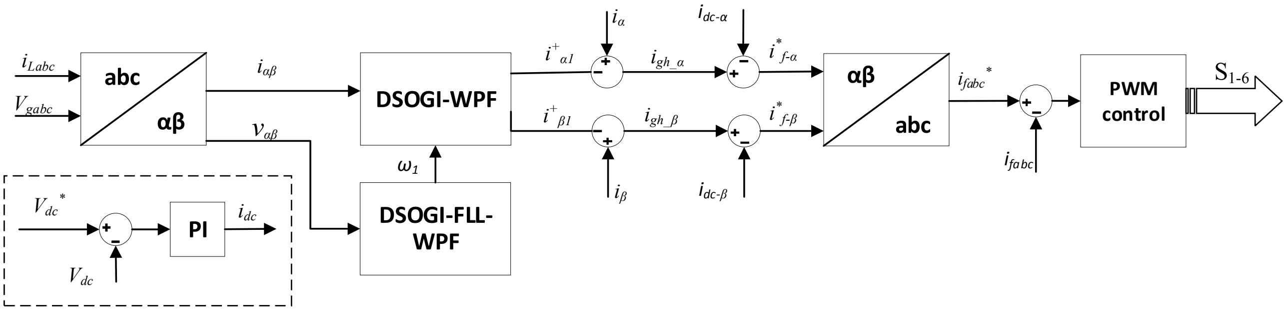

Fig. 4. Structure of the proposed control

1. Double second-order generalized integrator with prefilter. In this sub-section, the proposed method based on DSOGI-WPF, which is illustrated in Fig. 5, is employed as a filter to extract the harmonic components of the input signal and detect its positive sequence components.

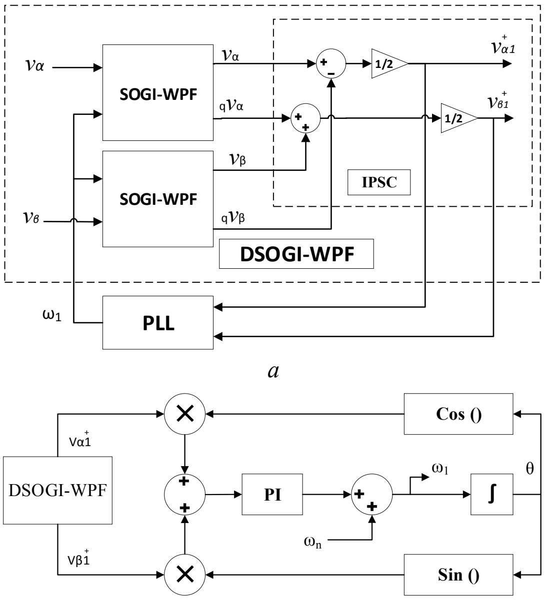

a

b

Fig. 5. Block diagram of the proposed synchronization method: *a* – DSOGI-WPF, *b* – DSOGI-PLL-WPF

As mentioned above, the DSOGI-WPF has two identical variables in each SOGI-WPF, where $k_1 = k_2 = 2\zeta$. To have an effective filtering performance with a fast dynamic response, the k_1 and k_2 are set to 0.8. The two SOGI-WPF lead to output the signals in-phase and quadrature-phase for α and β components (v_α, v_β, qv_α, and qv_β). To compute the positive sequence components $\left(v_{\alpha1}^+, v_{\beta1}^+\right)$ these signals are used as the inputs of instantaneous positive-sequence components IPSC calculation block as shown in Fig. 5, the IPSC in the stationary $\alpha\beta$ reference frame is given as

$$v_{\alpha\beta1}^+ = \frac{1}{2}\begin{bmatrix} 1 & -q \\ q & 1 \end{bmatrix} v_{\alpha\beta1}, \qquad (5)$$

where $q = e^{-j(\pi/2)}$, which represents a 90-lagging phase-shift operator. The amplitude of the positive sequence components detected by the DSOGI-WPF can be expressed as

$$\left|V_1^+\right| = \sqrt{\left(v_{\alpha1}^+\right)^2 + \left(v_{\beta1}^+\right)^2}\,. \qquad (6)$$

To obtain the positive sequence components of current, the same procedure as precedent is applied by using the DSOGI-WPF and IPSC blocks.

2. Frequency estimation and grid harmonics extraction. In order to estimate the frequency of the PCC voltage, the fundamental positive sequences $\left(v_{\alpha1}^+, v_{\beta1}^+\right)$ obtained by IPSC are straightforwardly used to implement the PLL based on in-quadrature signal generation as shown in Fig. 5, which is known as the DSOGI-PLL-WPF. The PLL that is illustrated in Fig. 5 uses the DSOGI-WPF as a prefiltering stage in the stationary reference frame (*αβ*) to eliminate the negative impact of the distorting harmonics, which makes it more accurate at the estimation of the frequency and the amplitude of the positive sequence. The frequency/phase generated by the PLL allows providing the phase-angle for the trigonometric functions and the fundamental frequency to the DSOGI-WPF. The PI controller gains of the SOGI-PLL-WPF are set to $k_p = 0.3$ and $k_i = 0.5$.

Identifying the positive-sequence for the grid current and make the SOGI-WPF adaptable with any variation may have occurred on the frequency by using SOGI-PLL-WPF allows extracting the harmonic current produced because of non-linear load by simple subtraction as illustrated in Fig. 4. In this case, the grid-harmonic currents in *αβ* reference frame can be calculated as

$$i_{gh-\alpha} = i_\alpha - i_{\alpha1}^+\,. \qquad (7)$$

$$i_{gh-\beta} = i_\beta - i_{\beta1}^+\,. \qquad (8)$$

3. V_{dc} regulator. To maintain the DC-link in SAPF at optimal reference voltage and lower the fluctuations on it, a PI controller is applied in a closed-loop as shown in Fig. 6. From this figure, the transfer function of the closed-loop system is depicted as

$$\frac{V_{dc}}{V_{dc}^*} = \frac{k_p s + k_i}{C_{dc} s^2 + k_p s + k_i}\,. \qquad (9)$$

The equation (9) refers to the second-order transfer function. Thus, $k_p = 2\zeta C_{dc}\omega_n$ and $k_i = C_{dc}\omega_n^2$, where

ω_n is the natural frequency, ζ is the damping factor and is taken as 0.707.

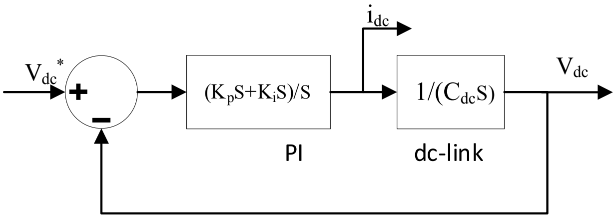

Fig. 6. Scheme of V_{dc} control

4. Reference currents computation. The reference currents for SAPF gather the harmonic currents of the grid that must be compensated and the currents necessary for the V_{dc} to be stable at the desired reference, which can be calculated as

$$i_f^* = i_{gh} - i_{dc}\,. \tag{10}$$

The i_f^* in stationary $\alpha\beta$ frame can be written as

$$i_{f-\alpha}^* = i_{gh-\alpha} - i_{dc-\alpha}\,; \tag{11}$$

$$i_{f-\beta}^* = i_{gh-\beta} - i_{dc-\beta}\,, \qquad (12$$

where the i_{dc} in stationary ($\alpha\beta$) reference frame is calculated as

$$i_{dc-\alpha} = i_{dc}\frac{v_{\alpha 1}^+}{\left|V_1^+\right|}\,. \tag{13}$$

$$i_{dc-\beta} = i_{dc}\frac{v_{\beta 1}^+}{\left|V_1^+\right|}\,. \tag{14}$$

The $i_{f-\alpha}^*$ and $i_{f-\beta}^*$ are transformed to i_{abc}^* by inverse Clarke's transformation. Finally, the PWM control generates the pulses of the inverter using error between the reference currents i_a^*, i_b^*, i_c^* and the injected currents i_{fa}^*, i_{fb}^*, i_{fc}^* respectively.

Simulation and experimental results performance. The simulation results have been obtained by modeling the SAPF on MATLAB-Simulink environment according to the topology presented in Fig. 1 and the different parameters of the system are illustrated in Table 1. The proposed algorithm is evaluated under balanced, distorted, and unbalanced voltage. To prove the performance of the SAPF in real-time, the control algorithm which based on DSOGI-WPF and DSOGI-PLL-WPF (Fig. 4 and Fig. 5 respectively) in extracting the reference harmonic currents has been executed by using the digital signal processor (dSPACE 1104 platform). As shown in Fig. 7, the measured load currents, injected harmonic currents by the SAPF, voltages of the PCC, and voltage of the DC-bus are connected via the Analog to Digital Conversion inputs of the dSPACE. The drivers of the IGBT modules of the inverter are controlled by the pulses sent via Digital output.

Table 1

System parameters

Parameters	Values
Grid voltage	V_{g_max}=100 V, f = 50 Hz
Source impedance	R_g = 0.5 Ω, L_g = 1 mH
DC-link	C_{dc}=1100 µF, V_{dc} = 280 V
Output filter	R_f = 0.6 Ω, L_f = 12.5 mH
Non-linear load	Three-phase rectifier, R_L = 33 Ω
PLL-PI gains	K_p = 0.3, K_i = 0.5
SOGI-WPF gains	$k_1 = k_2$ = 0.8
DC-link control gains	K_p = 0.49, K_i = 109
Switching frequency	7 kHz
Sampling frequency	14 kHz

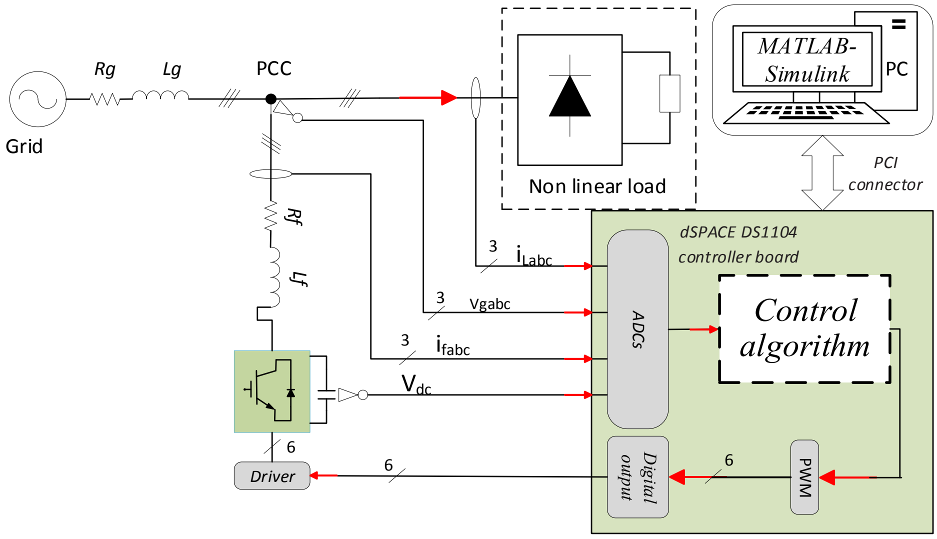

Fig. 7. Experimental schematic of SAPF

1. Behavior of the SAPF under sinusoidal grid voltage condition. Fig. 8,*a* and Fig. 8,*b* respectively show the simulation and the experimental results of the SAPF under sinusoidal supply voltage. Indeed, the voltage at the PCC is slightly affected by the harmonics caused by the main network whose voltages V_{ga}, V_{gb}, V_{gc} have a total harmonic distortion (THD) of 1, 1.2, and 1.4 % respectively. The performance of the control based on DSOGI-WPF is remarkable where the harmonized currents generated by the load are almost compensated by the SAPF currents which give back the waveform of the source current sinusoidal. Table 2 illustrates the THD of the load and the source currents, which shows that the THD of the source currents is greatly reduced.

Table 2

Current total harmonic distortion

	THD (%) load currents			THD (%) source currents		
	i_{La}	i_{Lb}	i_{Lc}	i_{ga}	i_{gb}	i_{gc}
Balanced grid voltage	21.8	22.3	23.1	3.5	3.6	4.2
Distorted grid voltage	19.1	19.3	20	4.5	4.3	4.6
Unbalanced grid voltage	19.1	21.9	23.1	3.9	4	4.3

2. Behavior of the SAPF under distorted grid voltage condition. In this study, the waveform of the grid voltage has a deformed shape due to the presence of harmonics, the voltage of each phase is perturbed by a high amount of the –5th and +7th harmonic components with a THD of 13, 14.7, and 13.2 % for V_{ga}, V_{gb}, V_{gc} respectively.

Figure 9 illustrates the performance of the proposed SAPF command while the supply voltage is distorted. As observed in Fig. 9,*a* and Fig. 9,*b*, the source current has a shape close to sinusoidal in the simulation and experimental results, which confirms the robustness and the precision of the DSOGI-WPF. The acceptable THD of the source current which describes in Table 2 also demonstrates that the proposed algorithm based on DSOGI-PLL-WPF makes the SAPF well synchronized with the fundamental frequency of the PCC voltage which is affected by harmonics.

3. Behavior of the SAPF under unbalanced grid voltage condition. In this situation, the grid voltage is characterized by the following measurements: the amplitudes of the three phases are V_{ga} = 110 V, V_{gb} = 96 V, V_{gc} = 82 V with a total harmonic distortion of 1.8, 3.7, and 7.7 % respectively. The voltage unbalancing is achieved by inserting resistors of different values in series with the three phases. In Fig. 10,*a* and Fig. 10,*b*, the simulation and the experimental results are presented, where the performance of the SAPF under distorted-unbalanced voltage is validated. It is clear that the efficiency of SAPF is not influenced by distorted-unbalanced voltage. The THD of each phase of the source and load currents is illustrated in Table 2, where the recommendations of the IEEE standard concerning the THD are observed.

4. Comparison between SOGI-PLL-WPF and SOGI-PLL under distorted voltage. Figure 11 shows the performance comparison of the SOGI-PLL-WPF and the basic SOGI-PLL under distorted grid voltage. It is clear that the SOGI-PLL-WPF is more robust and efficient than the SOGI-PLL under such abnormalities of the PCC voltage, in which the frequency estimated using SOGI-PLL contains a high level of ripple compared to SOGI-PLL-WPF method in both simulation and experimental results.

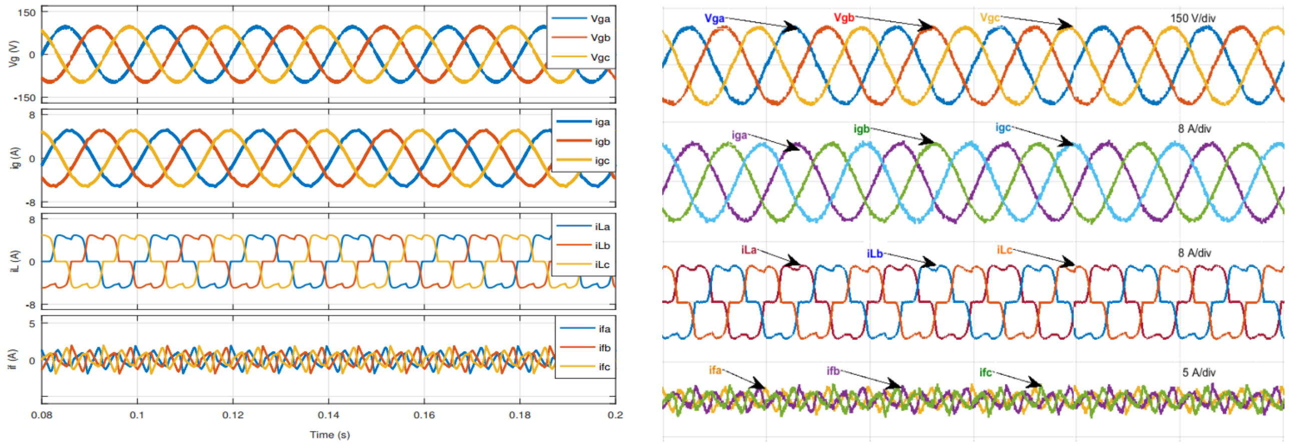

a *b*

Fig. 8. Behavior of the SAPF under sinusoidal grid voltage condition: *a* – simulation results, *b* – experimental results

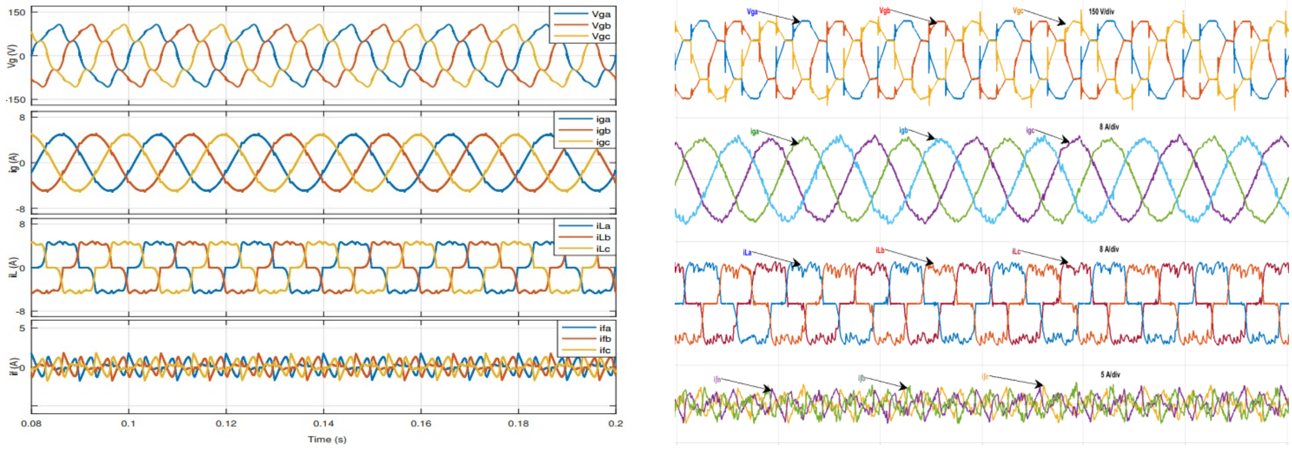

a *b*

Fig. 9. Behavior of the SAPF under distorted grid voltage condition: *a* – simulation results, *b* – experimental results

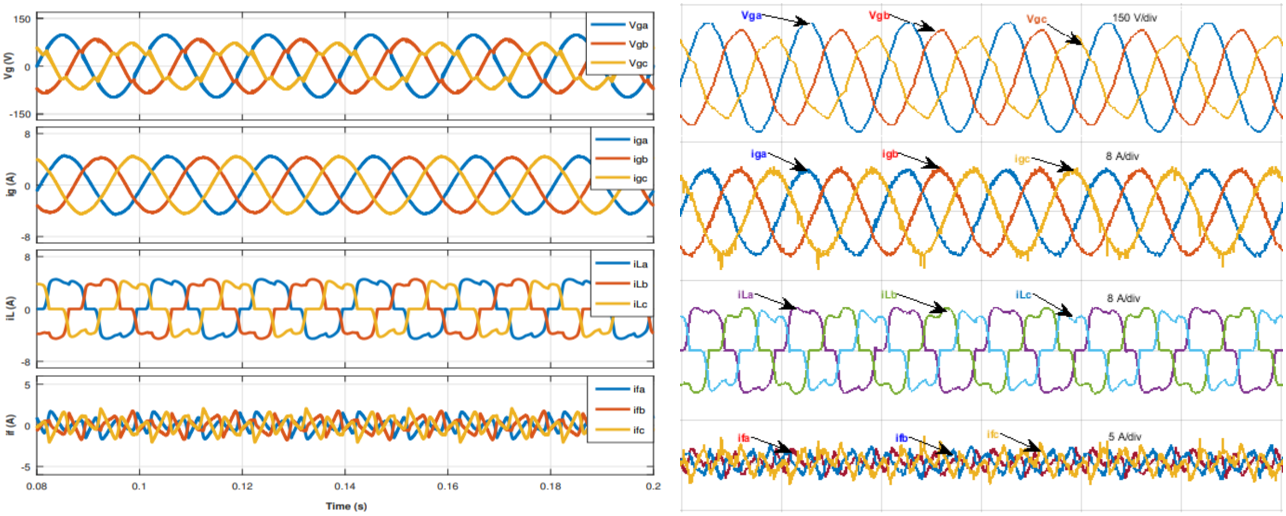

a *b*

Fig. 10. Behavior of the SAPF under unbalanced grid voltage condition: *a* – simulation results, *b* – experimental results

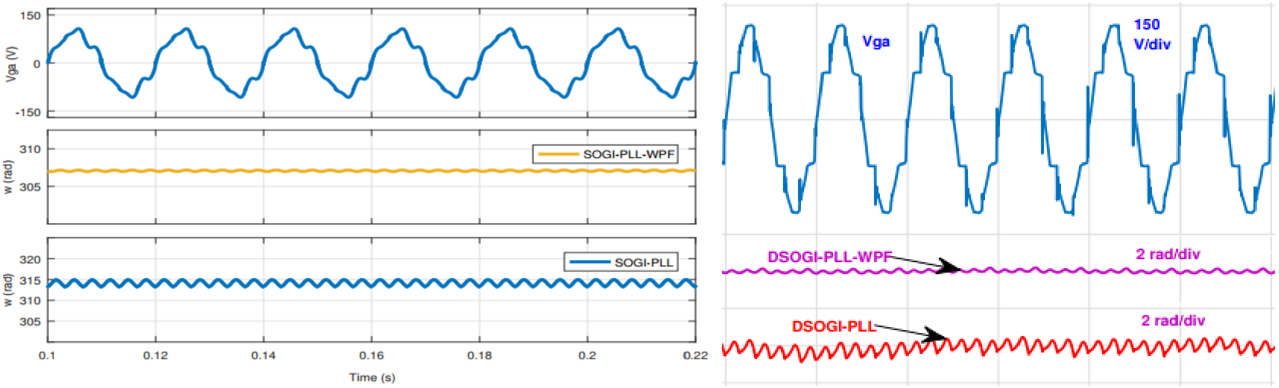

a *b*

Fig. 11. Performance of SOGI-PLL-WPF and SOGI-PL: *a* – simulation results, *b* – experimental results

Conclusion. This proposed work has extended the straightforward prefiltering method based on double second-order generalized integrator with prefilter to extract the reference harmonic current components for the control of the three-phase shunt active power filter, allowing a significant attenuation of the harmonics of the source currents and consequently improving its quality. The performance of the proposed configuration has been proven, where the total harmonic distortion has had significant reduction from about 22 % to less than 4.2 % under sinusoidal voltage, in distorted voltage, the total harmonic distortion is mitigated to about 4.6 % and nearly to 4.3 % under unbalanced voltage, which demonstrates the effectiveness and robustness of the proposed algorithm. This also signifies that even the abnormalities of the point of common coupling voltage, the phase-locked loop based on double second-order generalized integrator with prefilter has estimated grid fundamental voltage magnitude and frequency accurately and makes the shunt active power filter always synchronized. The main advantage of the represented structure appeared in the results of the experiment, where it has given good results with reduced computation time. The experimental results have been quite identical to those obtained by simulation in MATLAB-Simulink.

REFERENCES

1. Taskovski D., Koleva L., Milchevski A., Dimcev V. Near perfect reconstruction filter banks for power quality analysis. *Metrology and Measurement Systems*, 2013, vol. 20, no. 3, pp. 359-370. **doi: 10.2478/mms-2013-0031.**

2. Tugay D.V. The phase reactor inductance selection technique for power active filter. *Electrical Engineering & Electromechanics*, 2016, no. 6, pp. 31-38. **doi: 10.20998/2074-272X.2016.6.06.**

3. Patil K., Patel H.H. Modified SOGI based shunt active power filter to tackle various grid voltage abnormalities. *Engineering Science and Technology, an International Journal*, 2017, vol. 20, no. 5, pp. 1466-1474. **doi: 10.1016/j.jestch.2017.10.004.**

4. Naderi Y., Hosseini S.H., Ghassem Zadeh S., Mohammadi-Ivatloo B., Vasquez J.C., Guerrero J.M. An overview of power quality enhancement techniques applied to distributed generation in electrical distribution networks. *Renewable and Sustainable Energy Reviews*, 2018, vol. 93, pp. 201-214. **doi: 10.1016/j.rser.2018.05.013.**

5. Garcia Campanhol L.B., Oliveira da Silva S.A., Goedtel A. Application of shunt active power filter for harmonic reduction and reactive power compensation in three-phase four-wire systems. *IET Power Electronics*, 2014, vol. 7, no. 11, pp. 2825-2836. **doi: 10.1049/iet-pel.2014.0027.**

6. Soares V., Verdelho P., Marques G.D. An instantaneous active and reactive current component method for active filters.

IEEE Transactions on Power Electronics, 2000, vol. 15, no. 4, pp. 660-669. **doi: 10.1109/63.849036.**

7. Sena K.V. Power Quality Improvement using Five Level Active Power Filter with SRF Control Technique. *International Journal of Advanced Research in Electrical, Electronics and Instrumentation Engineering*, 2014, vol. 3, no. 7, pp. 10468-10476. **doi: 10.15662/ijareeie.2014.0307012.**

8. Akagi H., Kanazawa Y., Nabae A. Instantaneous reactive power compensators comprising switching devices without energy storage components. *IEEE Transactions on Industry Applications*, 1984, vol. IA-20, no. 3, pp. 625-630. **doi: 10.1109/TIA.1984.4504460.**

9. Wang H., Li Q., Wu M. Investigation on a new algorithm for instantaneous reactive and harmonic currents detection applied to intensive nonlinear loads. *IEEE Transactions on Power Delivery*, 2007, vol. 22, no. 4, pp. 2312-2318. **doi: 10.1109/TPWRD.2007.905379.**

10. Qasim M., Kanjiya P., Khadkikar V. Artificial-Neural-Network-Based Phase-Locking Scheme for Active Power Filters. *IEEE Transactions on Industrial Electronics*, 2014, vol. 61, no. 8, pp. 3857-3866. **doi: 10.1109/TIE.2013.2284132.**

11. Bhattacharya A., Chakraborty C. A Shunt Active Power Filter With Enhanced Performance Using ANN-Based Predictive and Adaptive Controllers. *IEEE Transactions on Industrial Electronics*, 2011, vol. 58, no. 2, pp. 421-428. **doi: 10.1109/TIE.2010.2070770.**

12. Jarupula S., Mannam V.G.R., Vutlapalli N.R. Power quality improvement in distribution system using ANN based shunt active power filter. *International Journal of Power Electronics and Drive Systems (IJPEDS)*, 2015, vol. 5, no. 4, pp. 568-575. **doi: 10.11591/ijpeds.v5.i4.pp568-575.**

13. Xiao C., Pei X., Y Liu., Lu Y., Wang C., Xu F. Adaptive harmonic current compensation method with SAPF based on SOGI. *2018 IEEE International Power Electronics and Application Conference and Exposition (PEAC)*, 2018, pp. 1-6. **doi: 10.1109/PEAC.2018.8590342.**

14. Matas J., Castilla M., Miret J., García de Vicuña L., Guzman R. An adaptive prefiltering method to improve the speed/accuracy tradeoff of voltage sequence detection methods under adverse grid conditions. *IEEE Transactions on Industrial Electronics*, 2014, vol. 61, no. 5, pp. 2139-2151. **doi: 10.1109/TIE.2013.2274414.**

15. Li W., Ruan X., Bao C., Pan D., Wang X. Grid synchronization systems of three-phase grid-connected power converters: a complex-vector-filter perspective. *IEEE Transactions on Industrial Electronics*, 2014, vol. 61, no. 4, pp. 1855-1870. **doi: 10.1109/TIE.2013.2262762.**

16. Yada H.K., Murthy M.S.R., Prakash K. A Novel Control Algorithm for DSTATCOM Based on Three-Phase Dual SO-SOGI-PLL under Non-Ideal Grid Voltage Conditions Including DC-Offset. *International Journal of Applied Engineering Research*, 2017, vol. 12, no 10, pp. 2480-2488.

17. Chilipi R., Al Sayari N., Al Hosani K., Fasil M., Beig A.R. Third order sinusoidal integrator (TOSSI)-based control algorithm for shunt active power filter under distorted and unbalanced voltage conditions. *International Journal of Electrical Power & Energy Systems*, 2018, vol. 96, pp. 152-162**. doi: 10.1016/j.ijepes.2017.09.026.**

Received 24.01.2020

Sami Kalkoul[1], *PhD, Associate Professor,*
Hocine Benalla[1], *PhD, Professor,*
Khalil Nabti[1], *PhD, Professor,*
Reama Abdellatif[2], *PhD, Professor,*
[1] Mentouri Brothers University, Constantine 1,
Campus Ahmed Hamani Zarzara, Route d'Ain el Bey,
Constantine, 25000, Algeria.
e-mail: sami.kalkoul@lec-umc.org, benalladz@yahoo.fr, khalilnb2003@gmail.com,
[2] System Engineering Department,
École Supérieure d'Ingénieurs en Électrotechnique et Électronique (ESIEE),
Cité Descartes, 2 Boulevard Blaise Pascal,
93160 Noisy-le-Grand, France.
e-mail: abdellatif.reama@esiee.fr

How to cite this article:
Kalkoul S., Benalla H., Nabti K., Abdellatif R. An adaptive harmonic compensation strategy for three-phase shunt active power filter based on double second-order generalized integrator with prefilter. *Electrical engineering & electromechanics*, 2020, no. 3, pp. 58-64. **doi: 10.20998/2074-272X.2020.3.09.**

UDC 621.3 **doi: 10.20998/2074-272X.2020.3.10**

L. Louze, O. Abdessemad, A.L. Nemmour, A. Khezzar

AN EFFECTIVE CONTROL OF AN ISOLATED INDUCTION GENERATOR SUPPLYING DC LOAD FOR WIND POWER CONVERTING APPLICATIONS

Purpose. The aim of this paper is to perform a simple and robust control method based on the well-known sliding control approach for a self-excited induction generator supplying an isolated DC load; this adopted technique does not require much computation and could be easily implemented in practice. In this context, the present work will begin with a mathematical development of this control technique and its application to the self-excited induction generator case. For this purpose, the machine provides the produced active power to the load through a static PWM converter equipped with a single capacitor on the DC side. In order to insure the output DC-bus voltage regulation with respect to the load-power demands and the rotor speed fluctuations, the required stator currents references are computed by considering the reactive power required for the machine core magnetization, the induced voltages through the stator windings and the active power set value obtained from the corresponding sliding mode DC-bus voltage controller. Regarding the nonlinearity of the DC-bus voltage mathematical model and the discontinuity characterizing the converter-machine behavior association, the sliding mode strategy will constitute a perfect tool to sizing the controller structure with high control performances. Results of simulation carried out to demonstrate the proposed control validity are presented. References 26, figures 6.

Key words: **self excited induction generator, sliding mode control, DC-bus voltage regulation.**

Целью данной статьи является разработка простого и надежного метода управления, основанного на хорошо известном подходе к управлению скольжением для асинхронного генератора с самовозбуждением, питающего изолированную нагрузку постоянного тока; данный принятый метод не требует больших объемов вычислений и может быть легко реализован на практике. В этом контексте данная работа начинается с развития математических основ этого метода управления и его применения в случае асинхронного генератора с самовозбуждением. Для этого машина подает произведенную активную мощность в нагрузку через статический ШИМ-преобразователь, оснащенный единственным конденсатором на стороне постоянного тока. Чтобы обеспечить регулирование выходного напряжения шины постоянного тока с учетом требований к нагрузке и колебаниям скорости вращения ротора, требуемые токи статора рассчитываются с учетом реактивной мощности, необходимой для намагничивания сердечника машины, наведенных напряжений в обмотках статора и заданного значения активной мощности, полученного из соответствующего контроллера напряжения шины постоянного тока в режиме скольжения. Что касается нелинейности математической модели напряжения шины постоянного тока и неоднородности, характеризующей поведение системы «преобразователь-машина», стратегия скользящего режима будет представлять собой идеальный инструмент для определения размеров конструкции контроллера с высокими характеристиками управления. Для демонстрации обоснованности предлагаемого метода контроля, приведены результаты выполненного моделирования. Библ. 26, Рис. 6.

Ключевые слова: **асинхронный генератор с самовозбуждением, управление режимом скольжения, регулирование напряжения на шине постоянного тока.**

Introduction. Induction generators constitute a potential choice for off-grid applications. When operating in self-excited mode. For a given input prime mover-mechanical power, the squirrel-cage relative to these machines configuration requires only a reactive power to insure the main core magnetization.

Generally, the machine magnetizing procedure could be performed in several ways; from simple capacitors to complex static power conversion systems. Many studies have been presented as well as in steady-state and transient analysis of the squirrel cage induction generator based stand-alone wind energy conversion systems [1-9].

For the output-voltage self-excited induction generator (SEIG) regulation, a number of works have been proposed structures based on switched capacitors [10-15], a saturable reactors scheme [16, 17], and short shunt or long shunt configurations schemes [18-22]. Works that are more recent use voltage source converter based voltage and frequency controller [23-25].

The aim of this paper is to achieve an efficient control strategy for self-excited induction generator driven by a wind turbine and associated to a static voltage source converter with an output DC link.

For this reason, the sliding mode control strategy is applied to regulate the DC voltage on the DC side for a variable DC load taking into account the rotor speed variations. As practical uses, the regulated DC voltage obtained could be used to charge a battery set, to supply isolated DC loads or be further converted into fixed-frequency AC power by an inverter to supply AC loads.

Mathematical model for the self-excited induction generator. By adopting the frequently assumptions, the general equations of three-phase induction machines in the (α, β), stationary reference frame are given by:

$$\begin{cases} v_{s\alpha} = R_s i_{s\alpha} + L_s \dfrac{di_{s\alpha}}{dt} + M\dfrac{di_{r\alpha}}{dt} \\ v_{s\beta} = R_s i_{s\beta} + L_s \dfrac{di_{s\beta}}{dt} + M\dfrac{di_{r\beta}}{dt} \\ 0 = R_r i_{r\alpha} + L_r \dfrac{di_{r\alpha}}{dt} + M\dfrac{di_{s\alpha}}{dt} - \omega\left(L_r i_{r\beta} + M i_{s\beta}\right) \\ 0 = R_r i_{r\beta} + L_r \dfrac{di_{r\beta}}{dt} + M\dfrac{di_{s\alpha}}{dt} + \omega\left(L_r i_{r\alpha} + M i_{s\alpha}\right) \end{cases}, \quad (1)$$

where s and r denote stator and rotor quantities; v and i represent instantaneous voltages and currents respectively; R_s and R_r are the stator and rotor resistances respectively; L_s, L_r and M are stator, rotor and magnetizing inductances respectively and ω represents the rotor angular velocity.

Sliding mode control. General concepts. The general form of sliding surface which guarantees the convergence of the state x to its reference x^* is given as follows:

$$S(x)=\left(\frac{d}{dt}+\gamma\right)^{n-1}\left(x^*-x\right), \tag{2}$$

where n is the degree of the sliding surface and γ is a strictly positive constant.

The first convergence condition allowing the dynamic system to converge towards the sliding surfaces must verify the well-known Lyapunov function expressed in terms of the system state-variables given by:

$$V(x)=\frac{1}{2}S^2(x). \tag{3}$$

To insure the Lyapunov function decreases, it is necessary to ensure that its derivative is negative. This is verified if:

$$\dot{S}(x)S(x)<0. \tag{4}$$

In order to perform the control quantity U_c, which contains two terms, first for the exact linearization term U_{eq}, the second discontinuous one for the system stability U_n:

$$U_c=U_{eq}+U_n. \tag{5}$$

The first control term U_{eq} is obtained from the condition $\dot{S}(x)=0$ when the second control term U_n is selected to guarantee the attractivity of the variable to be controlled towards the commutation surface.

Application to the self-excited induction generator. For the induction generator sliding mode controller design, the adopted switching surface is:

$$S=V_{dc}^*-V_{dc}, \tag{6}$$

where V_{dc} denotes the DC voltage in the DC side.

The derivative of (6) gives:

$$\dot{S}=\dot{V}_{dc}^*-\dot{V}_{dc}. \tag{7}$$

If the inverter losses are neglected, the relationship between the DC-bus power P_{dc} and the stator power side P_s is as follows:

$$P_s=P_{dc}+P_{load}, \tag{8}$$

where P_{load} denotes the active power consumed by the load on the DC-bus side.

Taking into account that the capacitor power P_{dc} is expressed by:

$$P_{dc}=V_{dc}i_{dc}=CV_{dc}\dot{V}_{dc}, \tag{9}$$

where C represents the capacitor value on the converter DC side, therefore:

$$P_s=CV_{dc}\dot{V}_{dc}+P_{load}. \tag{10}$$

From (10), the output DC bus voltage derivative is given by:

$$\dot{V}_{dc}=\frac{1}{CV_{dc}}\left(P_s-P_{load}\right). \tag{11}$$

From (11), (7) becomes:

$$\dot{S}=\dot{V}_{dc}^*-\frac{1}{CV_{dc}}\left(P_s-P_{load}\right). \tag{12}$$

By referring to (11), it is clear that P_s represents the control quantity and P_{load} acts as a disturbance for the V_{dc} closed control loop.

For sliding mode purposes, the control quantity set value P_s^* takes the form of (5) as:

$$P_s^*=P_{s\_eq}+P_{s\_n}. \tag{13}$$

Under these conditions, (12) gives:

$$\dot{S}=\dot{V}_{dc}^*-\frac{1}{CV_{dc}}\left(P_{s\_eq}+P_{s\_n}-P_{load}\right). \tag{14}$$

In the steady state conditions, the sliding surface is zero, and therefore its derivative and the discontinuous part are also zero, so:

$$P_{s\_eq}=CV_{dc}\dot{V}_{dc}^*+P_{load}. \tag{15}$$

By replacing the equivalent control with its expression in (14), the following surface derivative is obtained:

$$\dot{S}=-\frac{1}{CV_{dc}}P_{s\_n}. \tag{16}$$

The attractiveness condition expressed by (4) relative to the Lyapunov condition imposes the following choice of the P_{s_n} according to:

$$P_{s\_n}=k\times\operatorname{sign}(S), \tag{17}$$

where k is a positive gain.

Finally, the global control is performed by the following equation:

$$P_s^*=C\dot{V}_{dc}^*+P_{load}+k\times\operatorname{sign}(S). \tag{18}$$

Since the active and reactive stator powers can be expressed in terms of the stator current components $i_{s\alpha}$ and $i_{s\beta}$ as:

$$\begin{bmatrix} P_s^* \\ Q_s^* \end{bmatrix}=\begin{bmatrix} v_{s\alpha} & v_{s\beta} \\ -v_{s\beta} & v_{s\alpha} \end{bmatrix}\begin{bmatrix} i_{s\alpha}^* \\ i_{s\beta}^* \end{bmatrix}. \tag{19}$$

Then, the reference stator current components $i_{s\alpha}^*$ and $i_{s\beta}^*$ to be injected to the stator windings are given by:

$$\begin{bmatrix} i_{s\alpha}^* \\ i_{s\beta}^* \end{bmatrix}=\begin{bmatrix} v_{s\alpha} & v_{s\beta} \\ -v_{s\beta} & v_{s\alpha} \end{bmatrix}^{-1}\begin{bmatrix} P_s^* \\ Q_s^* \end{bmatrix}. \tag{20}$$

Figure 1 shows the corresponding controller structure relative to the used sliding mode method.

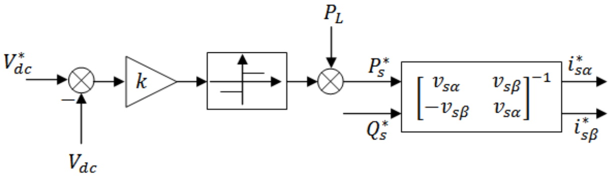

Fig. 1. Sliding mode control applied to the DC-bus voltage regulation

The proposed control scheme using hysteresis controllers is shown in Fig. 2.

Simulations and results. The proposed control has been simulated for an induction machine with the following parameters [26]: (3.6 kW, 415 V, 7.8 A, 50 Hz, 4 poles), whose per-phase equivalent circuit constants are: $L_s = L_r =$ $= 241.4$ mH, $M = 230$ mH, $R_s = 1.7\ \Omega$ and $R_r = 2.7\ \Omega$.

The DC-bus voltage regulation and the corresponding main machine's characteristics obtained using the proposed sliding mode controller in presence of stern disturbances such as a step-changing of the load power P_{load}, a step-changing of the DC-bus voltage reference value and finally, when the wind turbine imposes to the induction generator shaft a variable speed profile.

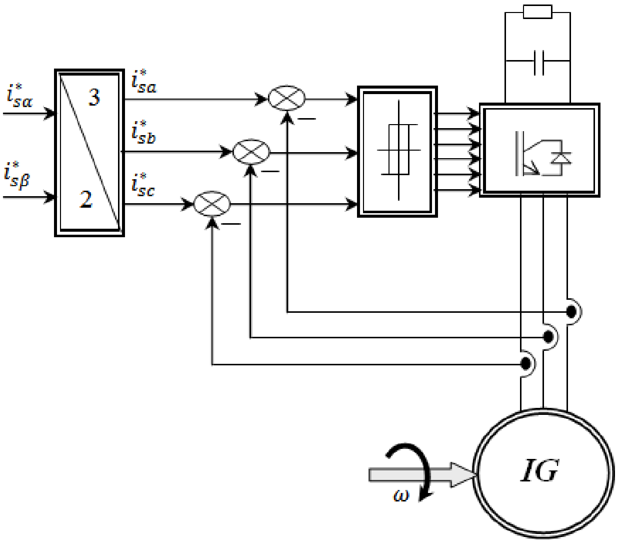

Fig. 2. Induction generator (IG) control structure used

The DC-bus voltage regulation performances under a constant rotor speed. Figure 3 shows the dynamic responses of the no-load operation followed up by a sudden load power variation P_{load} = 3500 W introduced at $t = 0.5$ s, then a step changing of the DC-bus voltage from 600 V to 700 V introduced at $t = 1$ s.

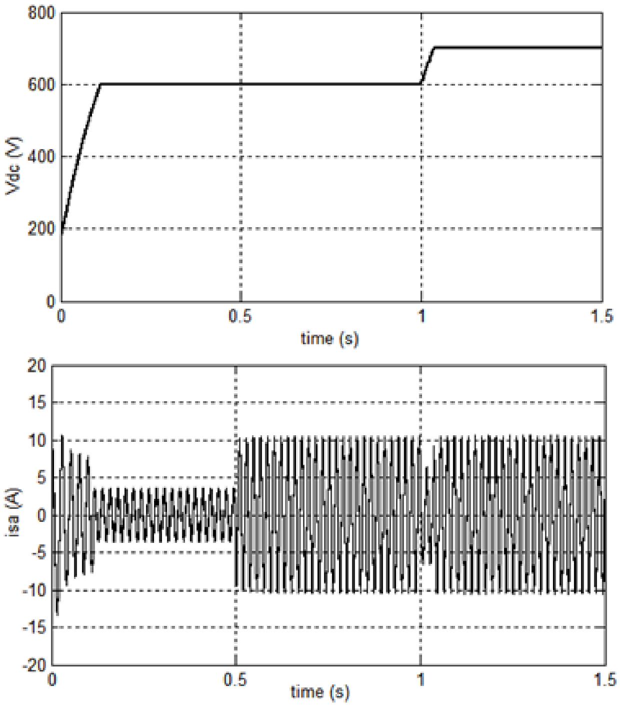

Fig. 3. The generator performances
($\omega = 300$ rad/s and $C = 1000$ µF)

The proposed control method based on the described sliding mode controller offers a fast DC-bus voltage response and it is perfectly tracked to its set reference. In spite of a sudden power load introduction, this disturbance is instantaneously rejected and the control performances are not affected.

The speed variation effects for a given capacitor value. Figure 4 illustrates the influence of the changing speed effects on the voltage build-up process. The same load will be applied for all following sub-sections (P_{load} = 3500 W at $t = 0.5$ s). The proposed SEIG system control tracking performances is unaffected to the considered rotor speed variations.

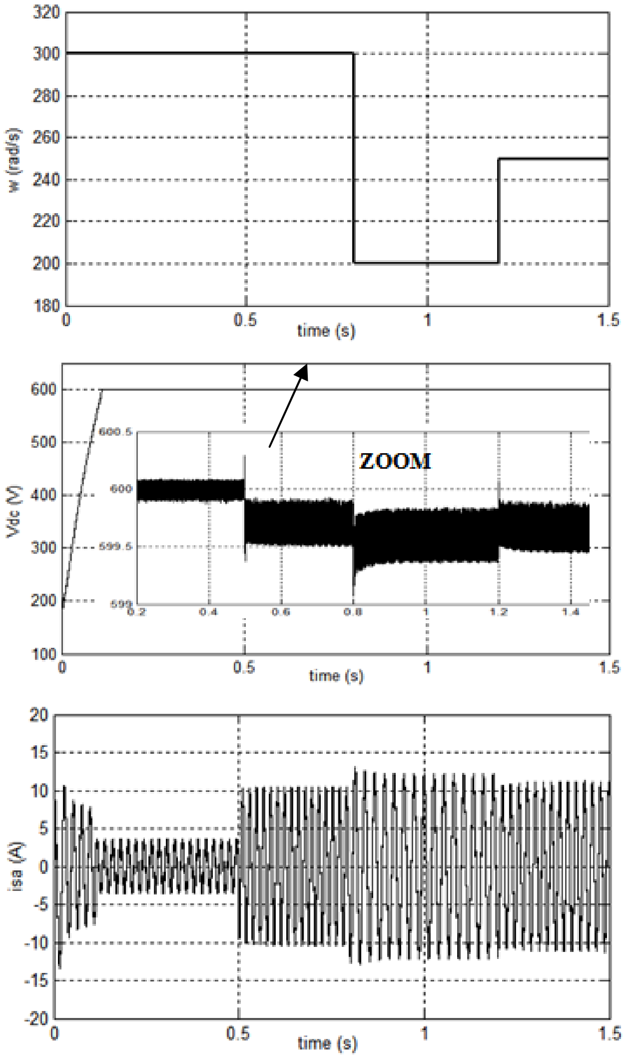

Fig. 4. The generator performances ($C = 1000$ µF)

The DC-bus voltage regulation performances under a practical rotor speed profile and load power demand. In order to simulate a practical case relative to the wind profile nature that imposes to the shaft the waveform represented on Fig. 5,*a*. The DC load is assumed to change according to the profile of Fig. 5,*b*, when the DC-bus voltage set value is fixed at 600 V (Fig. 5,*c*). The current rate is according to the demand of the load (Fig. 5,*d*).

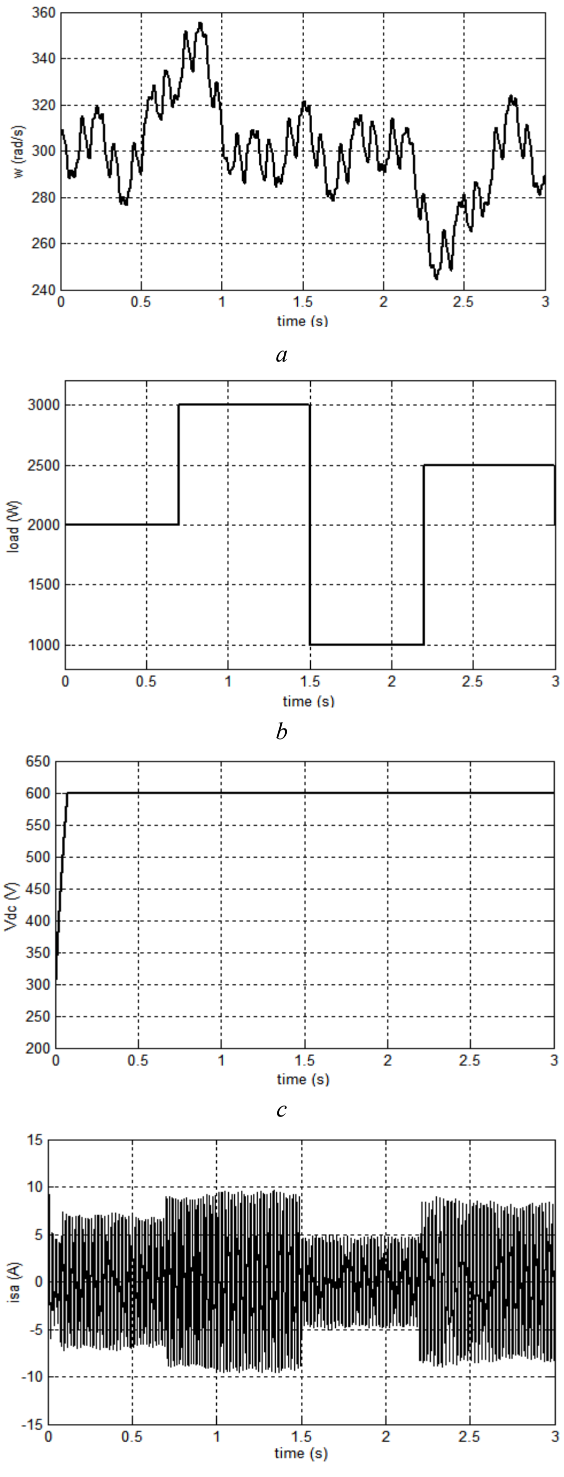

a

b

c

d

Fig. 5. The generator performances under speed and load variations

Robustness against variation in generator parameters. To verify the robustness of the proposed nonlinear control algorithm, some parameters changing is considered (case of stator rotor resistances changing). Figure 6 shows the control system performances when both stator and rotor resistances are intentionally augmented by 100 % with respect to the rated values under a constant rotor speed profile. The DC-bus voltage regulation still insensitive to the considered machine parameters variations.

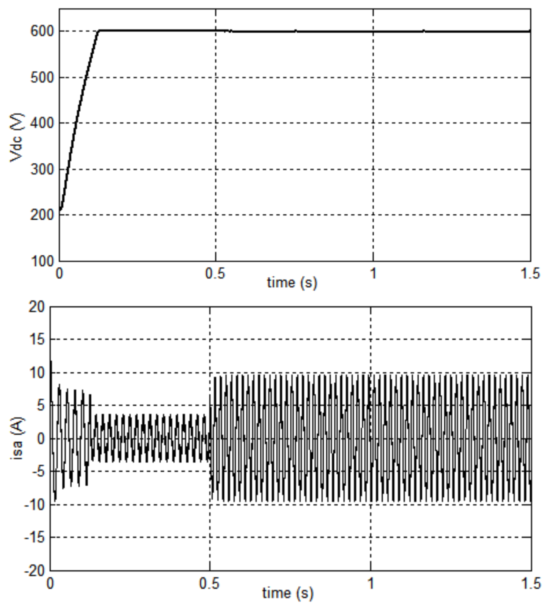

Fig. 6. The generator performances under stator and rotor resistances changing

Conclusion. This paper presents an efficient control approach based on the sliding mode theory for an induction generator operating in stand-alone mode associated to a pulse width modulation static converter with an intermediate DC link. The proposed control algorithm offers a perfect control performances under a simultaneously variation of the load power variation between 1 kW and 3 kW and the rotor speed between almost 240 rad/s and 360 rad/s. Moreover, these control characteristics remain insensitive to the machine parameters derives represented by 100 % of the stator and rotor resistances increase with respect to their nominal values. The obtained results show that the DC bus voltage tracking performance remains intact. The proposed system conversion control could be very useful for the wind power generating plants.

REFERENCES

1. AI Jabri A.K., Alolah A.I. Capacitance requirement for isolated self-excited induction generator. *IEE Proceedings B Electric Power Applications*, 1990, vol. 137, no. 3, pp. 154-159. **doi: 10.1049/ip-b.1990.0016**.

2. Chan T.F. Capacitance requirements of self-excited induction generators. *IEEE Transactions on Energy Conversion*, 1993, vol. 8, no. 2, pp. 304-311. **doi**: **10.1109/60.222721**.

3. Harrington R.J., Bassiouny F.M.M. New approach to determine the critical capacitance for self-excited induction generators. *IEEE Transactions on Energy Conversion*, 1998, vol. 13, no. 3, pp. 244-249. **doi**: **10.1109/60.707603**.

4. Seyoum D., Rahman M.F. The dynamic characteristics of an isolated self-excited induction generator driven by a wind turbine. *Industry Applications Society Annual Meeting (IAS), Conference Record of the IEEE*. **doi: 10.1109/IAS.2002.1042641**.

5. Sandhu K.S., Jain S.P. Steady state operation of self-excited induction generator with varying wind speeds. *International Journal of Circuits, Systems and Signal Processing*, 2008, vol. 2, no. 1, pp. 26-33.

6. Haque M.H. A novel method of evaluating performance characteristics of a self-excited induction generator. *IEEE Transactions on Energy Conversion*, 2009, vol. 24, no. 2, pp. 358-365. **doi: 10.1109/TEC.2009.2016124**.

7. Bhim S., Madhusudan S., Tandon A.K. Transient performance of series-compensated three-phase self-excited induction generator feeding dynamic loads. *IEEE Transactions on Industry Applications*, 2010, vol. 46, no. 4, pp. 1271-1280. **doi: 10.1109/TIA.2010.2049556**.

8. Kheldoun A., Refoufi L., Khodja D.E. Analysis of the self-excited induction generator steady state performance using a new efficient algorithm**.** *Electric Power Systems Research*, 2012, vol. 86, no. 2, pp. 61-67. **doi: 10.1016/j.epsr.2011.12.003**.

9. Haitao L., Lili C., Xiaodan Z., Yunxia L., Xuehu P. Build-up steady-state analysis of wind-driven self-excited induction generators**.** *The Journal of Engineering*, 2017, vol. 2017, no. 13, pp. 1383-1387. **doi: 10.1049/joe.2017.0558**.

10. Elsharkawi M.A., Venkata S.S., Williams T.J., Butlar N.G. an adaptive power factor controller for three-phase induction generators. *IEEE Transactions on Power Apparatus and Systems*, 1985, vol. PAS-104, no. 7, pp. 1825-1831. **doi**: **10.1109/TPAS.1985.319219**.

11. Malik N.H., Al-Bahrani A.H. Influence of the terminal capacitor on the performance characteristics of a self-excited induction generator. *IEE Proceedings C Generation, Transmission and Distribution*, 1990, vol. 137, no. 2, pp. 168-173. **doi: 10.1049/ip-c.1990.0022**.

12. Wang L., Dong-Jing L. Coordination Control of an AC-to-DC Converter and a Switched Excitation Capacitor Bank for an Autonomous Self-Excited Induction Generator in Renewable-Energy Systems. *IEEE Transactions on Industry Applications*, 2014, vol. 50, no. 4, pp. 2828-2836. **doi: 10.1109/TIA.2014.2298555**.

13. Stuty K., Bhuvaneswari G. Voltage regulation of a stand-alone Three-phase SEIG feeding single-phase loads. *IEEE Students' Conference on Electrical, Electronics and Computer Science*, 2014, **doi: 10.1109/SCEECS.2014.6804472**.

14. Mazurenko L.I., Dzhura O.V., Shevchuk S.P. Transients in a transistor-switched capacitor regulator of a stand-alone induction generator supplying a single-phase load. *International Conference on Modern Electrical and Energy Systems (MEES)*, 2017. **doi: 10.1109/MEES.2017.8248901**.

15. Benhacine T.Z.E., Nesba A., Mekhtoub S., Ibtiouen R. A balancing method for three-phase SEIG feeding a single-phase load by using switched capacitors. *International Conference on Electrical Sciences and Technologies in Maghreb (CISTEM)*, 2018. **doi: 10.1109/CISTEM.2018.8613410**.

16. de Resende J.T., Schelb A.J.H.C., Ferreira R., Manasses E.P. Control of the generated voltage by a three-phase induction generator self-excited by capacitors using control techniques. *IEEE International Conference on Industrial Technology*, 2003. **doi: 10.1109/ICIT.2003.1290386**.

17. Ahmed T., Nishida K., Soushin K., Nakaoka M. Static VAR compensator-based voltage control implementation of single-phase self- excited induction generator. *IEE Proceedings - Generation, Transmission and Distribution*, 2005, vol. 152, no. 2, pp. 145-156. **doi: 10.1049/ip-gtd:20051251.**

18. Shridhar L., Singh B., Jha C.S. Transient performance of the self regulated short-shunt self-excited induction generator. *IEEE Transactions on Energy Conversion*, 1995, vol. 10, no. 2, pp. 261-267. **doi: 10.1109/60.391891**.

19. Ojo O. Performance of self-excited single-phase induction generators with shunt, short-shunt and long-shunt excitation connections. *IEEE Transactions on Energy Conversion*, 1996, vol. 11, no. 3, pp. 477-482. **doi: 10.1109/60.536996**.

20. Fraile-Ardanuy J., Fraile-Mora J., Pedro A.G.G. Voltage control of isolated self-excited induction generator through series compensation. *Przeglad Elektrotechniczny*, 2012, no. 01a, pp. 132-136.

21. Abdelhamid B., Taoufik M., Lassad S. Shunt and short shunt compensation for induction machine generator. *17th International Conference on Sciences and Techniques of Automatic Control and Computer Engineering (STA)*, 2016. **doi: 10.1109/STA.2016.7951989**.

22. Jaswant S., Pawan K.Y., Abhishek K.C. Improvement in voltage profile in self excited induction generator using fuzzy logic. *International Journal on Future Revolution in Computer Science & Communication Engineering (IJFRCSCE)*, 2018, vol. 4, no. 1, pp. 113-117.

23. Kasal G. Singh B. Decoupled voltage and frequency controller for isolated asynchronous generators feeding three-phase four-wire loads. *IEEE Transactions on Power Delivery*, 2008, vol. 23, no. 2, pp. 966-973. **doi: 10.1109/TPWRD.2008.915783**.

24. Rajagopal V., Singh B., Kasal G. Electronic load controller with power quality improvement of isolated induction generator for small hydro power generation. *IET Renewable Power Generation*, 2011, vol. 5, no. 2, pp. 202-213. **doi: 10.1049/iet-rpg.2010.0081.**

25. Silva F.B., da Silva Gonçalves F.A., Vanço W.O., de Carvalho D.P., Bissochi Jr C.A., Monteiro R.V.A., Guimarães G.C. Application of bidirectional switches in the development of a voltage regulator for self-excited induction generators. *International Journal of Electrical Power & Energy Systems*, 2018, vol. 98, no. 5, pp. 419-429. **doi: 10.1016/j.ijepes.2017.12.025**.

26. Seyoum D., Grantham C., Rahman M.F. The dynamic characteristics of an isolated self-excited induction generator driven by a wind turbine. *IEEE Transaction on Industry Applications*, 2003, vol. 39, no. 4, pp. 936-944. **doi: 10.1109/TIA.2003.813738**.

Received 11.02.2020

Louze Lamri[1]*, Doctor of Electrical Engineering, Professor,*
Abdessemad Oussama[1]*, PhD student,*
Nemmour Ahmed Lokmane[1]*, Doctor of Electrical Engineering, Professor,*
Khezzar Abdelmalek[1]*, Doctor of Electrical Engineering, Professor,*
[1] Laboratoire d'Electrotechnique de Constantine (LEC),
Mentouri Brothers University, Constantine 1,
Constantine, Algeria.
e-mail: lamri.louze@lec-umc.org,
oussama.abdessamad@lec-umc.org,
ahmed-lokmane.nemmour@lec-umc.org,
abdelmalek.khezzar@lec-umc.org

How to cite this article:

Louze L., Abdessemad O., Nemmour A.L., Khezzar A. An effective control of an isolated induction generator supplying DC load for wind power converting applications. *Electrical engineering & electromechanics*, 2020, no. 3, pp. 65-69. **doi: 10.20998/2074-272X.2020.3.10.**

Матеріали приймаються за адресою:
Кафедра "Електричні апарати", НТУ "ХПИ", вул. Кирпичова, 21, м. Харків, 61002, Україна
Електронні варіанти матеріалів по e-mail: a.m.grechko@gmail.com

Довідки за телефонами: +38 050 653 49 82 Клименко Борис Володимирович
+38 067 359 46 96 Гречко Олександр Михайлович

Передплатний індекс: 01216